ISTITUTO NAZIONALE DI FISICA NUCLEARE - ISTITUTO NAZIONALE DI FISICA NUCLEARE - ISTITUTO NAZIONALE DI FISICA NUCLEARE - ISTITUTO NAZIONALE DI FISICA NUCLEARE - ISTITUTO NAZIONALE DI FISICA NUCLEARE - ISTITUTO NAZIONALE DI

Laboratori Nazionali di Frascati

LNF-93/002 (IR)
21 Gennaio 1993

The KLOE Collaboration

THE KLOE DETECTOR
Technical Proposal

PACS.: 11.30.Er; 13.20.Eb; 13.20.Jf; 29.40.Gx; 29.40.Vj

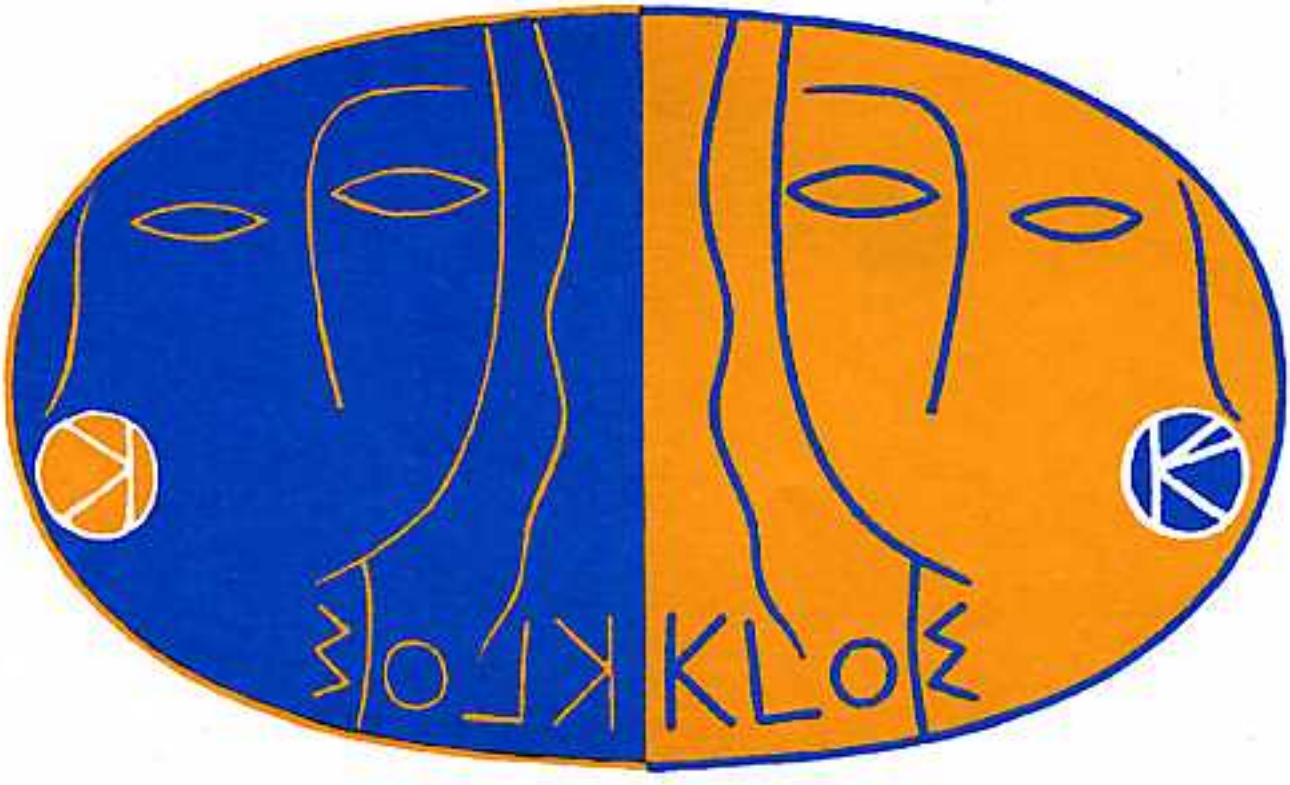

Servizio Documentazione
dei Laboratori Nazionali di Frascati
P.O. Box, 13 - 00044 Frascati (Italy)

LNF–93/002 (IR)
21 Gennaio 1993

The KLOE Collaboration

THE KLOE DETECTOR
Technical Proposal

PACS.: 11.30.Er; 13.20.Eb; 13.20.Jf; 29.40.Gx; 29.40.Vj

ERRATA CORRIGE

LNF-93/002 (IR)
21 Gennaio 1993

THE KLOE DETECTOR

Technical Proposal

Among the authors there are also:

C. BINI, G. DI COSIMO, A. DI DOMENICO, F. GARUFI, P. GAUZZI

Dipartimento di Fisica dell'Università e Sezione INFN, Roma I

INFN – Laboratori Nazionali di Fisica Nucleare
Servizio Documentazione

LNF–93/002 (IR)
21 Gennaio 1993

THE KLOE DETECTOR
Technical Proposal

The KLOE Collaboration

A. Aloisio[e], A. Andryakov[b], A. Antonelli[b], M. Antonelli[b], D. Babusci[b], R. Baldini-Ferroli[b], G. Barbiellini[m], M. Barone[i], K. Barth[c], S. Bellucci[b], G. Bencivenni[b], S. Bertolucci[b], S. Bianco[b], C. Bloise[b], V. Bolognese[h], F. Bossi[b], A. Calcaterra[b], P. Campana[b], M. Candusso[j], G. Capon[b], M. Carboni[b], R. Casaccia[b], G. Cataldi[d], N. Cavallo[e], L. Cerrito[j], F. Cervelli[h], F. Cevenini[e], V. Chiarella[b], G. Chiefari[e], M. Cordelli[b], P. Creti[d], S. D'Angelo[j], R. De Sangro[b], P. De Simone[b], G. De Zorzi[i], E. Drago[e], O. Erriquez[a], F. L. Fabbri[b], A. Farilla[a], G. Felici[b], M. L. Ferrer[b], G. Finocchiaro[j], P. Franzini[i,f], C. Gatto[e], G. Giordano[b], E. Gorini[d], F. Grancagnolo[d], U. v. Hagel[c], R. Haydar[b], M. Incagli[h], C. Joram[c], W. Kim[l], W. Kluge[c], G. Lanfranchi[i], P. Laurelli[b], J. Lee-Franzini[b,m], A. Martinis[m], M. M. Massai[h], G. Matone[b], L. Merola[e], A. Michetti[i], S. Miscetti[b], F. Murtas[b], G. P. Murtas[b,e], M. Napolitano[e], E. Nappi[a], E. Pace[b], G. F. Palamà[d], M. Panareo[d], L. Paoluzi[j], A. Parri[i], E. Pasqualucci[j], A. Passeri[k], V. Patera[b], I. Peruzzi[b,g], H. Peters[c], M. C. Petrucci[i], M. Piccolo[b], M. Reale[j], R. Sangoi[m], P. Santantonio[b], S. Sarwar[b], R. D. Schamberger[l], K. R. Schubert[c], F. Scuri[m], M. Spinetti[b], E. Spiriti[k], C. Stanescu[k], L. Tortora[k], P. M. Tuts[f], E. Valente[i], L. Votano[b], X. L. Wang[b], S. Weseler[c], R. Wieser[c], A. Zallo[b], F. Zecchinato[b].

[a] Dipartimento di Fisica dell'Università e Sezione INFN, Bari
[b] Laboratori Nazionali di Frascati dell'INFN, Frascati
[c] Institut für Experimentelle Kernphysik, Universität Karlsruhe
[d] Dipartimento di Fisica dell'Università e Sezione INFN, Lecce
[e] Dipartimento di Scienze Fisiche dell'Università e Sezione INFN, Napoli
[f] Physics Department, Columbia University, New York
[g] Dipartimento di Fisica dell'Università, Perugia
[h] Dipartimento di Fisica dell'Università e Sezione INFN, Pisa
[i] Dipartimento di Fisica dell'Università e Sezione INFN, Roma I
[j] Dipartimento di Fisica dell'Università e Sezione INFN, Roma II
[k] Istituto Superiore di Sanità and Sezione INFN, ISS, Roma.
[l] Physics Department, State University of New York at Stony Brook.
[m] Dipartimento di Fisica dell'Università e Sezione INFN, Trieste/Udine

TABLE OF CONTENTS

1. INTRODUCTION

1.1 Direct CP violation

The KLOE detector[1] is designed primarily with the goal of detecting direct CP violation in K^0 decays with a sensitivity of $\sim 10^{-4}$ in $\Re(\epsilon'/\epsilon)$, without forgetting a vast amount of other physics.[1] In the following we will only refer to physical observables. Since the observation,[2] in 1964, that the long lived K^0 meson decays into two pions, the search for direct CP violation has failed.

If the direct CP violating amplitude $\langle \pi\pi | K_2 \rangle$, where K_2 is CP-odd, vanishes, then:

$$\mathcal{R}_S \equiv \frac{\Gamma(K_S \to \pi^+\pi^-)}{\Gamma(K_S \to \pi^0\pi^0)} = \mathcal{R}_L \equiv \frac{\Gamma(K_L \to \pi^+\pi^-)}{\Gamma(K_L \to \pi^0\pi^0)}, \tag{1.1}$$

otherwise, in general, $|\mathcal{R}_S - \mathcal{R}_L| = \Delta\mathcal{R} \neq 0$ and $\Delta\mathcal{R}/\mathcal{R} = 6 \times |\Re(\epsilon'/\epsilon)|$.

The present experimental knowledge is:[3]

$$\frac{\Delta\mathcal{R}}{\mathcal{R}} = \begin{cases} (4 \pm 4) \times 10^{-3} \\ (14 \pm 4) \times 10^{-3} \end{cases} \sim (0 - 2) \times 10^{-2} \tag{1.2}$$

Theoretical predictions, with large uncertainties, are $\Delta\mathcal{R}/\mathcal{R} \leq 10^{-2}$, if the top mass is considerably lower than 160 GeV. Rumors[4] would suggest a top mass around 130 GeV. The aim of KLOE is to reach a sensitivity in $\Delta\mathcal{R}/\mathcal{R}$ of $\sim 6 \times 10^{-4}$, achievable at DAΦNE at full luminosity, from the statistical point of view, in about one year. The two formidable tasks for KLOE to face are the controlling of efficiencies for the decays of interest and the rejection of background from the copious K_L decays to states other than two pions. At DAΦNE, in addition, direct CP violation can be observed by interferometry.[5–9] Many of the systematic uncertainties are the same for the two methods. Their effect on the ratios defined in eq. (1.1) is slightly more intuitive and we will limit our discussion to this case.

1.2 Measuring the two pion BR's

The relation between measurements and BR's, assuming tagging is used, is:

$$\underbrace{N_{L,S}^{\pm,0}}_{\text{observed}} - \underbrace{Bck_{L,S}^{\pm,0}}_{\text{estimated}} = \underbrace{N_{KK} \times \varrho_{L,S}(\text{tag})}_{\text{drops identically}} \times \underbrace{BR_{L,S}^{\pm,0}}_{\text{desired}} \times \underbrace{\left\langle \varrho_{L,S}^{\pm,0} \right\rangle}_{\langle\text{efficiency}\rangle} \times \iint_{\text{FV}} g(l - l') I(l)\, \mathrm{d}l\, \mathrm{d}l' \tag{1.3}$$

The double integral is a convolution of the decay intensity $I(l)$ and the experimental resolution $g(l - l')$ in the measurement of the decay path length and an integration over the fiducial volume, FV, of the detector. The implications of detector size, knowledge of the boundary of the fiducial volume and magnetic field value are discussed in this section. The four backgrounds $Bck_{L,S}^{\pm,0}$ and the averaged efficiencies $\left\langle \varrho_{L,S}^{\pm,0} \right\rangle$ are different. They must be known to an accuracy of $\mathcal{O}(1/3000)$ and will be discussed in detail in the appropriate sections later.

1.3 Fiducial Volumes

As described later, we assume a detector consisting of an electromagnetic calorimeter, a large tracking chamber and a vertex detector. The calorimeter has a central part which can be approximated as a cylinder of 2 m radius and 3.5 m length closed by two end-caps, covering ~98% of the solid angle. The chamber, with inner wall of 25 cm radius, provides tracking for $30 < r < 200$ cm. The whole detector is immersed in a solenoidal field of 0.6 T. Regeneration in walls (beam pipe, chamber walls) is $\leq 1\%$.[6] Use of a large beam pipe, inside which all K_S's decay, and rejection of K decays up to 6 cm (10 τ_S) past any wall eliminates the effects of $K_L \to K_S$ regeneration. The fiducial volume (FV) for K_S and K_L decays are idealized below.

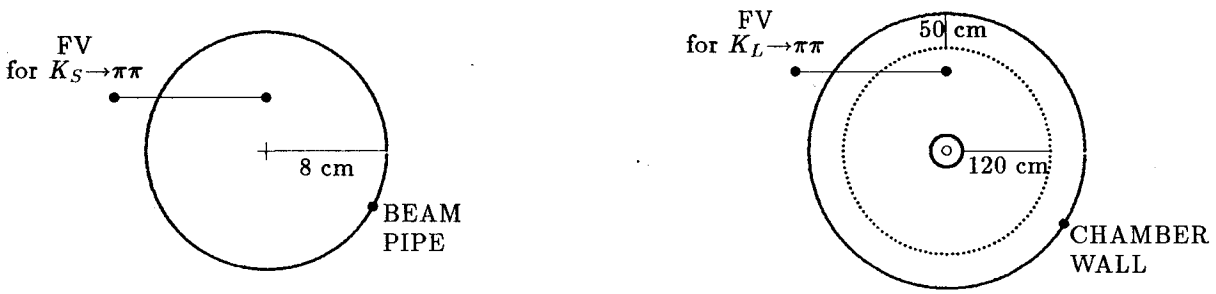

Fig. 1.1. Fiducial Volumes for K_S and K_L decays.

A beam pipe of 8-10 cm radius provides a vacuum region in which all K_S's decay. The helium based chamber is both the decay volume for K_L's and measures angle and momenta for charged particles. The fiducial volume for K_L decays, in cylindrical coordinates, is taken as:

$$\begin{aligned} 30 < r < 150 \text{ cm} \\ -125 < z < 125 \text{ cm} \end{aligned} \qquad (1.4).$$

1.3.1 K_S decay fiducial volume.

If the integral of eq. (1.3) can be carried out to ∞, FV boundary and resolution do not contribute any error. This is essentially the case for K_S decays. A K_L signal guarantees the presence of a K_S. The beam pipe has radius equivalent to $\geq$13-17 lifetimes. Therefore without imposing, ideally, any fiducial volume cut on the data, the integrals are "1", independently of flight path resolution. Efficiencies for $\pi^+\pi^-$ and $\pi^0\pi^0$ decays are $\geq$99% and are well controlled. Backgrounds are at the level of 10^{-3}, before any cut is applied.

1.3.2 K_L decay fiducial volume.

The case is quite different for K_L decays, since the fiducial volume has dimensions, ~120 cm, which is a small fraction of the mean decay path, ~350 cm. A small error on the determination of the boundary of the fiducial volume can introduce large errors on $\mathcal{R}_L$, at the accuracy of interest. In particular what is relevant is the relative error in the determination of the boundaries of the fiducial volumes for $K_L \to \pi^+\pi^-$ and $K_L \to \pi^0\pi^0$, since different methods are used to obtain the K_L path length. $K_L \to K_S$ regeneration at the chamber inner wall provides in fact an excellent check of the correct knowledge of the inner boundary of the fiducial volumes. Observation of the enhanced $\pi^+\pi^-$ and $\pi^0\pi^0$ signals from K_S decays from the same source does provide the required check. The outer boundary requires more care. Assuming a spherical fiducial volume

defined by $30 < R < R_{\rm FV}$ cm, the fractional change in detected events per unit change in $R_{\rm FV}$ is:

$$\frac{\delta N/N}{\delta R_{\rm FV}} = \frac{1}{350} \times \frac{1}{\exp((R_{\rm FV} - 30)/350) - 1}\ {\rm cm}^{-1}$$

For $R_{\rm FV}=\infty$ the error on $\delta N/N$ vanishes. For $R_{\rm FV}=150$ cm, $\delta N/N \sim 1\%$ for $\delta R_{\rm FV}=1$cm, while for $R_{\rm FV}=500$ cm the fractional error on N is 10 times smaller. More relevant, a reduction on detector size of 20%, for the one given above, implies a reduction in fiducial volume of a factor 2 and an increase in the fractional error of a factor three. The argument above is illustrative, since it is clearly better to use a cylindrical fiducial volume. The distribution of the K_L decay points in space is shown in

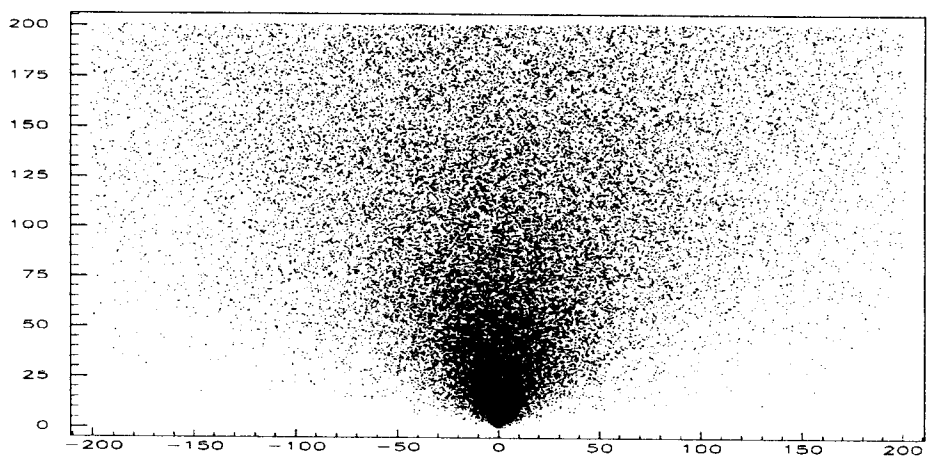

Fig. 1.3. Distribution of K_L decay points in cylindrical coordinates.

We define a cylindrical fiducial volume similar to eq. (1.4) and obtain the fractional error on the number of decays per cm change in the r and z boundaries shown in fig. 1.4 as function of the calorimeter dimensions, assuming that the FV terminates 50 cm from its inner walls.

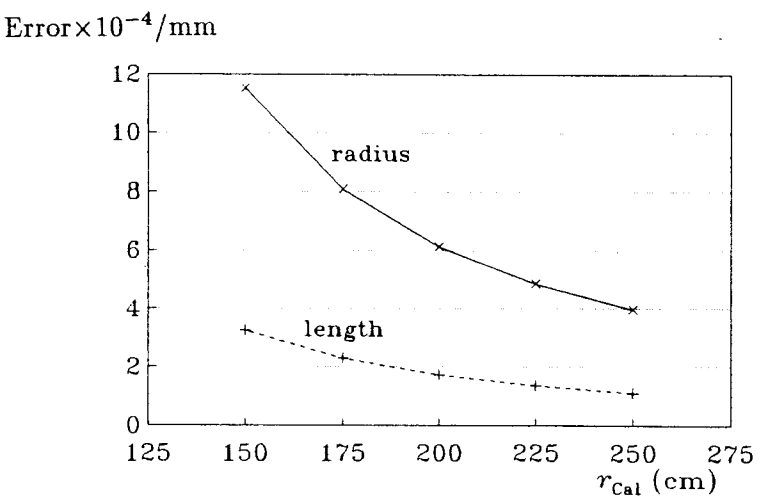

Fig. 1.4. $(1/N)(\delta N/\delta R_{\rm FV})$ in ${\rm mm}^{-1}\times 10^{-4}$ vs calorimeter radius for $|z|=170$ cm.

We are clearly much less sensitive to uncertainties in the z–boundary, as is obvious from fig. 1.3. To achieve a sensitivity of 3×10^{-4} in $\Delta\mathcal{R}/\mathcal{R}$, we must ensure that the outer boundaries of

the fiducial volumes for charged and neutral decays are equal to better than 0.5 mm. The most effective way to ensure this is to use K_L decays for which both a "neutral" and a "charged" decay vertex is measurable such as $K_L \to \pi^+\pi^-\pi^0$. Decays of charged K's, $K^\pm \to \pi^\pm\pi^0$, can also be used over part of the FV.

The above argument justifies our choice for the detector size in the sense that it is the value for which the fractional change in $(1/N)(\delta N/\delta R_{\rm FV})$ equals the fractional change in detector volume. It is by no means the only argument: in general, the safety factor of the experiment for all the points we have considered increases with the FV size. They include angular resolution for photons, time of flight measurements, available size of photomultipliers and all factors implied by eq. (1.3).

1.4 Magnetic Field

Of crucial importance in rejecting contamination of the $K_L \to \pi^+\pi^-$ sample is the ability to perform good measurements of momenta in the range 150–270 MeV/c. In particular $K_{\mu 3}$ decays overlap kinematically with $K_L \to \pi^+\pi^-$ decays when the laboratory muon momentum is $\sim$250 MeV. A simple argument predicts that kinematical overlaps decrease as the cube of the field value. This has been proved by full Monte Carlo calculations. A possible argument against high field is the loss of tracking efficiency and accuracy in vertexing for spiraling tracks. Again we barely see a loss in tracking efficiency beginning at 7 kG, $\sim$0.2% as well as some saturation in the $K_{\mu 3}$ background rejection. Thus, our choice of 6 kG, which provides good rejection without impairing other detector functions, is justified. We note that CLEO[10] uses a field of 15 kG at the $\Upsilon(4S)$ where the most probable secondary momenta are around 200 MeV/c.

2. THE KLOE DETECTOR

The experimental apparatus must be able to track charged particles of momenta between 50 and 250 MeV/c. It must also detect, with very high efficiency, γ's with energy as low as 20 MeV, measure their energies with a resolution $\delta E_\gamma / E_\gamma \sim 15\%$ at 100 MeV and provide the space coordinates of the photon conversion point.

The general features of the detector are similar to those of a *standard* general purpose collider's apparatus: a cylindrical structure surrounding the beam pipe consisting of a vertex chamber, a large tracking device with high efficiency for the K^0 decay products, an electromagnetic calorimeter with exceptional timing ability, also providing some particle identification, and a solenoidal magnet, in order of increasing radius, as shown in fig. 2.1.

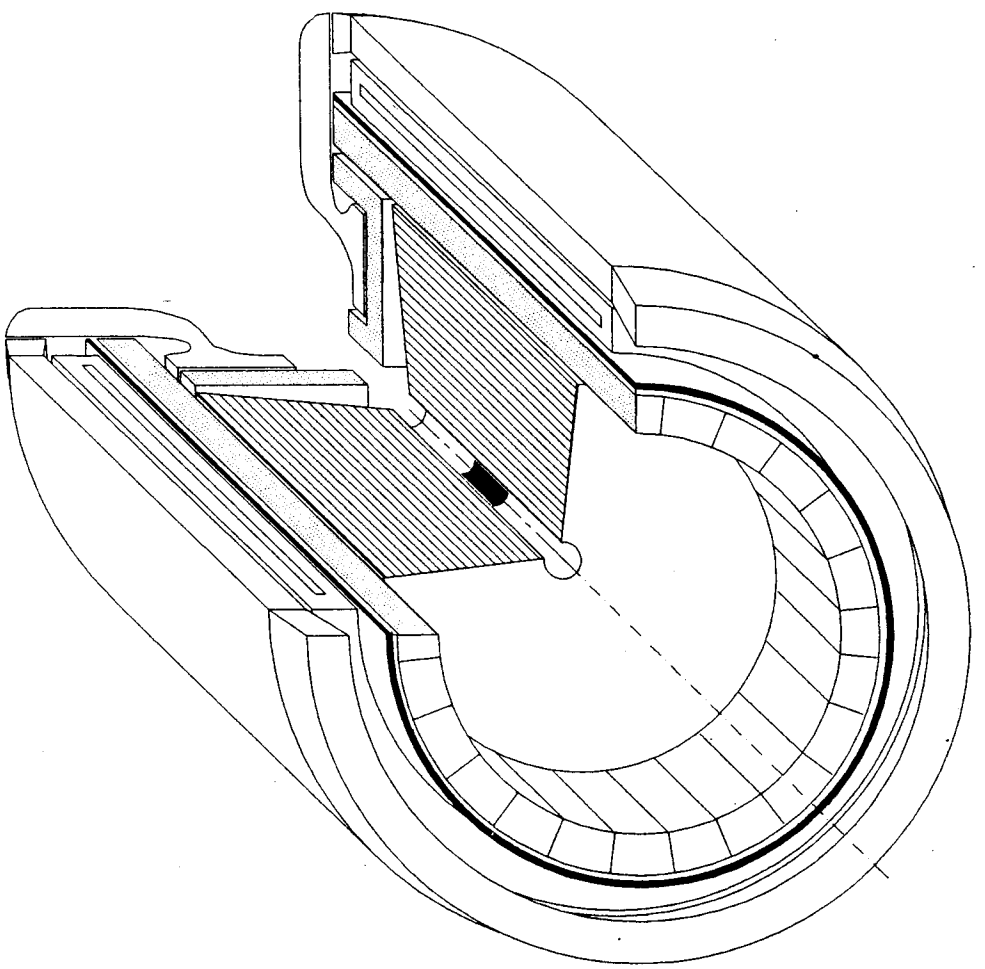

Fig. 2.1. The KLOE detector.

In the following we will use a cartesian coordinate system with the $z$axis along the beam direction. The x-axis is horizontal and the y-axis is vertical.

2.1 Beam Pipe

The radius of the beam pipe is chosen to be between 8 and 10 cm, the final choice depending

on solving problems due to the beam pipe acting as a free-wheeling cavity. This allows us to define a fiducial region for K_S decays without complications from regeneration. The beam pipe wall is made of 0.5 mm thick beryllium, or some equivalent low mass, low Z material to minimize multiple scattering, energy loss for charged kaons and regeneration.

2.2 Calorimetry

Reconstruction of the $\pi^0\pi^0$ decay mode of a 110 MeV/c momentum K, the determination of its decay point and the efficient rejection of the three π^0 decays make the e.m. calorimeter, EmC, a most demanding element of the detector. In particular the EmC must provide a good measurement in three dimensions of the photon conversion point.

We propose to use a lead–scintillator sampling calorimeter using very thin lead layers, 0.5 mm, and 1 mm scintillating fibers. Such device has acceptable resolution and good efficiency ($> 99\%$) for photon energies down to 20 MeV. In addition the use of fibers gives extremely good time resolution. Measurement of the time of arrival of a photon gives the flight path of the K^0 to an accuracy $\delta l = \beta_K c\, \delta t \sim 6 \times 10^{-3}$ cm $\times\, \delta t$(ps). For a 510 MeV K^0, that is for four photons with $\sum E_\gamma = 510$ MeV and a sampling fraction of $\sim$12%, one expects a timing resolution of about 100 ps and a flight path resolution of 6 mm. In a realistic simulation a resolution of 8 mm is obtained. We recall that time measurements for a single photon allow the determination of the flight path. This implies that observation of only three photons still allows an overconstrained determination of both the K^0 mass and the flight path, using timing information to supplement geometrical and energy measurements.

Finally, among all proposed solutions, the structure discussed above is relatively simple to build, does not require a disproportionate number of read–out channels, does not have thick walls in front and lends itself most easily to the construction of a truly hermetic calorimeter.

The EmC is divided in a central part, approximating a cylindrical shell, of 4 m diameter, 3.7 m effective length and 25 cm thickness. Two end-caps, 4 m in diameter and 25 cm thick close, as hermetically as possible, the calorimeter. The beam pipe holes are $\sim 20 \times 30$ cm^2.

2.3 Tracking

The reconstruction of the CP violating decay $K_L \to \pi^+\pi^-$, the rejection of the $K_{\ell 3}$ background, the determination to good accuracy, $\sim$10 mr, of the K_S flight direction and of the decay vertices, $\sim$3 mm, are the main tasks of the tracking system. Material thicknesses must be kept as low as possible to minimize multiple scattering and regeneration effects and not affect the performance of the EmC. We chose a drift chamber over a time projection chamber which would suffer at the high event rates of DAΦNE, especially Bhabha's at $10° < \theta < 20°$. Because the main tracking chamber cannot begin at $r < 25$ cm, the interaction region is surrounded by a vertex chamber. The vertex chamber consists of $\sim$1350 *straw* tubes, covering the range $-40 < z < 40$ and $10 < r < 25$ cm.

The large tracker uses a rectangular cell, with an area per cell of $\sim 2 \times 2$ cm^2 at $z=0$ for a total sense wire count of $\sim$27,000. Only stereo wires are used, maintaining a constant radial wire drop vs radius, with a stereo angle of $51 < \mathrm{ang} < 112$ mr. The gas is helium, with the usual addition of hydrocarbons, to control the multiple scattering.

The main chamber is cylindrical, with dimensions approximately 2 m radius and 3.5 m length at the outer rim. The end-plates are truncated cones of 75° half angle. The radiation length of the gas plus wires is ~500 m. The performance parameters of the KLOE tracking device are: $\sigma_{r,\phi}$=200 μm and σ_z=4 mm, σ_{p_T}/p_T=0.3% and a track reconstruction efficiency, averaged over $K_L \to \pi^+\pi^-$ decays, of $\geq$98%.

The low β insertion quadrupoles are supported by the chamber end-plate. These magnets also have implications on our particle acceptance.

2.4 Backgrounds

The rejection of three pion decays relies on good solid angle coverage and efficiency for γ's down to 20 MeV energy. Kinematic fitting, with good tracking and calorimeter information appear to be able to reject $K_{\mu 3}$ events to the required level. Other decays are more easily distinguished.

2.5 Trigger

Triggering at DAΦNE will be an entirely new experience. At full luminosity, the ϕ–event rate is ~5 kHz while the machine produced background can be estimated, scaling from other machines, to be a few % of this value. All events can thus, in principle, be passed to the digitizing electronics (FEE) and the data acquisition system (DAQ). The calorimeter can provide an adequate trigger for most events of interest. Special events might require tracking in the vertex chamber. Bhabha scattering at angles $10° < \theta < 20°$ and cosmic ray events must be recognized and rejected or prescaled not to overload FEE and DAQ. Both classes of events are important for detector calibration. Calorimeter information and simple combinatorial logic can effectively reject/scale these events.

2.6 Data Acquisition

The ϕ decays and calibration events represent, at full DAΦNE luminosity, a very large load for the data acquisition system. At 10,000 events per second, each event consisting of 2 to 4 kBytes, we estimate that 20,000 MIPS equivalent computing power will be necessary to digest the data. The universal approach appears to be farms of the new powerful μ–processors. We are at present looking at the α–VAX product of DEC, capable of 120 MIPS, but we will not commit ourselves to any solution for the next couple of years. We must mention two more points. We intend to write to tape all raw data, and we need to perform Monte Carlo simulations at the 10^8, or greater, event level. The data produced in one year at full $\mathcal{L}$ is $\sim 4 \times 10^{14}$ Bytes, to be stored at a bandwidth of 25–50 MBytes/s. The new 19 mm tape technology seems capable of such a task. Due to the Monte Carlo needs and the inevitable necessity of running production more than once we plan on two 20,000 MIPS farms.

2.7 Magnet

Economical reasons, *i.e.* power consumption, make a superconducting coil the choice of interest. In addition, the whole detector set up requires temperature control to within 2° C, difficult to achieve with a warm coil. Several reasons for this decision are described later.

3. KLOE MAGNET AND MECHANICAL STRUCTURES

The KLOE set-up is subdivided, like most similar experiments aiming at maximum angular coverage, in a central part of approximately cylindrical shape, called the barrel and in two end-caps (see fig. 3.1 and fig. 3.2). The barrel includes the iron shell transmitting the magnetic flux, the cryostat containing a superconducting solenoid, the 24 modules of the EmC made of lead and scintillating fibers, the main and vertex drift chambers and finally the axial vacuum chamber surrounded at each end by a triplet of permanent magnets quadrupoles. The end-caps are the two magnet pole pieces each carrying an EmC also made of lead and scintillating fibers, and subdivided in parallel modules. Each end-cap is split into two halves along the longitudinal vertical symmetry plane; each half is hanging from a carriage rolling on a beam supported by the barrel. These beams can pivot outward up to an angle of 20° to permit the opening of the end-cap and give access to the inside detectors for inspection and maintenance. The whole set-up is supported by four columns in the interaction pit and by four carriages rolling on rails in the assembly hall and during translation from the assembly hall to the DAΦNE hall (fig. 3.3). Two systems of rails perpendicular to each other are laid down in the floor of the assembly hall and one of them extends to the interaction pit. The carriages of the set-up can be rotated in order to orient themselves to the chosen rail system direction. An existing, non-removable, ferroconcrete structural beam limits the entrance height into the machine hall to 4 m above the floor. Consequently the assembly hall floor, extending to a wide pit into the machine hall, is put at a lower level (−4 m) permitting the passage of the set-up below the beam. In the experiment position the set-up will be raised by about 1.2 m by means of hydraulic jacks, the carriages will be removed and replaced by 4 columns. The cabling will be done in the assembly hall; the cables will be placed in articulated trays that can accomodate the motion of the detector. Fig. 3.4 and fig. 3.5 show the layout and the longitudinal cross section of the assembly hall and the experimental area, the limits of the 4 m deep pit excavated in the area and the rail system. Both the experimental area and the assembly hall are served by 30 ton load cranes. Table 3.1 gives the basic parameters of the magnet.

3.1 The Iron Yoke

3.1.1 Barrel

The steel structure of the barrel, fig. 3.6, consists of two strong longitudinal elements on which twelve curved pieces, eight of which are on the upper side and four on the lower side, are mounted to form in this way an approximately cylindrical structure. At each end of the barrel a strong continuous steel ring of approximately conical shape is bolted. This ring provides stiffness and, due to its shape, reduces somewhat the size and weight of the end-caps. Several notches for the passage of cables and pipes are present on the outside face of the rings: adequate apertures are present on the curved pieces for the cryogenic chimney, the vacuum ducts and the power and control cables of the coil. The longitudinal pieces support the cryostat and the calorimeter load and are provided with long flat surfaces for the sliding of the cryostat during mounting. The longitudinal pieces are provided with horizontal bottom surfaces, which rest on the set-up supports (carriages, columns, jacks). All the pieces are made of low carbon cast steel and are machined only on the mating surfaces. The weight of each individual piece is less than 30 tons,

to permit the mounting of the yoke by means of the crane. The various pieces are bolted and doweled together.

3.1.2 end-caps

Each pole piece of the iron yoke, or end-cap, fig. 3.7 consists of 4 approximately equal 90° sectors, weighing 25 ton each. A 70 cm diameter aperture is provided at the axis for the passage of the DAΦNE beam pipe as well as the ends and the photomultipliers, PM's, of the central end-cap calorimeter modules. The ring plates are furthermore bolted inside and outside the end-caps to shape the field at the position of the central PM's. The sectors are bolted in pairs and the bolting is calculated to resist the magnetic field forces (~150 ton per end-cap) which pull the end-caps inwards. All the pieces are made with low carbon cast steel which is particularly suitable to obtain the particular shape required: a protruding pole, a deep circular cavity for the reduction of the field and the location of the calorimeter ends, becoming reentrant and thin in the central region, to reduce the interference with the adjacent compensators when the end-caps are translated for opening. The end-cap sectors will also be machined only on the mating surfaces. Notches will be provided on the faces in contact with the barrel, to provide passage for the cables. The upper sectors carry means to attach them to the upper supporting structure.

TABLE 3.1. Basic magnet parameters.

Field value	0.6 T
Useful field volume	~76 m^3
Stored energy	1.3×10^7 joule
Overall length	6.1 m
Overall length at the axis	4.2 m
Overall width	6.8 m
Height of the axis above the floor in the assembly hall at the experiment	 3.95 m 5.2 m
Maximum height above the axis	4 m
Weight of the barrel yoke	~340 ton
Tot. yoke (+ supports) weight	475 ton
Cryostat and coil weight	40 ton

3.2 Coil and Field Shape

The coil is superconducting. This choice has been taken after many comparisons of cost and performance with the conventional warm solution and after clarification of the several questions raised by the special committee which was formed in order to advise in this matter.[11] Discussions with some manufacturers and outside experts provided further useful information. LNF

decision to install a dedicated refrigerator for the DAΦNE complex (experiments and compensator magnets) provided another strong motivation. The arguments in favor of the s.c. coil are smaller operating cost, the easier temperature control of the detector and the reduction in overall size and weight of the apparatus. The arguments against it are: the higher initial cost, which, however is compensated for, in a few years, by the lower operating cost, the longer delivery time (however still compatible with the general KLOE schedule) and the need of more skilled operators. Table 3.2 gives the main parameters of the coil.

TABLE 3.2. Basic coil parameters.

amp×turns	2.1×10^6
average radius of the winding	~2.6 m
length of the winding	4.2 m
inside radius of the cryostat	2.4 m
outside radius of the cryostat	2.85 m
cryostat overall length	4.6 m
current rise time	20 min
nominal current	$3000 < I_N < 4000$ A
refrigeration (steady operation)	< 40 W at 4.2° K < 1500 W at ~70° K < 0.8 g/sec of liquid He

The detailed design will be done by the coil manufacturer and it is conceivable that minor changes in the cryostat geometry will appear at that moment. The active coil length covers exactly the distance between the pole pieces. In this way the best field uniformity in the tracker volume is achieved. Fig. 3.8 shows the field lines in the tracker given by the 2–dimensional program "Poisson". The uniformity of the field is better than 7% in the entire volume and better than 2% in 90% of the tracker volume. On the other side the field value is strongly reduced at the position of the photomultipliers reading the EmC light output. This value is actually lower than 2 kG at all the PM positions and the direction of the field there has an angle always smaller than 30° with respect to the axis of the set-up along which all the PM's are oriented. The performance test done on the PM's under these conditions show that the achieved field shape is satisfactory.

3.3 The Barrel Supports

The four carriages carrying the set up are each composed of two four-wheels *buggy* moving on a double rail, and inserted in a steel frame which transmits the load through hydraulic jacks. A common hydraulic circuit for the jack provides for an equal sharing of the load between the buggies of a single carriage and among the carriages themselves. The frames are mounted below the longitudinal elements of the barrel in a way which permits them to pivot around a vertical axis. This operation is needed when, at the crossing point of the two rail systems, the direction

of movement has to be changed from one system to the other one. Before this operation takes place, the whole set-up has to be jacked up by few centimeters. The jacks are applied to the other flat areas of the barrel longitudinal pieces. A much longer lift of the set-up is needed in the interaction pit ($\sim$1.2 m) to put its axis at the DAΦNE beam level. This operation will be done in various steps with the help of concrete blocks and steel spacers, to avoid the use of too cumbersome elements. Once the detector is located in its final position, four columns (about 2.6 m high) will replace the carriages. These columns, strongly bolted on the floor, will permit minor adjustments of the set-up, fig. 3.9. The displacement of the set-up along the rails shall not be frequent. Therefore no motorized driving system is considered to be necessary. Due to the low friction of the wheels on the rails, the forces needed for the displacement are relatively low. The driving will be done very simply by means of winches attached to specific reinforced points of the building.

3.4 The End-Cap Opening System

Each half end-cap, weighing approximately 60 tons, will hang from a wheel structure rolling inside a strong iron beam. The total foreseen stroke is about 1.7 m. One end of the iron beam is attached above the barrel on a vertical pivot, around which it can rotate outwards; the beam is furthermore supported on a set of conical rollers moving on a flat horizontal surface cut out of the barrel end ring. The total force pushing the rings when the end-cap is fully open amounts to about 250 tons; the end rings, their bolting, and the conical rollers are designed to support such large forces. The opening of the end-cap will occur in three steps. The first one is a longitudinal displacement to disengage the end-cap from the barrel, fig. 3.10 b; this displacement brings the end-cap very close to the adjacent compensator magnet. The second step corresponds to the rotation outwards of each half end-cap up to the width limits of the compensator, fig. 3.10 c. Finally the third step is a further rolling out of the end-cap to provide lateral opening of the set-up, fig. 3.10 d. A pantograph type system will be provided in order to keep the orientation of the end-cap halves during the movements. The end-caps opening is a more frequent operation than the displacement of the apparatus. Therefore its drive will be motorized and a system of rack and pinion gears or similar will be provided, as well as the safety switches and the encoders permitting the accurate control and reproducibility of the movements.

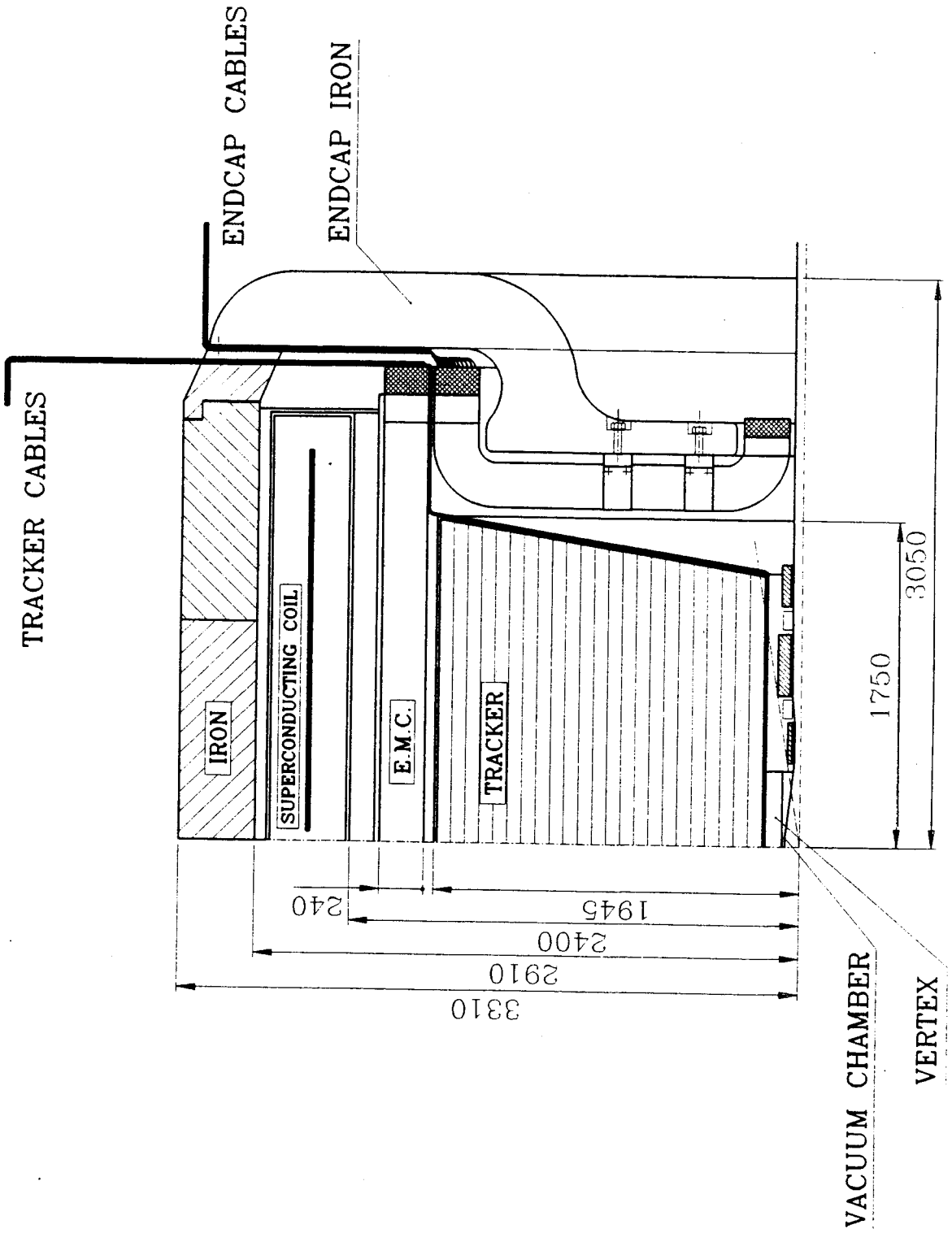

Fig. 3.1. KLOE, detail of the detector.

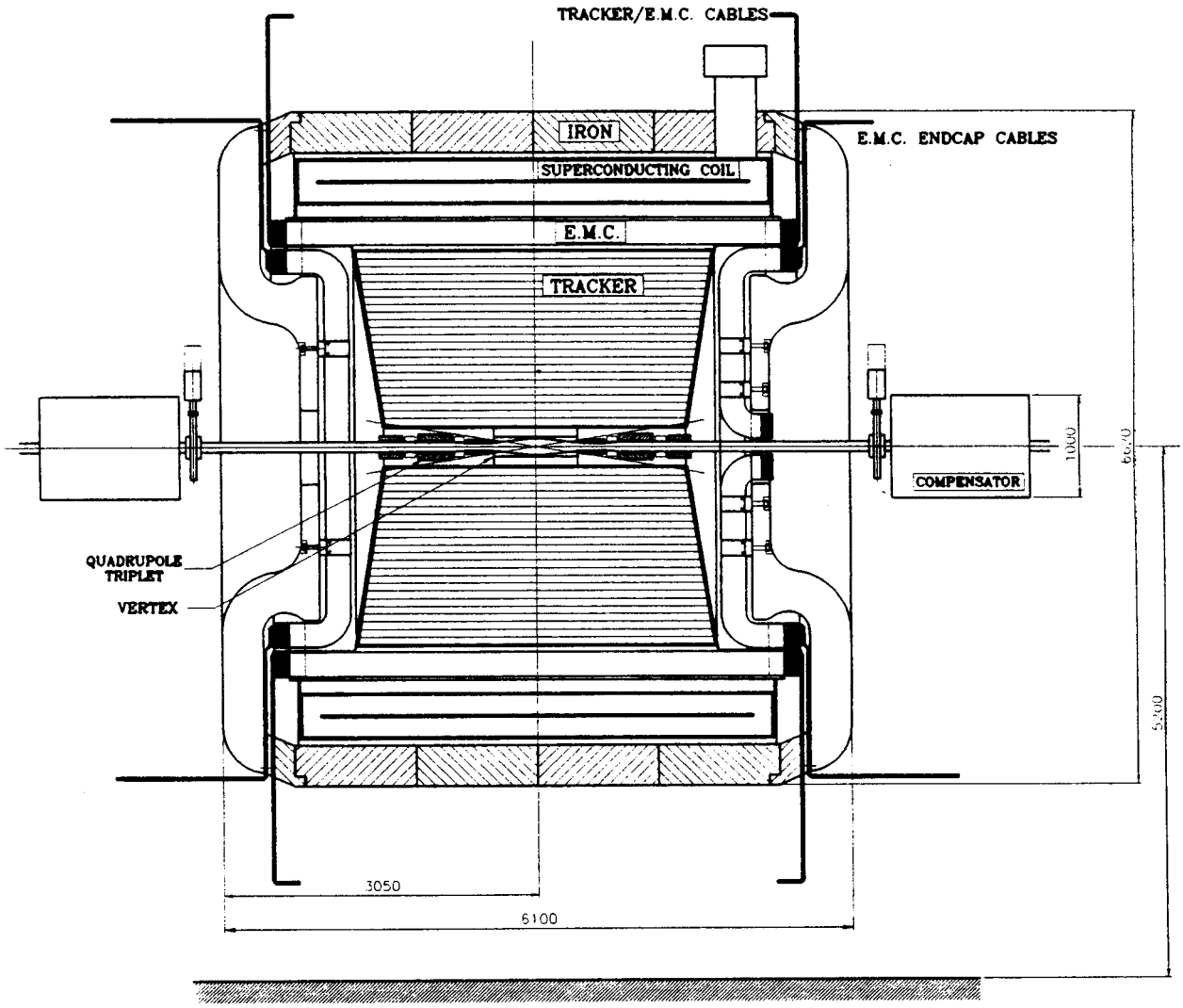

Fig. 3.2. KLOE, vertical cross section through the beam axis.

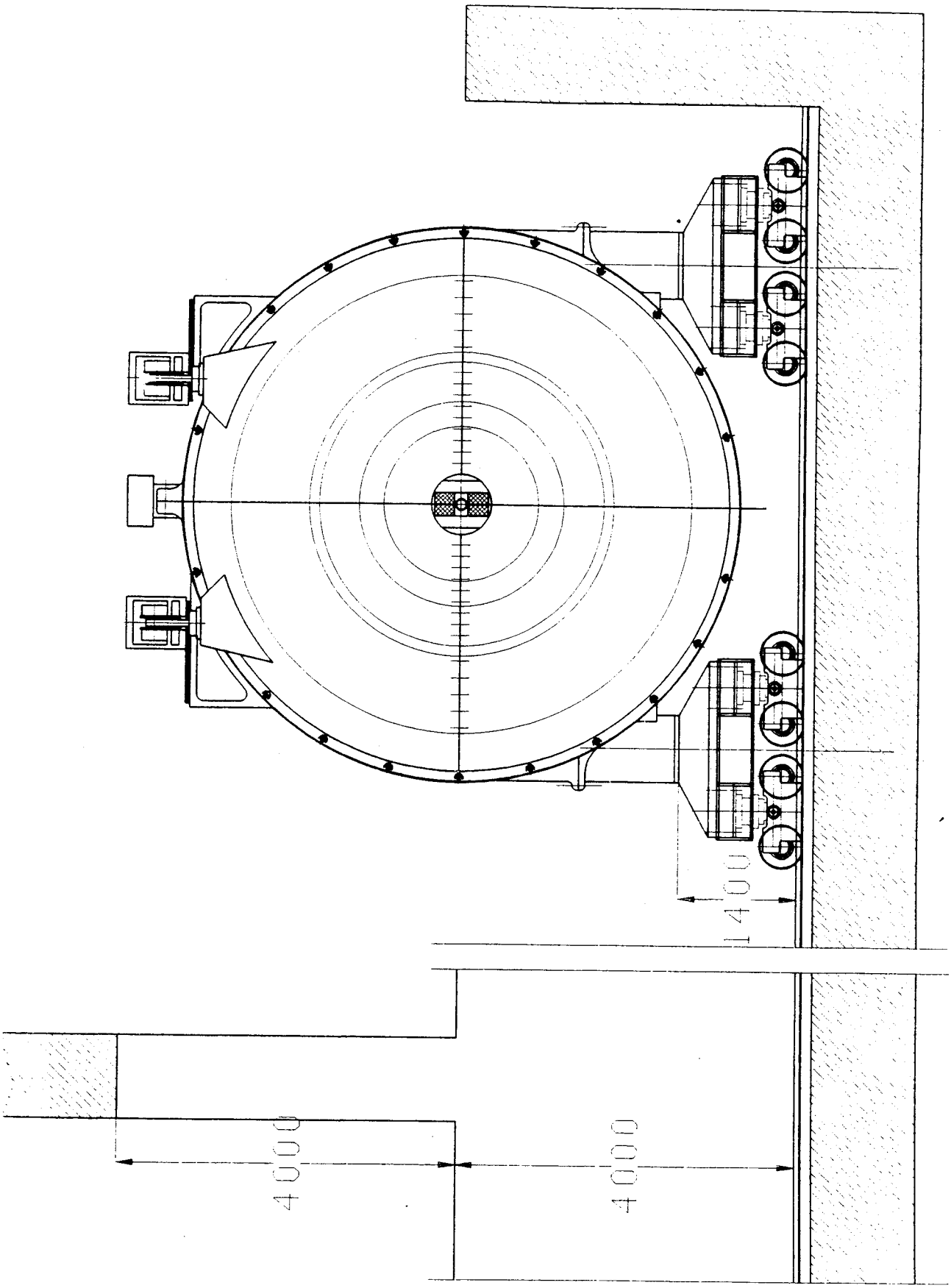

Fig. 3.3. Carriages and supports.

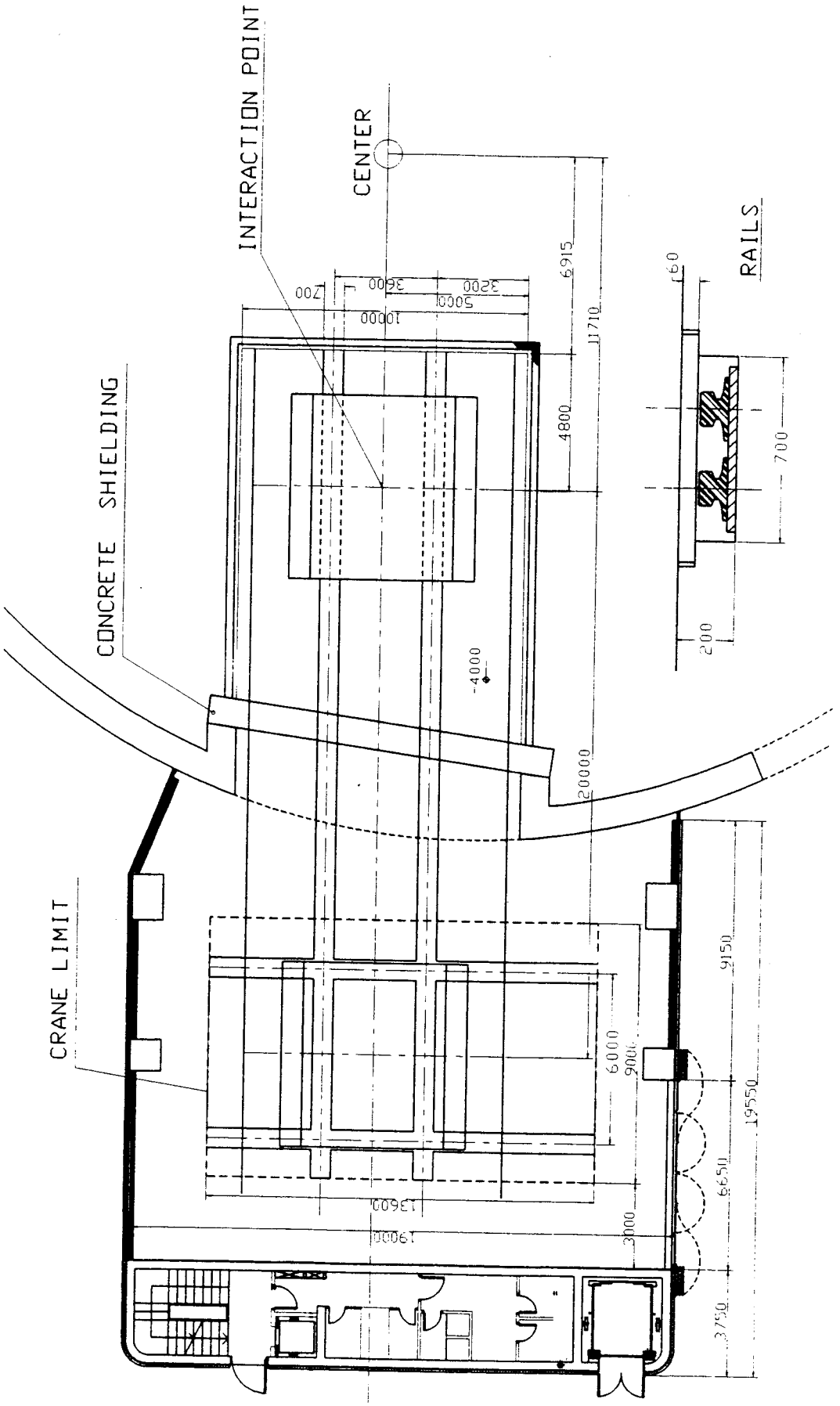

Fig. 3.4. Assembly hall and pit, plan view.

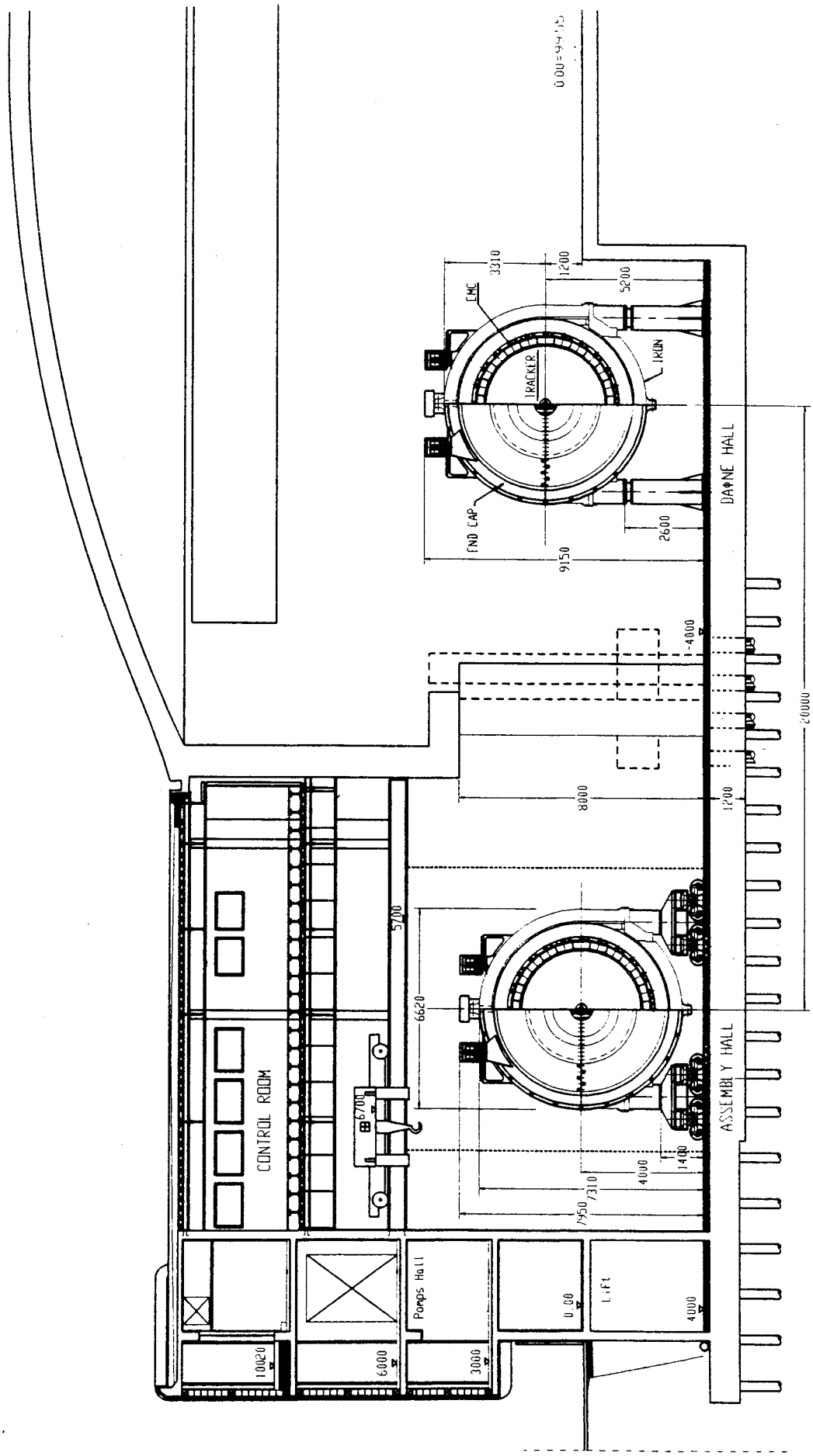

Fig. 3.5. Assembly hall and pit, elevation.

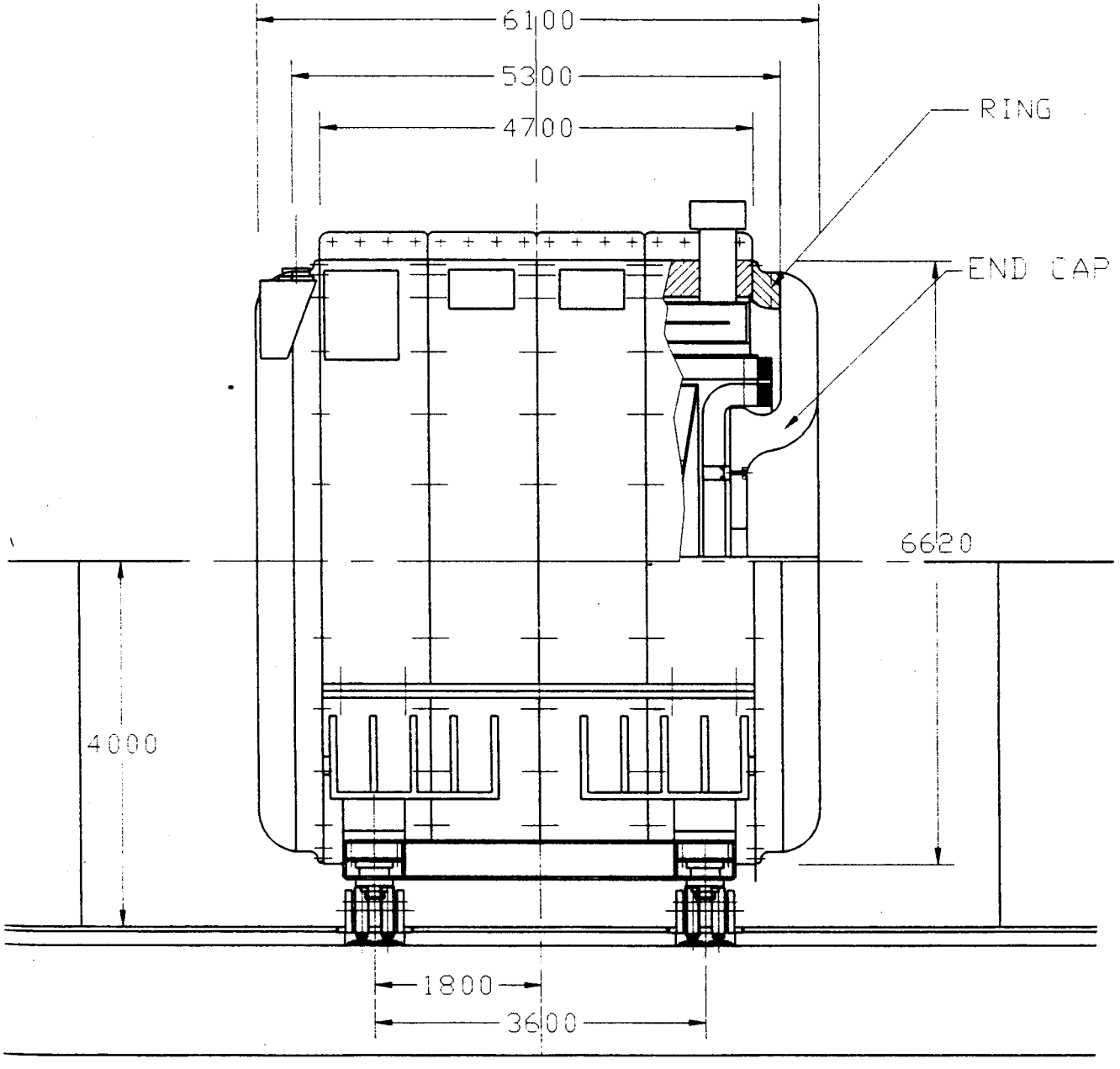

Fig. 3.6. The KLOE detector, assembled, side view.

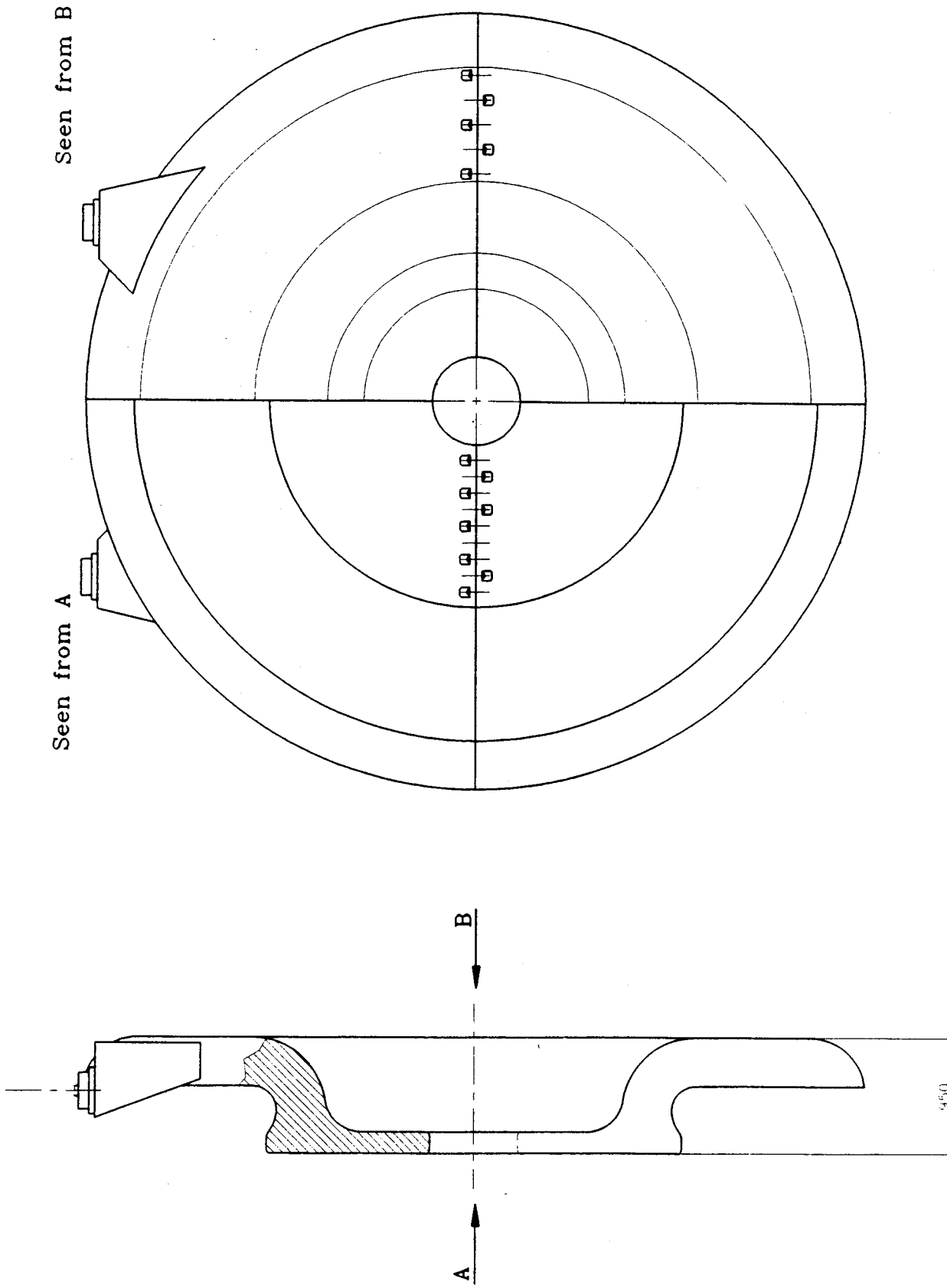

Fig. 3.7. Iron yoke, end-cap.

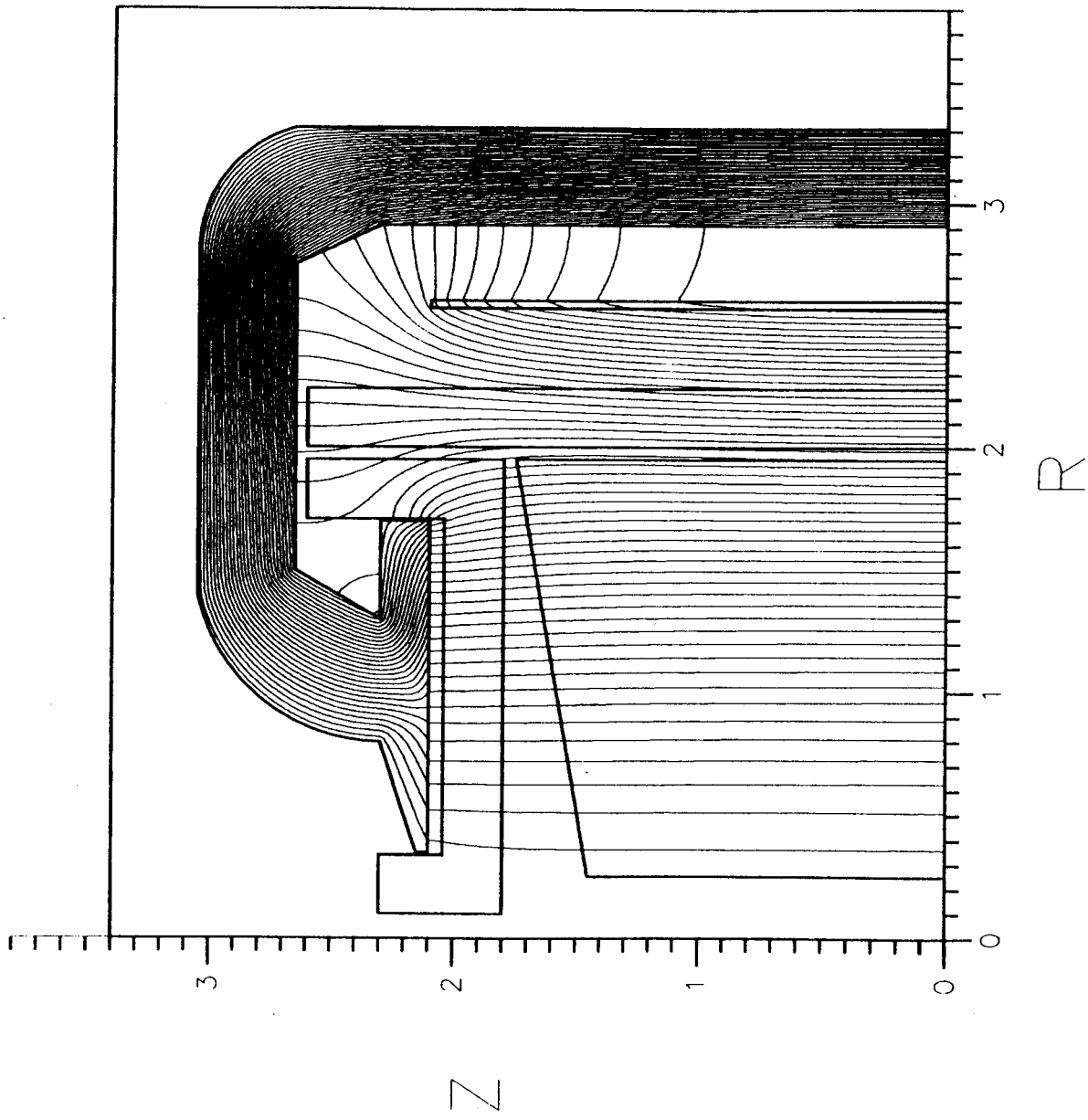

Fig. 3.8. Field map in KLOE.

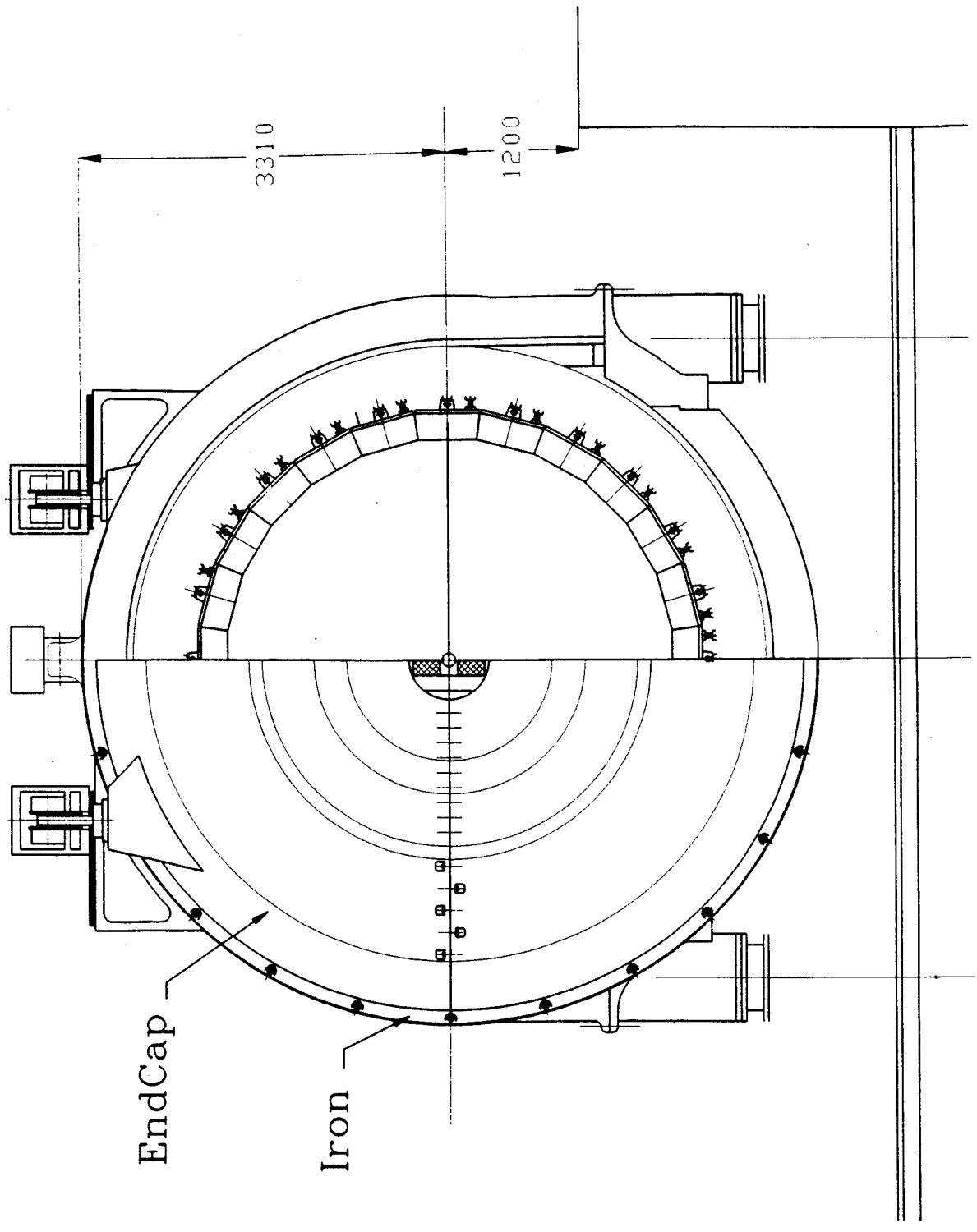

Fig. 3.9. Detector at beam height, in the pit.

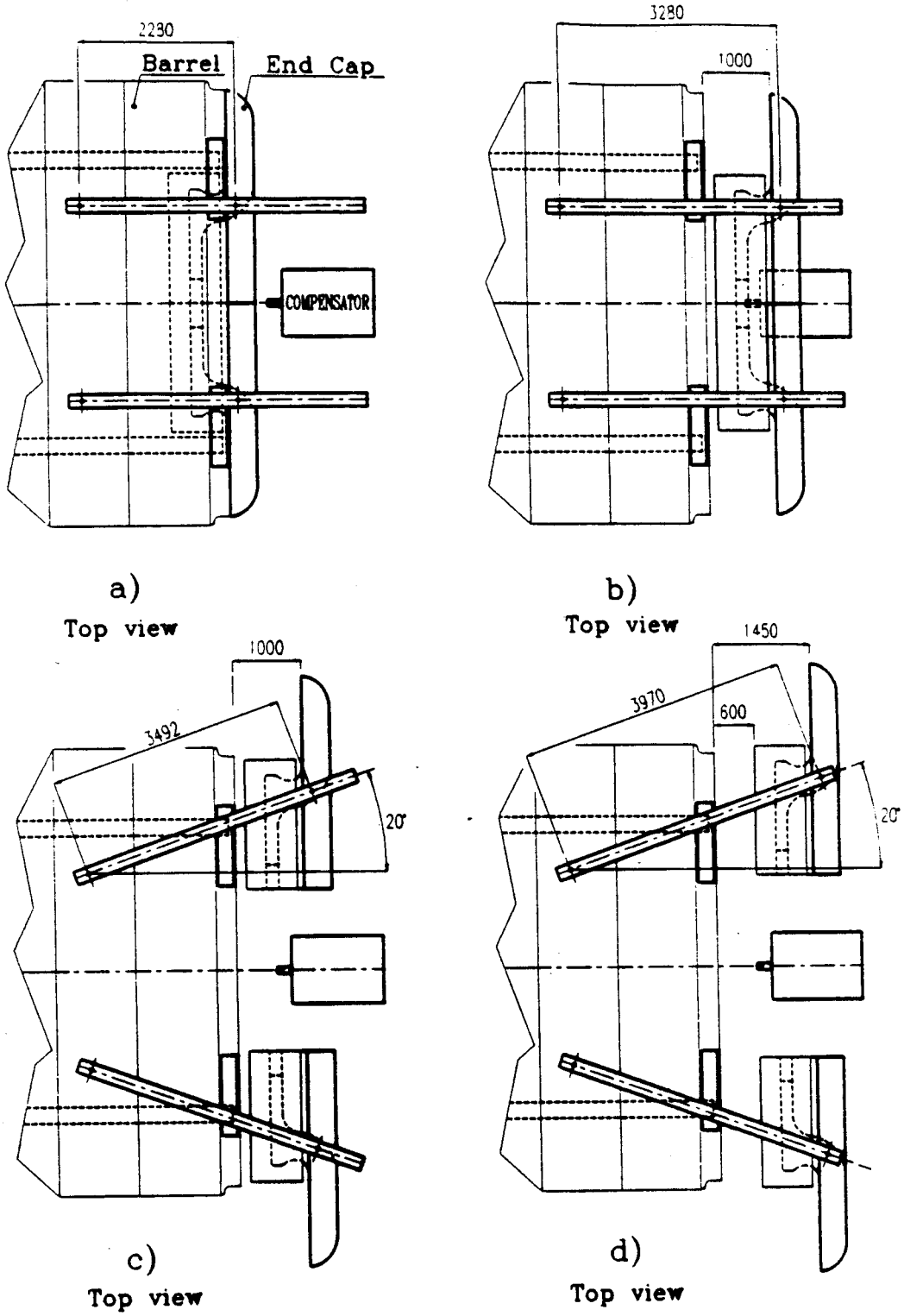

- a) In closed position
- b) Displaced up to the compensator
- c) After rotation of the supporting beams
- d) Maximum opening

Fig. 3.10. End-cap opening sequence.

4. ELECTROMAGNETIC CALORIMETER

4.1 Introduction

As anticipated in sections 2.2 and 2.5, the EmC performs three important tasks.

1. Determine the vertex of 110 MeV/c $K^0 \to \pi^0\pi^0$ decays, with an accuracy of a few mm.
2. Have a high discriminating power between $K_L \to \pi^0\pi^0$ and $K_L \to \pi^0\pi^0\pi^0$ decays.
3. Provide a first level trigger for the detector.

Moreover, these tasks have to be performed while keeping the contribution to the systematic error on $\Re(\epsilon'/\epsilon)$ below 5×10^{-5}.

As discussed in section 2.2, we propose to build a sampling EmC, using very thin ($\simeq$0.5 mm) lead grooved foils and scintillating fibers,[12] with a high granularity read-out. Fibers have been chosen for their superior timing properties,[13,14] and because they are convenient for building homogeneous structures with an (almost) arbitrary granularity. The lead-fiber composite can also be bent into the required shapes. Simulation studies and extensive measurements on prototypes,[14,15-18] demonstrated the high performance of our choice for the EmC.

1. It is fully efficient for photons, down to γ energies of $\sim$20 MeV.
2. It has good energy resolution: $\sigma_E/E \leq 5\%/\sqrt{E}$.
3. It allows the determination of the γ conversion point with an accuracy of $\sim$1 cm, adequate for the reconstruction of the K^0 decay point from the photon arrival times.
4. It has excellent timing performance: $\sigma_t \sim 50$ ps$/\sqrt{E\ (\mathrm{GeV})}$.[16]
5. It allows the construction of a hermetic calorimeter.

4.2 Calorimeter Layout

4.2.1 Calorimeter structure

The KLOE calorimeter is built by embedding 1 mm diameter polystyrene based blue scintillating fibers, between thin grooved lead foils, obtained by plastic deformation of $\sim$0.5 mm thick lead foils, fig. 4.1. Fibers are glued[19,20] to the foils, and run parallel to each other with a pitch of 1.35 mm. When layers are superimposed, fibers are located at the vertices of adjacent quasi-equilateral triangles, forming a structure which has a fiber:lead:glue volume ratio of 48:42:10 and a sampling fraction of $\sim$14% for a minimum ionizing particle.

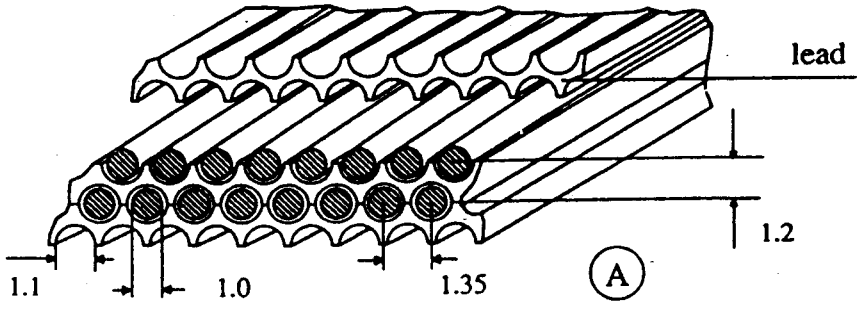

Fig. 4.1. Fiber and lead layout.

The resulting composite, which has a density of ~5 g cm^{-3} and a X_0 of ~1.5 cm, gains considerable stiffness and can be machined to any form. The mechanical properties of the composite have been measured[21] on several samples, following the UNI standards for composite plastic structures. The tested samples yielded consistent results, showing a predictable behavior to elongation, shear and compression loads. The unit yield load, 60 $N \times mm^{-2}$, agrees well with the value which has been calculated, using the mechanical properties of the components (lead, fibers, glue).

4.2.2 The Barrel EmC

The barrel EmC covers the polar region $49° < \theta < 131°$. It consists of 24 equal modules, forming a roman arch with inner radius ~2 m. Each module is 5.1 m long (the sensitive part is 4.5 m, to provide overlap with the end-caps) and has a thickness of 24 cm, for a minimum of 15 X_0. The thickness was chosen to prevent leakage, at the energies of interest, from degrading the energy resolution. The fibers run parallel to the beam, fig. 4.2. Each module contains ~400 km of scintillating fibers and weighs ~3.2 tons. At both ends, plexiglass light guides, formed by a tapered mixing part and a Winston concentrator,[22] take the light from fibers to PM's. The read-out granularity is 3.5×3.5 cm^2, for the first 5 read-out layers, and becomes 7×6.5 cm^2 in the back. The choice of granularity was driven by the following considerations.

1. Provide good position resolution in the r, ϕ coordinates, needed for good reconstruction of the K_L neutral decay vertex. The photon conversion point is measured in the transverse plane with a precision at least equal to the read out granularity $\times 1/\sqrt{12}$ cm, *i.e.* ≤ 1 cm. The z-coordinate is determined to ~2.5 cm on average, by the time difference measured at the two ends.

2. Allow range measurements in order to obtain some π–μ separation.

3. Make use of standard size, commercial, phototubes.

Light guides along the module sides have a trapezoidal cross section and a slightly bigger area. Every module uses 166 PM's, 150 of 1-1/8 inch diameter and 16 of 2 inch diameter, for a total of 3984 for the whole barrel EmC. In order to increase module stiffness and to allow for tracking chamber mounting brackets, a 0.5 mm thick steel skin is glued to the front face and the sides of the module and is bolted to a back-plate, which also carries the bushings to suspend the modules. At both ends the skin becomes a light tight box, which encloses the light guides and the PM's, fig. 4.3. A flow of nitrogen provides cooling and PM protection from possible He leaks from the chamber.

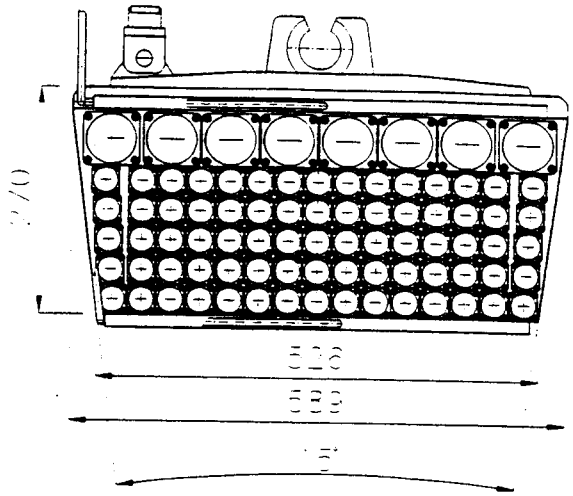

VISTA DA 'A'

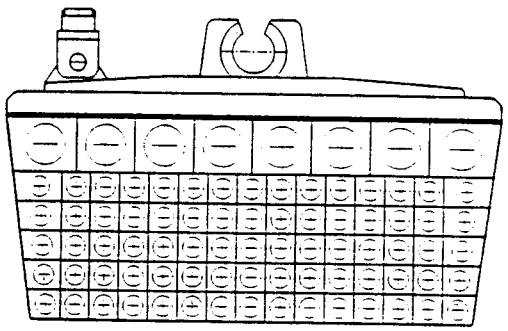

SEZ. B-B

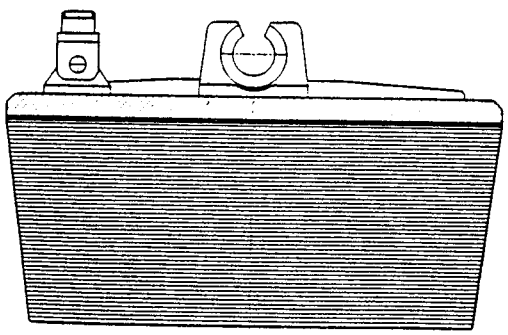

SEZ. C-C

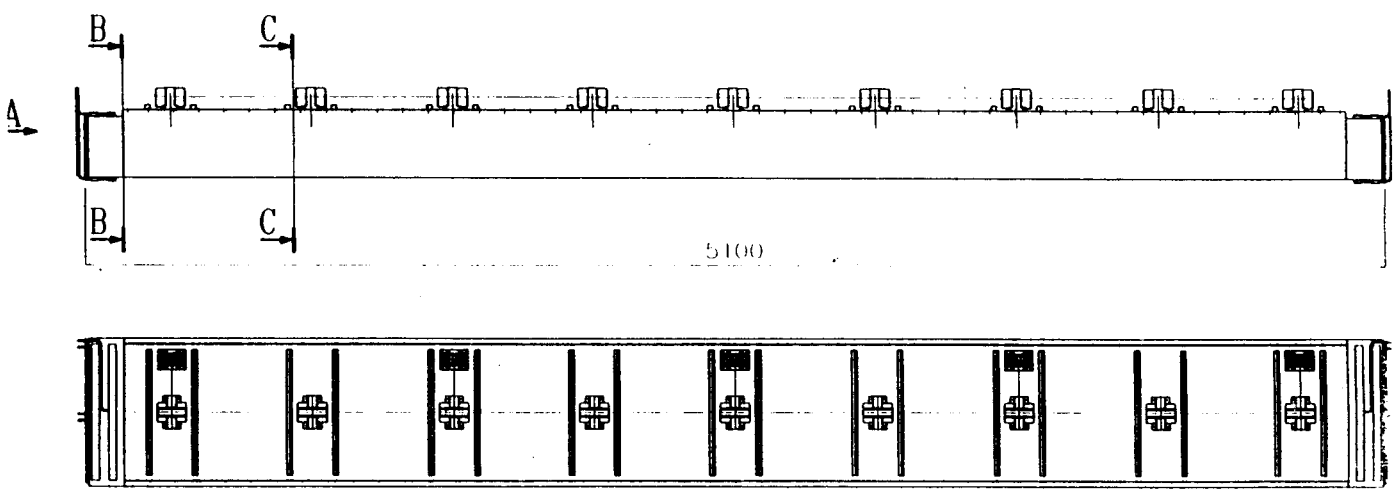

Fig. 4.2. Barrel Structure.

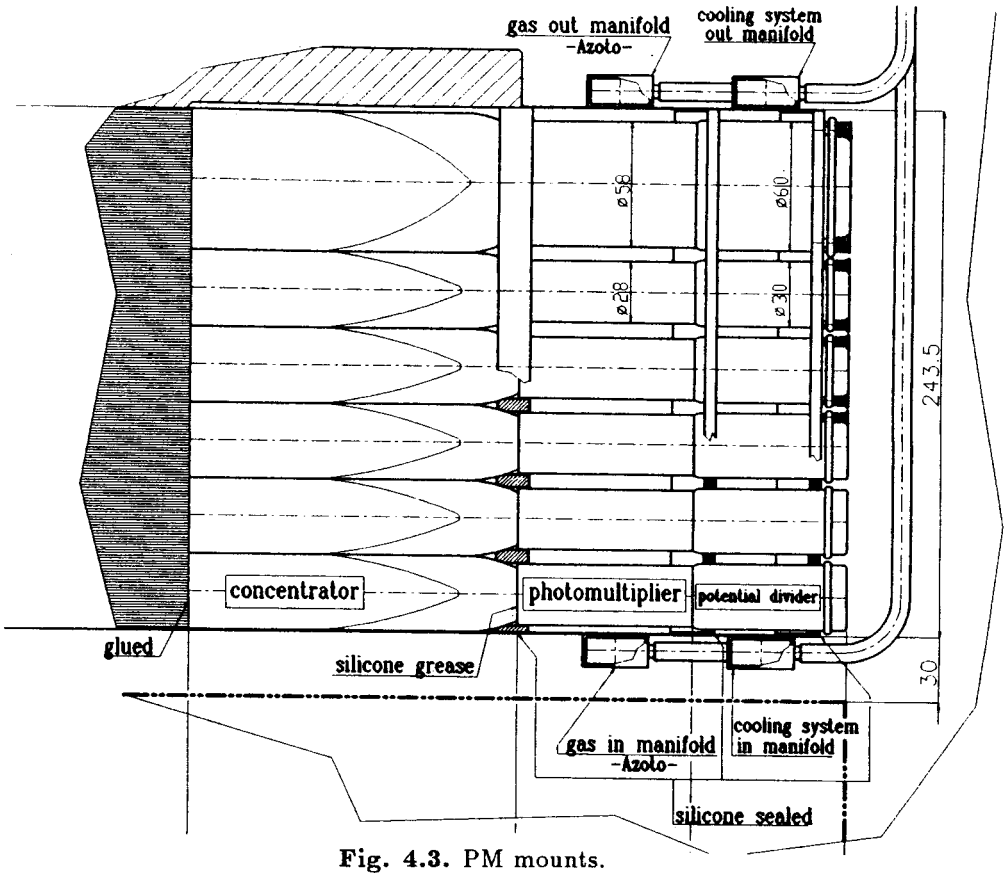

Fig. 4.3. PM mounts.

4.2.3 The End-Cap EmC

The end-cap EmC design has undergone a major change since the presentation of the KLOE proposal in April, 1992. This redesign effort has been driven by a number of considerations. The most important ones are given below.

1. Uniformity of construction and read-out over the whole EmC.
2. Reduction of the number of transition regions.
3. Appropriate orientation of the PM's in the magnetic field.
4. Modular construction.
5. Reduction of the insensitive area.
6. Reduction of the number of read-out channels.

Fig. 4.4 shows the layout of the end-cap. Its perimeter is a concave polygon, where modules run vertically, along the chords of the circle inscribed in the barrel. At the two ends they are bent at 90°, becoming parallel to the barrel ends. The end-caps are split into two halves, with the same structure, along the vertical diameter (see section A-A in fig. 4.4) leaving a 28×20 cm^2 hole for the beam pipe.

Appropriate overlap is allowed between the barrel and the end-cap, fig. 3.1, to reduce the escaping through the gap of γ's coming from the fiducial volume. The overall uninstrumented space is less than 1 %, which could be further reduced, by filling the cracks with fitted plugs. The two end-cap halves are attached to the magnet pole pieces, fig. 3.10, which are also split in two halves along the vertical. Every half weighs ~10 tons, and uses 1200 km of fibers. The read-out granularity is identical to the barrel. There are five 3.5×3.5 cm^2 elements and a tail catcher of 7×7 cm^2.

In the present configuration there are a total of 2580 photomultipliers, of which 2348 are 1-1/8 inch diameter and 232 are 2 in. With this modularity, we expect to have a position resolution in x and z of at least $3.5/\sqrt{12}$ cm, while the accuracy along y, determined by time differences, will be ~2.5 cm on average.

4.3 Component choice

4.3.1 Scintillating Fibers

The characterization of a wide variety of fibers commercially available has been carried out during the past months, along with a close interaction and feedback with the producers. The aim was to select fibers matching the minimal specifications required for the EmC (light yield in excess of 5 photoelectrons/mm at 100 cm from a bialkali photocathode, scintillation decay time τ_S~2.5 ns, attenuation length λ~250-300 cm, as well as to improve performance, reduce costs, guarantee uniform quality and timely delivery of the large amounts needed. Typically, the propagation speed of light in the fibers is ~0.17m/ns. Fibers were studied at both short, $1 < d <$ 100 cm, and long, $10 < d < 200$ cm, distance from the readout photomultiplier. Some results are given in table 4.1. A systematic study[18] investigated the properties of light transport at short distances from the PM's, also showing the role of glue in suppressing the light component which travels, by total internal reflection, at the cladding-air interface, which is characterized by very short attenuation lengths.

Measurements[23] made on 200 cm long fibers by several producers indicate the recent dramatic progress which has resulted in at least two types of fiber that match the required specification for the EmC. Use of fibers emitting in the blue-green region (Kuraray SCSF81, Polhitech 46) is a promising option, especially with a green-extended photocathode. At this point the main thrust is, while continuing to interact with producers to further optimize performance, to begin selecting vendors according to reliability, quality control and cost.

TABLE 4.1. Long fiber tests, bare fibers.

Fiber	λ_{peak}	τ_s	λatt	N_{pe}
	nm	ns	cm	100 cm
Bicron BCF10	430	2.4	220	5.1
Kuraray SCSF38	420	2.4	210	6.1
Kuraray SCSF81	420		260	5.4
Polhitech 42	420	2.4	250	5.2
Polhitech 46	460	2.4	270	5.8

The effect of removing with black paint and optical glue the contribution of the light propagating in the cladding on the attenuation curve in a plastic scintillating fiber is shown in fig. 4.5.

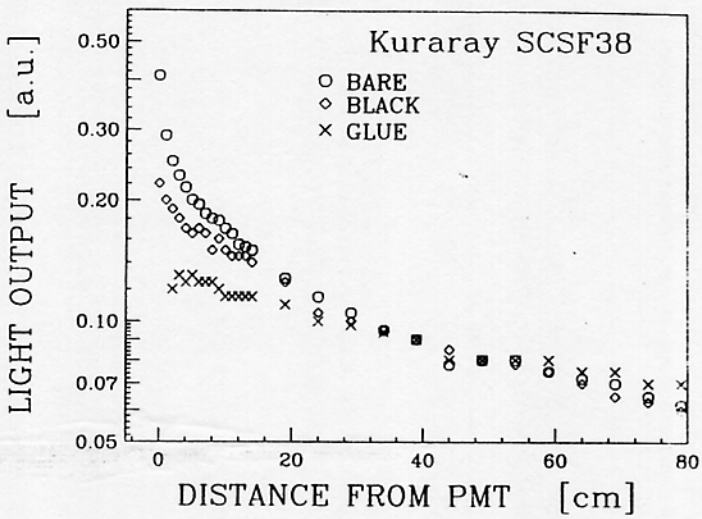

Fig. 4.5. Attenuation length in fiber core.

4.3.2 Light Collection

Since the timing resolution (and, to a lesser extent, the energy resolution) of the calorimeter depends on the number of photoelectrons, great care has to be put in maximizing the efficiency of the light collection. Another important design parameter is the uniformity of the PM photocathode illumination, to average out its response variations. The EmC light collection design exploits the fact that the refractive indices of fiber core, fiber cladding and plexiglass obey the relation $n_{\text{core}}/n_{\text{clad}} < n_{\text{plexiglass}}$. In this way it is possible to achieve considerable area concentration, without violating the Liouville theorem. Plexiglass guides, 20 cm long, consisting in a tapered mixing part and a Winston[22] cone with an area reduction factor of 2.7 have been built and used on the prototypes. Measurements indicate a transmission efficiency exceeding 93%, with the losses being mostly due to the glue interfaces. More work on prototypes and on simulation is in progress, in order to optimize the light guides design for the new mesh photomultipliers.

4.3.3 Photomultipliers

The expected magnetic field in the region where the photomultipliers will work is shown in fig. 3.8. The magnet return pole pieces have been designed in order to minimize the field component transverse to the PM axis. The residual field is found to have a transverse component not in excess of 0.4 kG. If the field intensity and the angle between the field and the PM axis are separately considered, they turn out to be lower than 2 kG and 30° respectively. Two types of "proxi-photocathode and mesh dynode" photomultiplier tube have been tested in a magnetic field: Hamamatsu R2490-05 and R3432-01; the first is a 2 inch, 16 dynode PM; the second is a 1 inch, 15 dynode PM. The R2490-05 is suitable for the outer part of the calorimeter while a new 1-1/8 inch Hamamatsu PM will be utilized in the inner part. The latter PM was not available at the time of the tests reported here. Measurements have been performed in Frascati, Roma-1 and Trieste/Udine placing PM's in magnetic fields up to 2.5 kG and at various angles, θ, between the field and the PM axis.

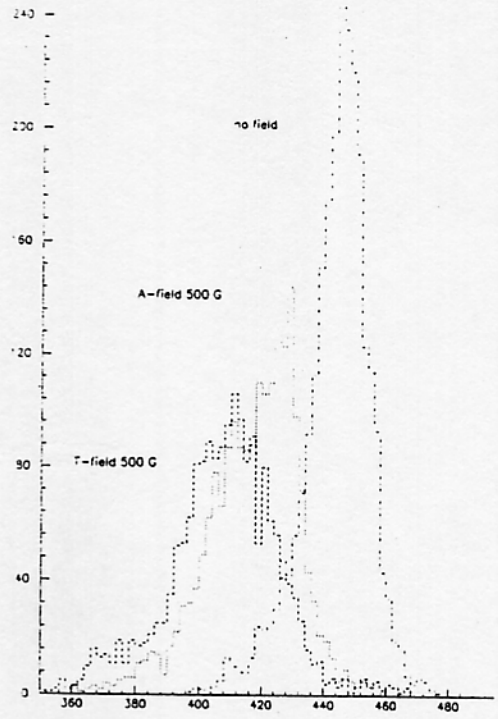

Fig. 4.8. Time response of the 1-inch PM.

4.4 Module Construction Tooling and Procedures

A set of tools have been designed and are under construction for mass production of the modules, in order to ensure a semi-automatic assembling of the EmC at reasonable costs and speeds, without loss of important performance parameters or requiring highly skilled manpower. The design is based on the experience gained in building the EmC prototypes and is aimed towards use of parallel fabrication, whenever possible.

4.4.1 Lead foils fabrication

Lead foils of ~4.7 m length and ~0.6 m width have to be grooved as in fig. 4.1, starting from a ~0.5 mm lead foil with considerable thickness variations across its surface. The groove shape and parallelism have to be kept under tight control, to avoid the deterioration of the calorimeter performance. An artist's view of the lead rolling machine (*lead–o–matic*) is given in fig. 4.9 The lead, supplied in reels, is first passed through a calibrator, consisting of two rollers to produce foils of even thickness and is then formed between grooved rollers. (fig. 4.10, b). The grooved rollers, made of hardened steel (Rockwell 60) and ground to shape by a sintered diamond tool, are mounted with ball bearings on a very rigid frame and can be aligned/checked with a set of micrometers (fig. 4.10, a). After the lead is formed, it enters a cleaning station, where lubricating agents and dirt are taken away by means of a set of brushes in a solution of alcohol and water, it is dried with a compressed air squeege and finally rolled on disposable cardboard tubes. When the desired length is reached, a travelling cutter automatically enters into operation, with no need to stop the chain, (fig. 4.10c). The rolled foil is then removed and a new cardboard reel is readied to accept the next one. Appropriate sensors and feedbacks are used along the path, in order to control process synchronization. A prototype of the *lead–o–matic*, capable of forming lead foils up to 15 cm width, has been built for use in the prototype

construction. Foils of almost 6 meter length have been produced, with a thickness uniformity of a few tens of μm and with grooves deviating from a straight line by less than 0.1 mm per meter of foil length. The operating linear speed is $\sim$3 cm/sec, which will allow us to produce the $\sim$200 foils needed for a module in less than 2 working days.

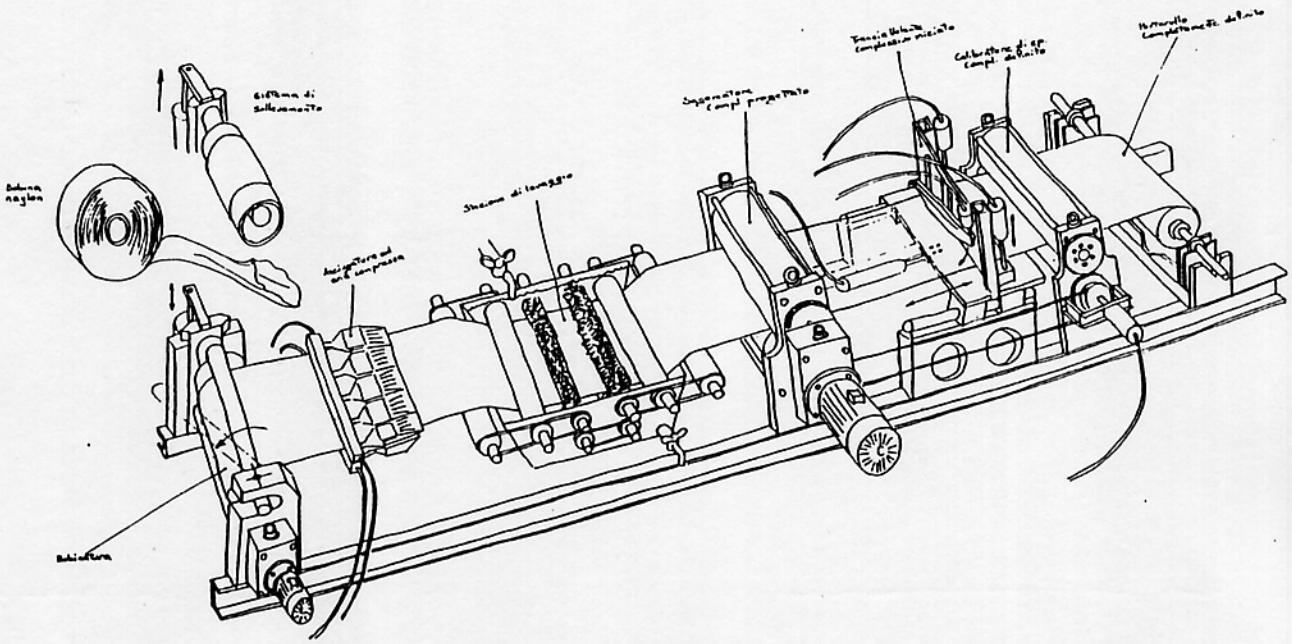

Fig. 4.9. Artist impression of the *lead-o-matic*.

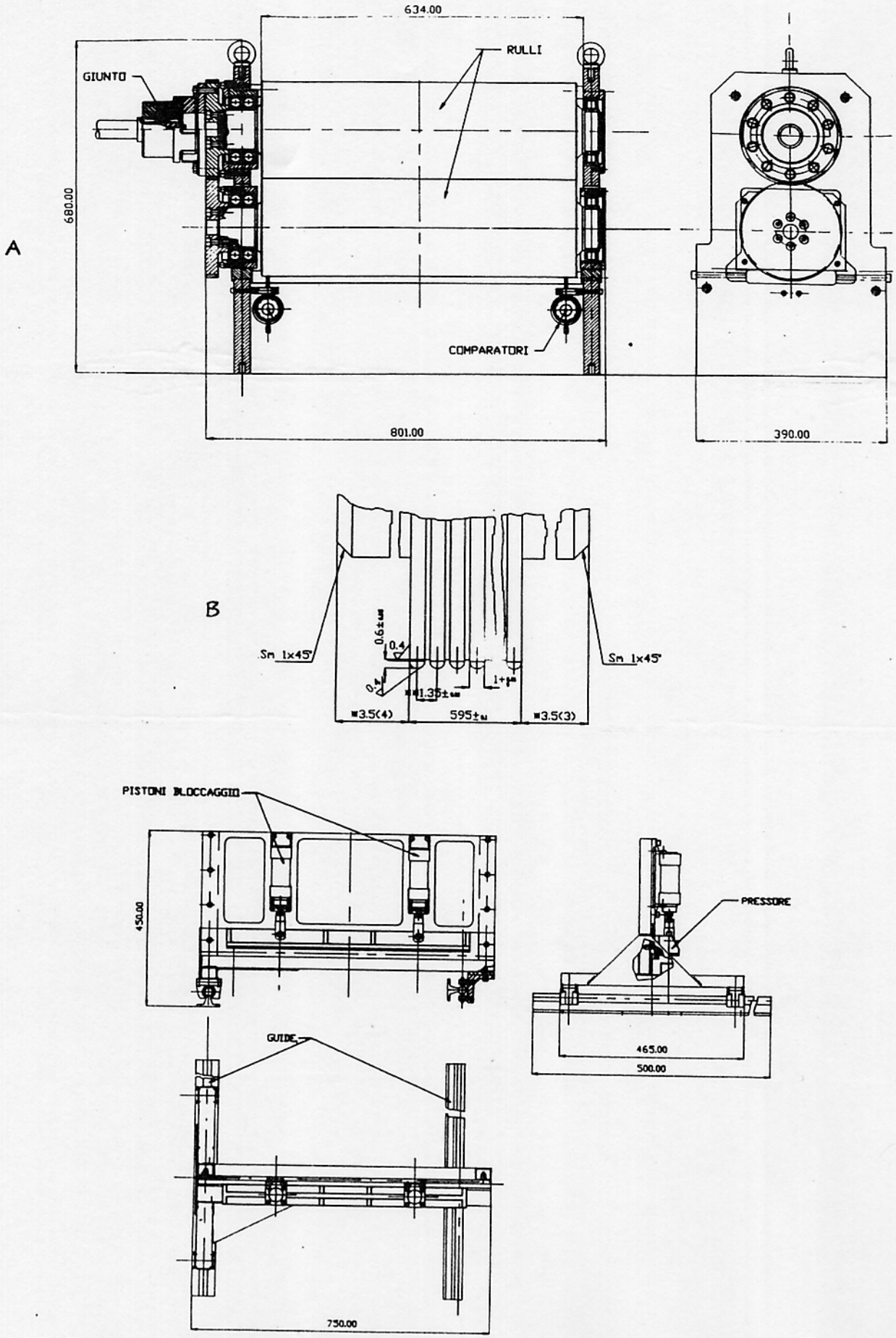

Fig. 4.10. Details of the *lead-o-matic*.

4.4.2 Assembly tools and procedures

Assembly procedures have been refined through the construction of several straight and curved EmC prototypes and have led us to the design of a set of tools for the various phases of the construction. Fig. 4.11 and fig. 4.12 show the devices used to lay down the lead foils, dispense the proper amount of glue, and to set the layer of fibers into the grooves.

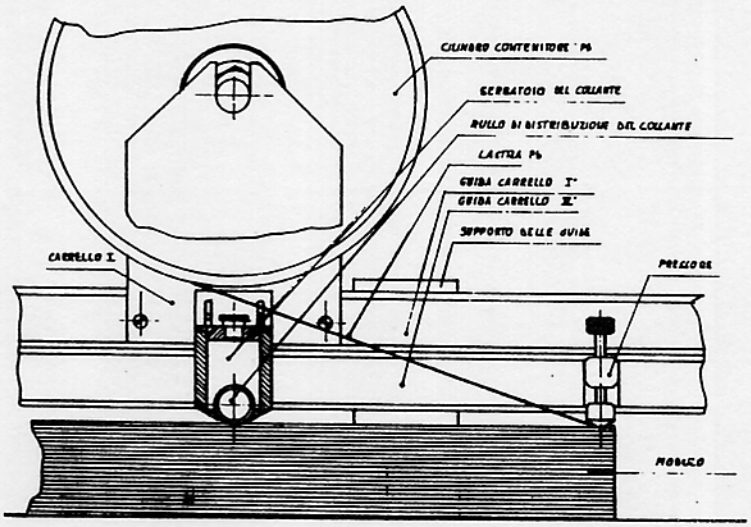

Fig. 4.11. Scheme for setting lead foils and dispensing glue.

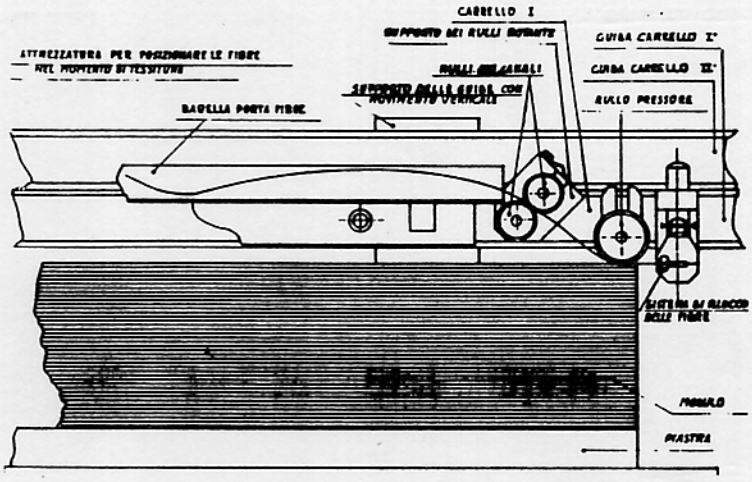

Fig. 4.12. Scheme for laying down the fibers.

All the devices slide on two sets of guides, and will be used alternatively in the module stacking. While the glue starts curing (~45 min), the stack is compressed under vacuum for 10 minutes, to apply even pressure and to sqeeze out excess glue. The EmC modules are built starting from the back, glueing the first lead foil to a 3.0 cm back-plate, which carries all the mounting fixtures. When the proper thickness is reached, the module is brought to a machining station, where all the faces are milled to their final dimensions. This milling machine, fig. 4.13, is designed by the Pisa KLOE group and is capable of milling the 4.5 m long faces at an angle, with a precision of 1/10 of a mm. When machining is completed, a 0.5 mm steel skin is glued

(under vacuum) to the module, and tightly bolted to the back-plate, forming a rigid box. After having allowed for adequate curing time, the module is clamped at the center to a pivoting jig, and rotated to a vertical position. This is done in order to perform the glueing of the light guides on a horizontal surface. Once the guides are set on one side, the module is flipped 180° and the other set of guides can be mounted, after having aligned them to the corresponding ones by means of a light source. Then the PM's are mounted, electrical connections are made, and the module is made light tight. The PM's are coupled to the guides with optical silicon grease, through a centering plate and are spring-loaded to ensure a good contact (fig. 4.3).

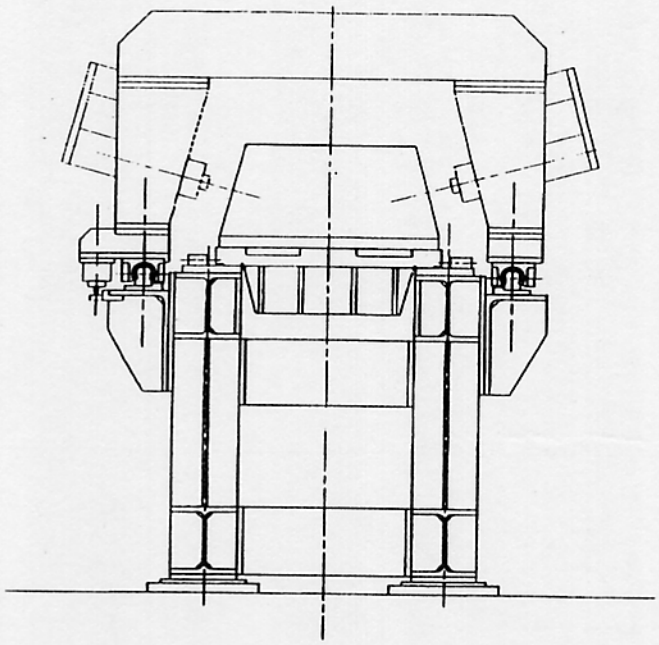

Fig. 4.13. Milling machine.

4.5 Calorimeter Assembly Mechanics

The assembly of the whole EmC has to avoid, as much as possible, cracks and/or inactive material, while having long term stability. We intend to exploit the structural properties of the lead/scintillating fiber composite to achieve these goals.

4.5.1 Barrel Assembly

Fig. 4.14 shows the mechanics of the barrel assembly. It consists of a number of cylindrical bearings, attached to the module back-plate, which can slide on guides mounted on a cylinder of adequate stiffness (which could be either the cryostat itself, like in the ALEPH experiment, or a separate structure attached to it), while a set of adjustable rods counteract the torque due to gravity.

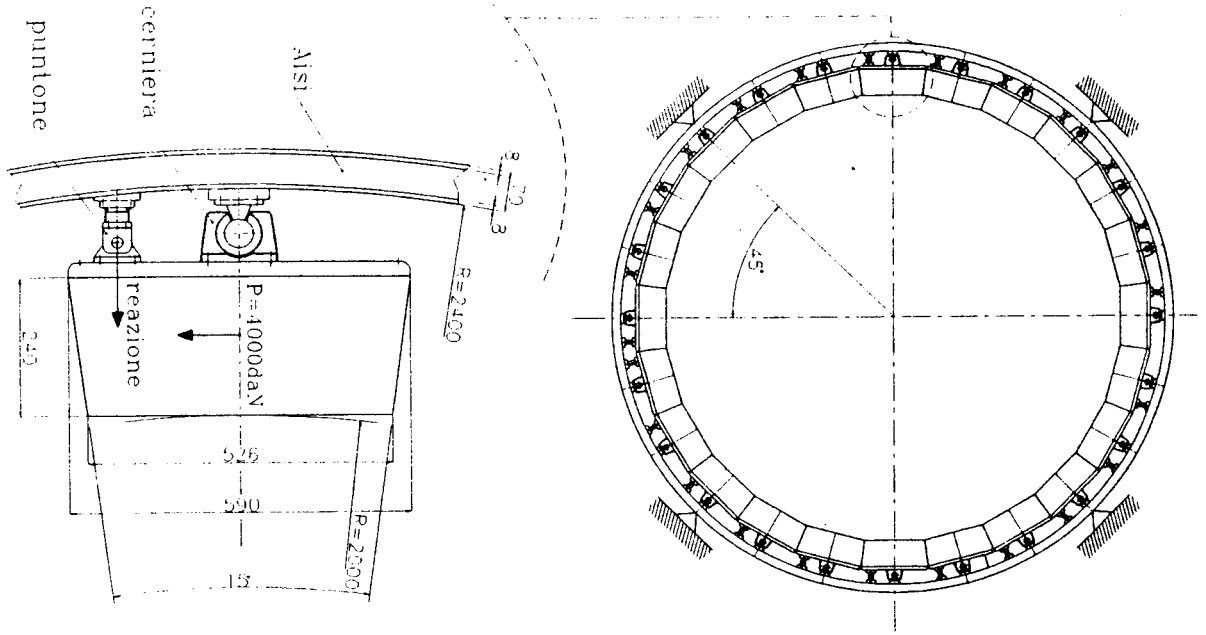

Fig. 4.14. Barrel assembly mechanics.

The barrel is assembled from the bottom module upwards. The inter-module clearances can be minimized, by adjusting bearing positions and rod lengths. Such a procedure will necessarily lead to a build up of small errors. We correct for them by machining the last (keystone) module to fit. Preliminary finite element analysis of the scheme of fig. 4.14 shows that the maximum deformation of the structure is fewer than 1 mm, and that shear and compression loads on the modules are at least one order of magnitude lower than the limits measured[21] for the composite.

4.5.2 End-cap Assembly

The assembly of the end-cap poses less problems, owing to the relatively low module weight and to the fact that modules can (partially) rest on the upper bent part. The end-caps need the possibility of moving them away from the iron pole pieces, to allow for PM servicing. A possible scheme is based on shafts (fig. 3.1), connected to the back-plates, which will go through holes in the iron pole pieces and can be used to push away the end-caps, once the iron end walls are open. Preliminary studies have shown that a small force ($\sim$60 kg) is sufficient to move a sector of $\sim$42 cm of the end-caps, if proper friction reduction methods are employed between the shafts and the holes.

4.6 Prototype Construction

4.6.1 Planar Prototypes

R&D work began in 1991, by building several small ($9\times9\times20$ cm^3) blocks, which gave us important insights on the construction techniques and on the performance.[26–28] A calorimeter module of external dimensions of $14\times24\times203$ cm^3, for a total thickness of $\sim15\ X_0$, was then built to set up construction procedures and to have a realistic proof of the final EmC performance. The calorimeter consists of 207 lead and scintillating fiber layers for a grand total of ~21450 fibers and a total weight of ~330 Kg. The fibers used were Kuraray SCSF-81 in the first 3.5 cm of the calorimeter and SCSF-38 elsewhere. The prototype was assembled in the LNF mechanical shop during a 3 week period in May 92. The grooved lead foils were produced with our first home-made rolling machine (the small *lead–o–matic*) starting from ~0.5 mm thick lead foils. The calorimeter is wrapped in a 1 mm steel skin of in order to simulate the final design in the experiment and to provide protection for the module. The optical readout is organized into 22 elements for each side: five layers of 4 small elements, 3.5×3.5 cm^2, and two large rear elements, 6.5×7 cm^2. On each side the light is transported, from the calorimeter to the 1-1/8 in diameter Hamamatsu 1398 photomultipliers, through 20 light-guides consisting of a $3.5\times3.5\times18$ cm^3 mixing piece and a Winston cone concentrator. The total area concentration factor is ~2.7. The rear elements are read out through a conical light guide from the 6.5×7 cm^2 area to a ~5 cm diameter Philips 2061. The area concentration factor is ~2.5. The calorimeter has been tested in a beam at the Paul Scherrer Institut, Villigen, Switzerland, PSI, and with cosmic rays. Furthermore a number of calorimeter elements, 3.5×3.5 cm^2 and ~5 m long, have been built using three type of fibers, chosen following our tests. They are presently being studied with cosmic rays, in order to help in the final fiber purchase decision.

4.6.2 Bent Prototypes

The design of the end-cap EmC employing curved composites of Pb and scintillating fibers, as proposed in section 4.2.3, requires further study of the mechanical construction feasibility, in order to develop procedures to avoid damage and reduce stress of the fibers during bending. These issues are being addressed by an aggressive prototyping and testing program. We have built four prototypes with a bent structure.

1. The ARCO prototype has a semicircular shape with inner and outer radii of 24 cm and 39 cm respectively and a width of 7 cm, with the same inner structural details as the barrel prototype. Scintillating fibers embedded in glued lead foils were made to follow a circular shape with the bend axis parallel to the lead sheets and perpendicular to the fibers. The two ends were machined, polished and divided into 16 readout cells each with 3.5×3.5 cm^2 surface area each. The same type of light-guides were used as in the barrel prototype. The outermost 3.5 cm were constructed using SCSF-38 fibers while for the inner 10.5 cm SCSF-81 fibers were employed with the aim to compare their response. The ARCO has been tested with cosmic ray muons and in the PSI test beam.
2. Two "C" shaped prototypes with a 5 cm bend radius between the long straight section and the two short arms. The straight segments of the two prototypes have a square cross section of 3.5 cm and have a length of 50 cm and 60 cm respectively, while the bent arms are 20 cm long. The "C" shaped prototypes have been tested with cosmic ray muons.

3. The "claw" prototype is a monolithic 100 cm long, 7.0 cm wide element bent 180° at one end into two separate 3.5×3.5 cm^2 cells with radii of 5 cm and 10 cm respectively. The claw has been tested with cosmic ray muons.

Building these prototype has demonstrated for the first time the mechanical feasibility of building bent structures over small radii without evident fiber damage. Two assembly procedures have been successfully tested:

1. Lead foils and fibers are assembled and glued on a flat bench, to a thickness of 1-2 cm. Before the glue begins to cure (~30 minutes) the element is placed on the proper form and bent.

2. Lead foil are assembled, alternating with fiber layers, directly on a bent form.

Both procedures have shown no damage of the fibers. The final quality of the fibers after the assembly and glueing process is visually inspected after the end faces are milled and polished. The claw prototype proves that it is possible to build the end-cap structure from single 28 cm to 60 cm wide modules, with slit ends, shaped as needed. This solution minimizes cracks between submodules and simplifies handling and mounting on the magnet iron pole pieces.

4.7 Results on prototypes

4.7.1 Test beam results on the barrel prototype at PSI

The module described in section 4.6.1 was brought to PSI and exposed in a test beam.[30] The primary goal was to measure the performance of a 4 m long calorimeter by using a 2 m long one. In order to do that, the response and the resolution of the calorimeter must be studied as function of the z position (i.e. along the fiber direction) using one side only. The energy resolution depends weakly on the z position because the fluctuations of the relatively large number of photoelectrons, N_{pe} is negligible with respect to the sampling fluctuations. The time resolution instead shows a strong z dependence since it depends essentially only on N_{pe}.

4.7.2 Test Beam experimental layout

The experimental layout used at the PSI test beam is shown in fig. 4.15 and consisted of:

1. A set of two scintillators (A,B) in front of the calorimeter, to provide (1) the proper time base, and (2) to define beam position and to identify particles by Time of Flight (TOF).

2. The calorimeter.

3. A moveable table (remotely controlled) for $y - z$ positioning.

4. The chambers used for the tracker prototype test.

The total amount of material in front of the calorimeter was equivalent to $\sim 0.2X_0$.

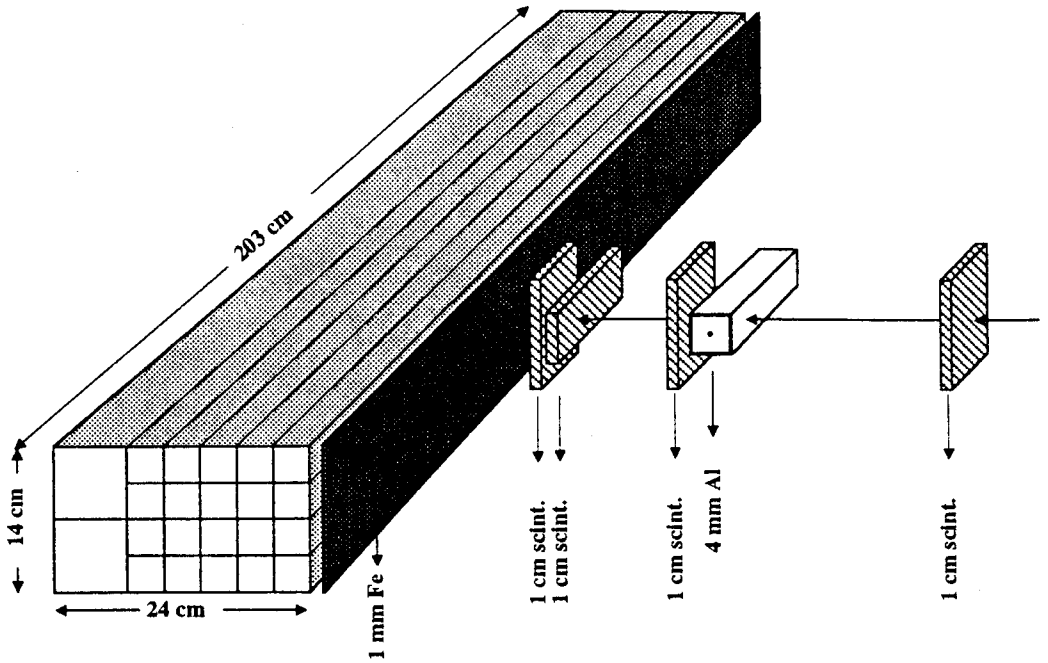

Fig. 4.15. Test beam setup at PSI

The PM outputs were connected, through 5 m of RG-58 cable, to active splitters. The two outputs of each splitter were sent to CAMAC ADC's and to low threshold discriminators. The discriminated outputs acted as TDC stops. The PSI machine is an isochronous cyclotron with an accelerating radio frequency, RF, of 50 MHz. It accelerates protons to 600 MeV kinetic energy. A secondary beam of π's, μ's and e's with momenta ranging from 150 to 300 MeV/c was delivered to our test area. A coincidence of the last two scintillators, fig. 4.15, was used to generate the ADC gates, and the "start" of the TDC system. The particle identification was done on the basis of the time of flight, TOF, using the RF signal as one of the TDC stops. The distribution of the RF timing is shown in fig. 4.16. Three distinctly separated peaks appear in this plot corresponding to the TOF expected for e , π and μ. The good particle identification achieved in this way is due to the long, ~22 m, flight path and the good time resolution, ~100 ps, of our counters.

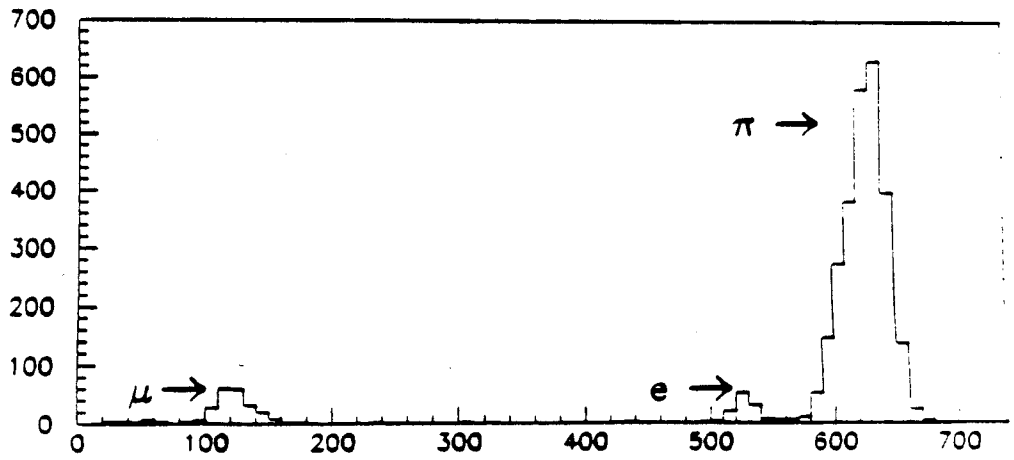

Fig. 4.16. TOF plot of pions, muons and electrons.

4.7.3 The definition of Energy response

In order to measure the resolution achievable in an array of several elements their relative gains (G_i) must be correctly taken into account. The gains are obtained by normalizing the charge (Q_i) collected in the i-th element for electromagnetic showers, with the signal (M_i) measured at the center of the module for muons, as minimum ionizing particles, MIP's. The total energy is therefore expressed in units of energy released by a muon in the basic cell by using:

$$E_n = \sum_{i=1}^{n} Q_i/M_i$$

The prototype is read out on both sides and therefore we can define the response for side A (E_n^A), for side B (E_n^B) and for both sides (E_n^{TOT}). To determine M_i we have oriented the calorimeter with the lead foils horizontally and taken data using a cosmic ray trigger, since the most energetic muons available in the beam had 250 MeV/c momentum and cannot be used as MIP's. The values thus obtained are used for all the further analysis.

4.7.4 Energy Response and Resolution for the Barrel EmC

The E_n^{TOT} distributions for e's impinging with normal incidence at the center of element 2 , after cleanup and for all different beam momenta, are shown in fig. 4.17.

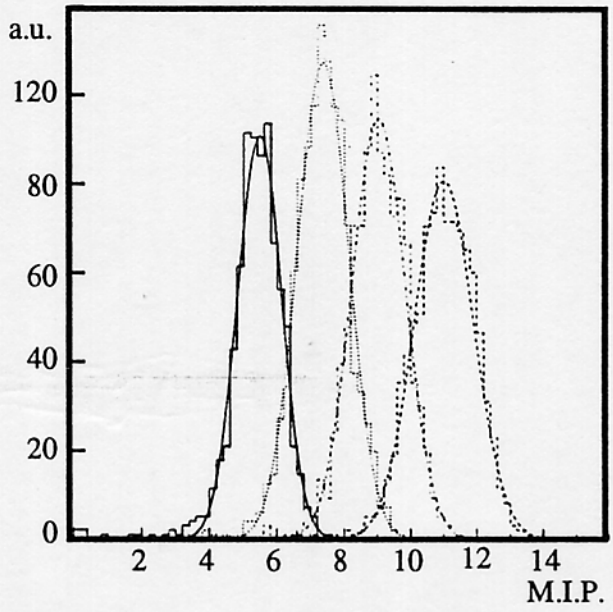

Fig. 4.17. The energy response for electrons

No tails are present in the plot and a fit to a gaussian gives an energy resolution of $\sigma_E/E \sim 4.5\%/\sqrt{E/\,(\mathrm{GeV})}$ fig. 4.18.

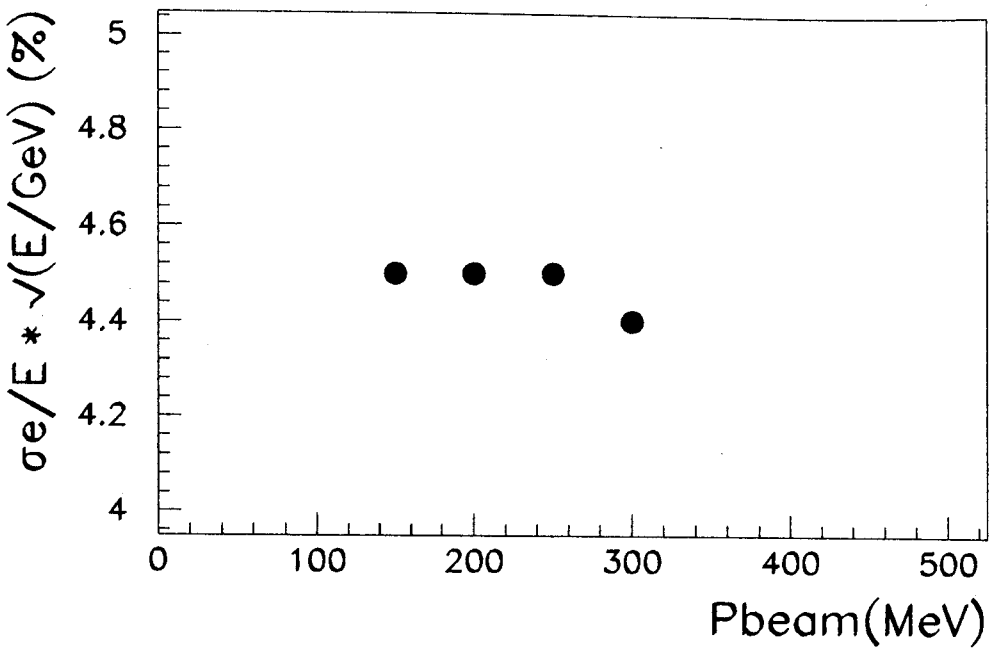

Fig. 4.18. The energy resolution for electrons.

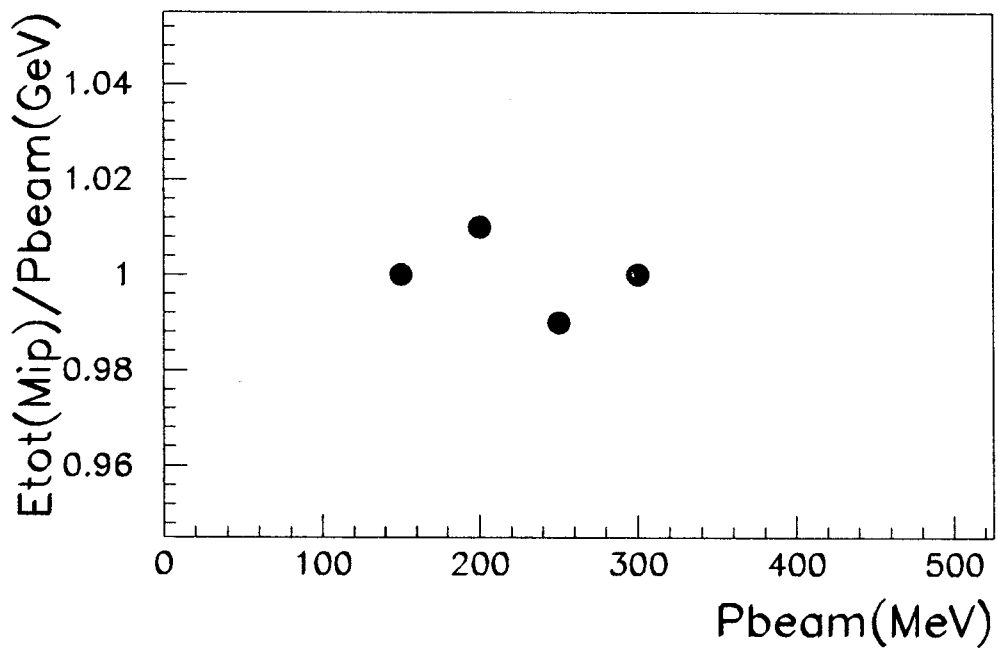

Fig. 4.19. Linearity.

The linearity of the calorimeter response is execllent, as shown in fig. 4.19. We have also studied the behavior of the calorimeter when particles were entering it at different angles. Fig. 4.20 shows the spectra of 250 MeV e's impinging on the calorimeter with an incident angle of 45°. The energy resolution is also $\sim 4.5\%/\sqrt{E/\,(\mathrm{GeV})}$.

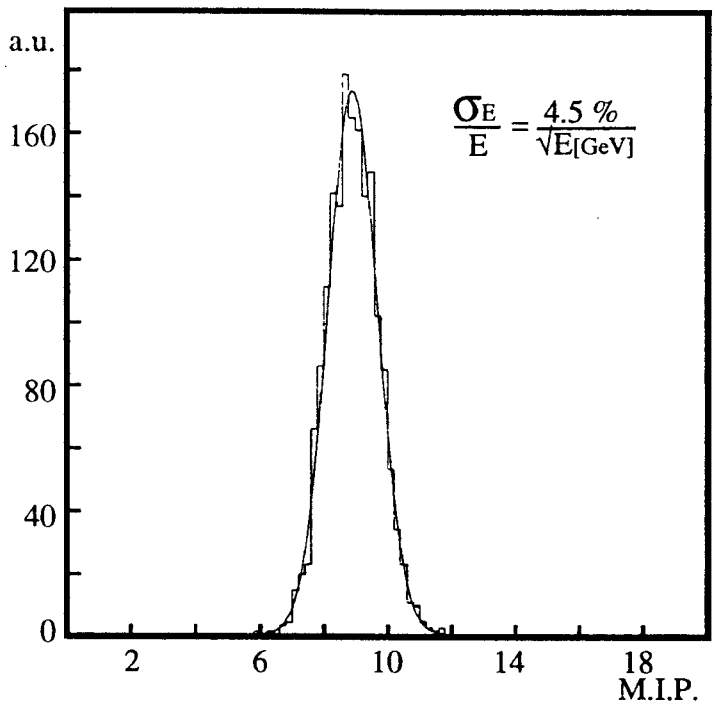

Fig. 4.20. Energy response for electrons at 45° incidence.

The response and the energy resolution, for 250 MeV/c electrons at normal incidence, as function of z and y have also been measured, where z is the distance between the beam impact point and the PM position along the fiber direction, and y is the distance between the beam and the calorimeter center along the vertical direction. Fig. 4.21-a and fig. 4.21-b show the distributions of the A and B sides. Each distribution has been fit to a single exponential function. The values obtained for the attenuation lengths are, respectively, λ_e^A=203 cm and λ_e^A=210 cm.

A similar distribution for 250 MeV/c μ yields an attenuation length λ_μ=170 cm.

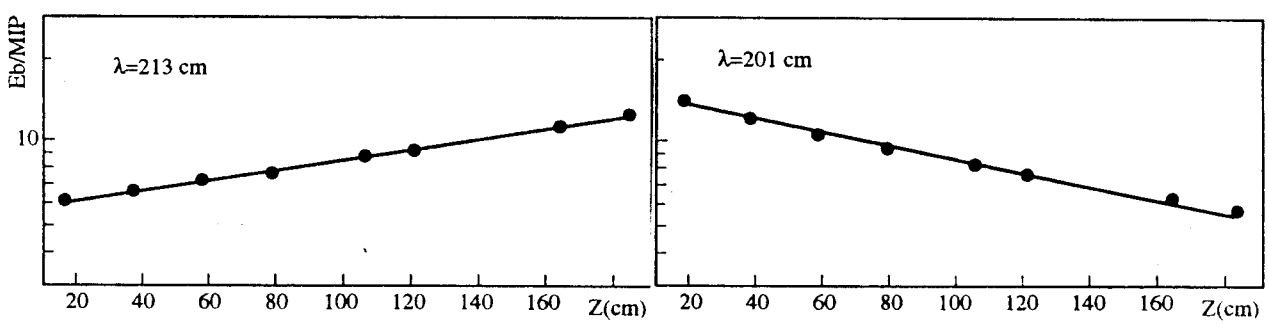

Fig. 4.21. Energy response along the module for electrons

The difference between the μ and e results is related to the different active material used in the prototype; the first longitudinal layer is consisting of SCSF-81 fibers while SCSF-38 are used elsewhere. These fibers have different λ_s, which can be readily measured using the μ data. In fig. 4.22 a and b, the average pulse height of the hit element for the first and the second layer is

plotted as function of z position. Typical multi-exponential behavior is shown by both types of fibers and we have fitted these by using a double exponential fit. The values of the attenuation length for the long component are: $\lambda_{38}\sim$1.9 m, $\lambda_{81}\sim$2.5 m.

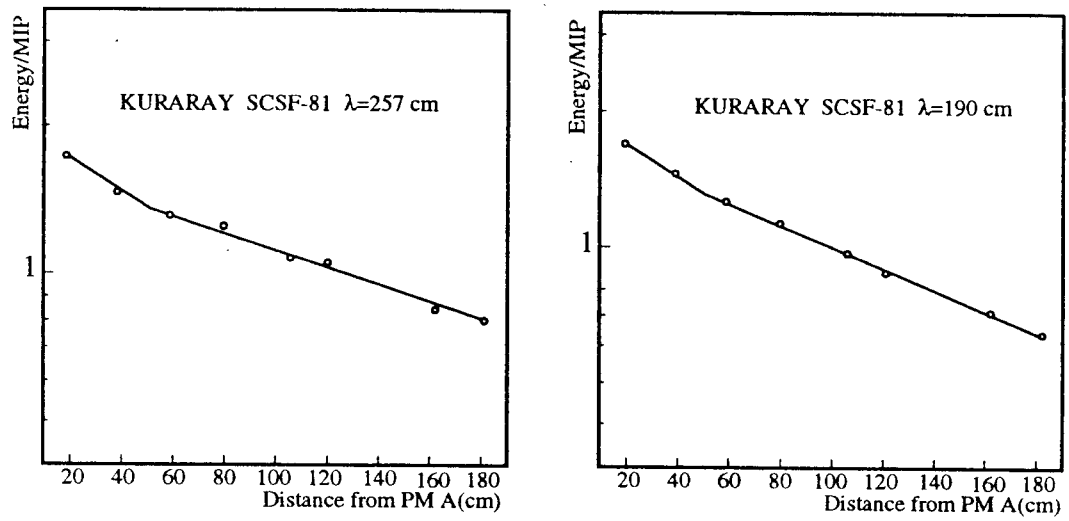

Fig. 4.22. Attenuation curves for SCSF81 and SCSF38 for muons.

The difference between λ_μ and λ_e is due to the convolution of the different energy profiles for electrons and muons with different attenuation lengths. In fig. 4.23 the distributions of E_n^A , E_n^B and E_n^{TOT} vs z are shown. E_n^{TOT} behaves as $\cosh(z/\lambda)$ and therefore reduces the effect of the attenuation length to a response variation of 10%. A 4 m long calorimeter built with SCSF-81 fibers will show differences in the total energy response along z of at most 30%.

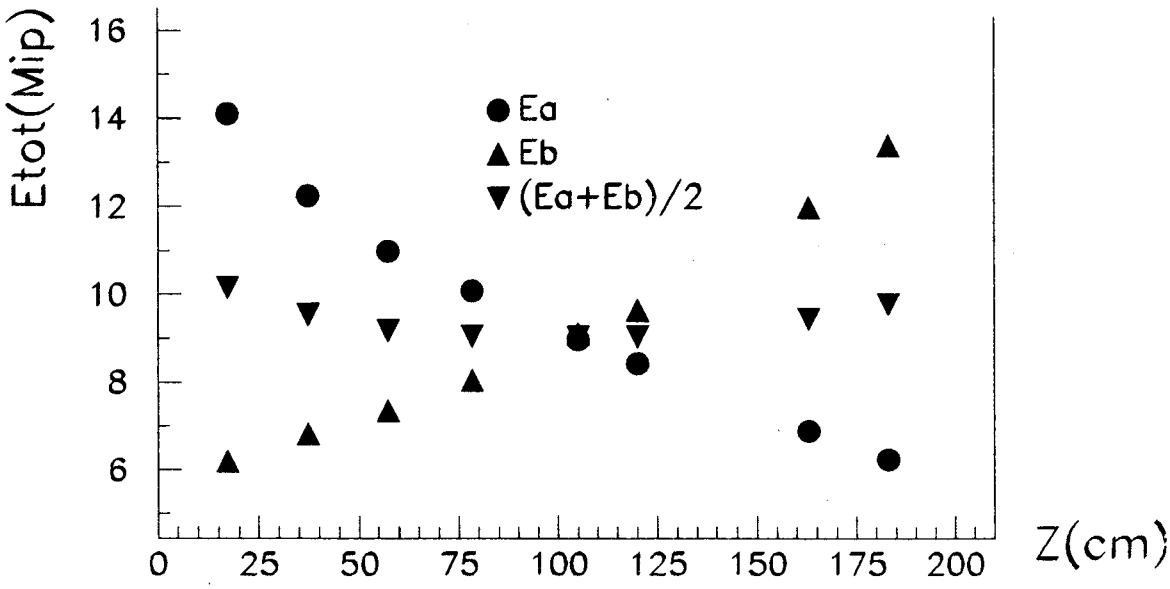

Fig. 4.23. Energy response vs distance for electrons for side A, side B and the sum.

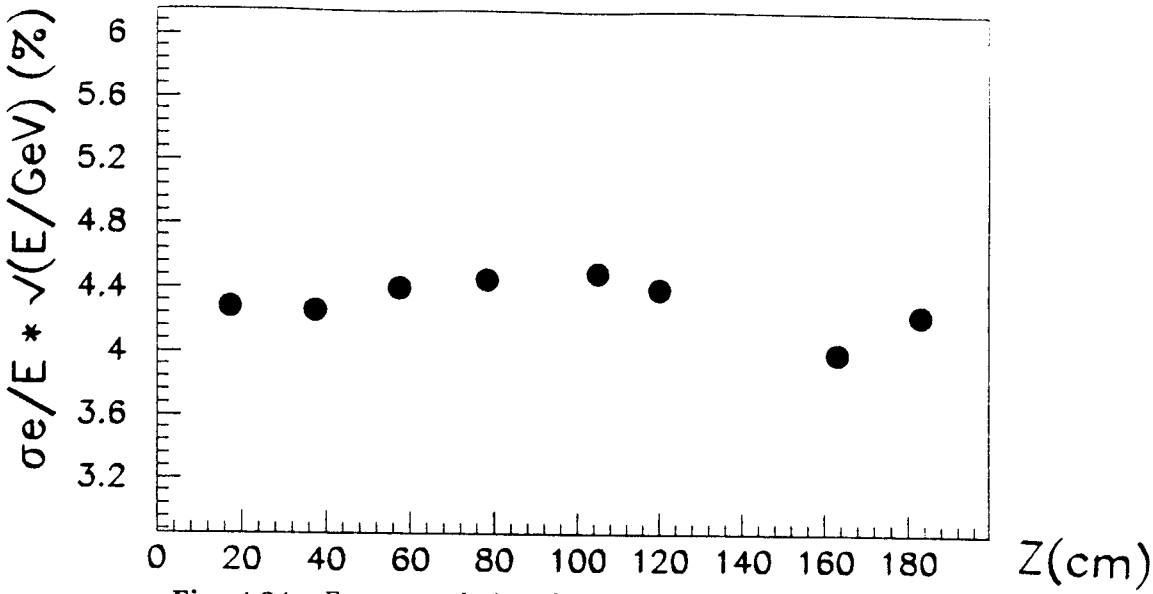

Fig. 4.24. Energy resolution along the module for electrons.

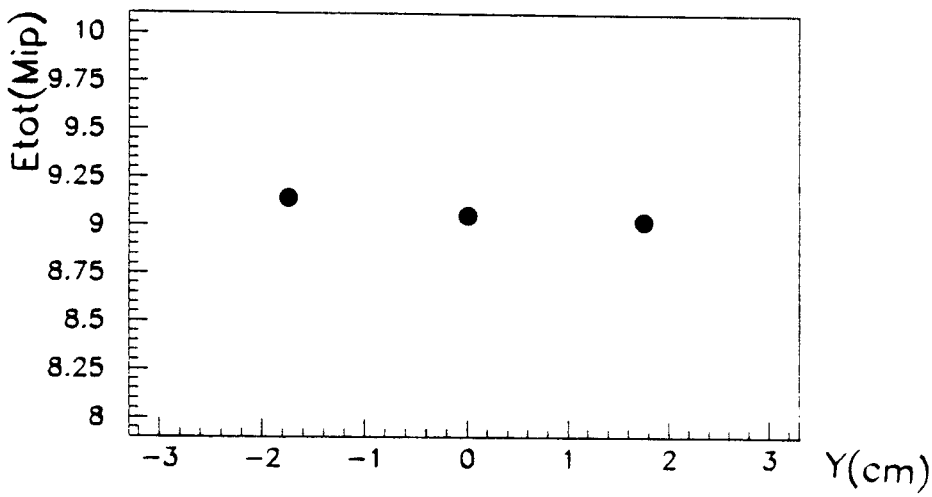

Fig. 4.25. Electron energy response for a vertical scan.

The energy resolution vs z is plotted in fig. 4.24. The resolution looks slightly better near the calorimeter ends, due to the higher light output (the contribution due to the phoelectron statistics is $\sim 1{,}6\%/\sqrt{E/\,(\mathrm{GeV})}$).

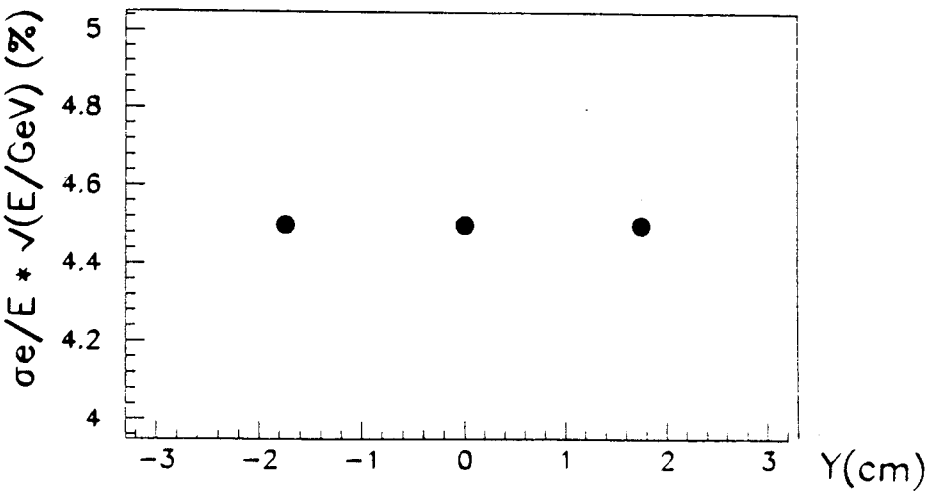

Fig. 4.26. Energy resolution, vertical scan, electrons

The result of a vertical scan can be seen in fig. 4.25 and fig. 4.26, where the response and the energy resolution are plotted respectively. The three points correspond to having the beam in the middle of element 2, in the middle of element 3 or in between the two elements. No appreciable differences are observed.

4.7.5 Time Resolution for the Barrel EmC

As mentioned before, the test beam goal was to measure the performance of a 4 m long calorimeter by using a 2 m long one. In order to do that the performance of the prototype should be measured using beam incident at one end and using the opposite side read-out only. The behavior of a 4 m calorimeter can then be inferred, knowing the λ_{att} of the fibers and the scaling law for using both sides, which can be written as:

$$\sigma_t^{(A+B)/2} \sim C \times \sqrt{\cosh(z/\lambda)}$$

Therefore to obtain the timing resolution for a 4 m long calorimeter we do the following:

1. Study σ_t for both muons and electrons, at different momenta, by using one side only.
2. Link σ_t for muons to σ_t for electrons.
3. Show that σ_t (obtained using A and B sides) scales at calorimeter center, at least, as $\sqrt{\sigma_{ta}^2 + \sigma_{tb}^2}\,/2$

We have analyzed μ and e runs of 150-200 MeV momentum, having the beam close to the side B and at calorimeter center. All the raw times were corrected for time walk, due to fixed threshold discriminators, and the t_0's were also subtracted.

The distribution of the timing obtained using one element only (T_{2A}) for 150 MeV μ incident on element 2 and at ~1.9 m away from PM A is shown in fig. 4.27. The distribution looks quite gaussian with no tails. After quadratically subtracting the contribution of the time base of ~ 65 ps, a resolution of ~306 ps is found.

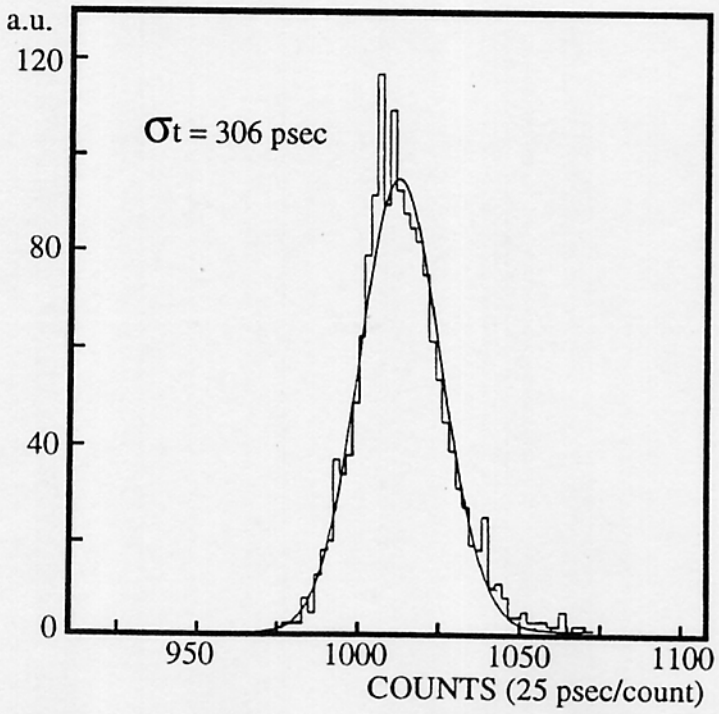

Fig. 4.27. Muon time distribution of a single calorimeter element, (side A).

The time resolution can be improved by averaging the times measured by more calorimeter elements, taking into account their statistical significance, by means of the energy weighted averaged time given by:

$$T_w = \sum_{i=1}^{n}((T_i' - T_i^0) \times E_i) \Big/ \sum_{i=1}^{n} E_i$$

A 150 MeV μ deposits energy in at most two calorimeter elements, with the bigger energy deposit in the first one and therefore the expected improvement should be less than $\sim 1/\sqrt{2}$. Fig. 4.28 shows the distribution of T_w^A for these events. Resolution is $\sim$ 240 ps.

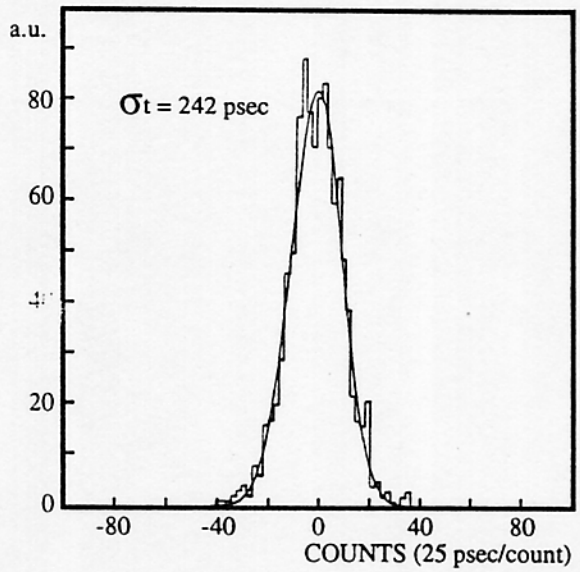

Fig. 4.28. Muon time distribution averaged over all the elements, (side A).

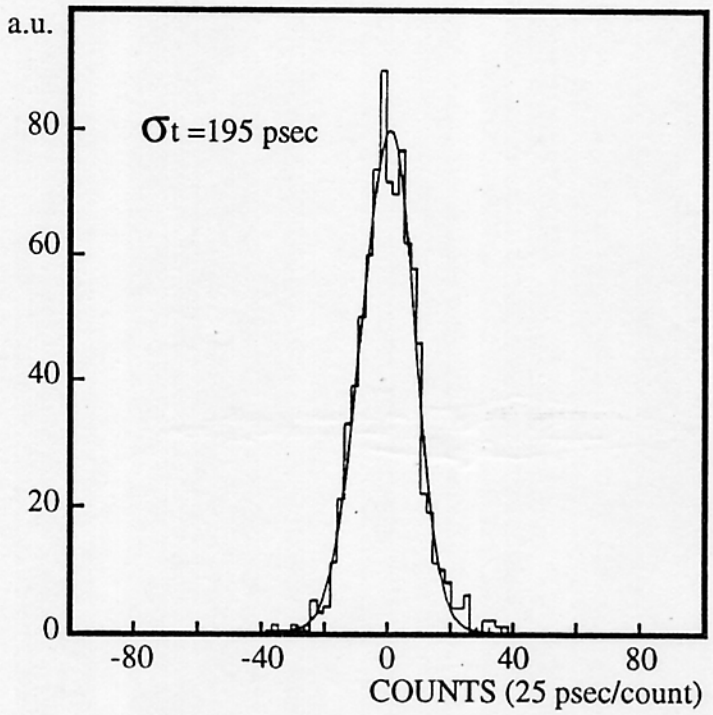

Fig. 4.29. Electron time distribution averaged over all the elements, (side A).

Fig. 4.29 shows the average time distribution at A, for 150 MeV e's incident at B. The

resolution is 195 ps. The averaging process is more complicated for electrons than for muons, because the deposited energies differ from element to element and more cells enter in the T_w average. The comparison of electrons and muon data will therefore help to understand systematics in the averaging procedure.

To connect μ and e data we must take into account the fact that, at these energies, both particles are fully contained in the calorimeter and that, therefore, the energy deposited in the active material (E_{dep}) is proportional to the kinetic energy (E_{kin}) of the particle. Using the (measured) e/μ ratio, which is $\sim$1.2, we can introduce the equivalent e.m. energy, E_{eq}^{em}, defined by the relations:

$$E_{eq}^{em} = 1.2 \times E_{kin}$$

for muons and

$$E_{eq}^{em} = E_{ele}$$

for electrons and then check whether the time resolutions for muons and electrons follow the "universal" curve

$$\sigma_t = k \Big/ \sqrt{E_{eq}^{em}}$$

At 150 MeV/c this formula agrees with muon and electron data. The kinetic energy of a 150 MeV/c μ is 78 MeV, scaling by the factor 1.2 gives $E_{eq}^{em}\sim$94 MeV. The expected ratio is therefore given by:

$$\sigma_t^{\mu}/\sigma_t^{e} = \sqrt{E_{ele}/E_{kin}} = \sqrt{150/94} = 1.26.$$

The measured ratio is 1.24, in good agreement with the parametrization.

TABLE 4.2. Time resolutions for μ and e.

Particle	P (MeV/c)	E_{eq}^{em}	σ_t^{meas}	σ_t^{theor}
μ(T02) on B side	150	51	207	225
μ(T02) on center	150	70	204	192
$\mu(T_w)$ on B side	150	94	171	166
$\mu(T_w)$ on center	150	130	164	141
$\mu(T_w)$ on B side	200	144	131	134
e (T_w) on B side	150	150	138	131
e (T_w) on B side	200	200	125	114
e (T_w) on center	150	207	124	112
e (T_w) on center	200	285	103	95

We have also checked how averaging the times of the A and B sides improves the timing. The T_w distributions for side B are shown in fig. 4.30 for 150 MeV μ's at the calorimeter center; the resolution is 181 ps. The same distributions, using both sides, can be seen in fig. 4.31, the resolution is 107 ps. The time resolution of the average scales slightly better than $\sqrt{\sigma_{ta}^2 + \sigma_{tb}^2}\,\Big/2$. Furthermore time resolution for side B looks consistently better than for side A, and this has been attributed, after a visual inspection, to a poorer coupling of the light guides on the A side. Assuming the same light output from both sides we can say that, for a 4 m long calorimeter at

the center, $\langle T_w \rangle$ is $T_w^A/\sqrt{2}$, where T_w^A is the value obtained with A side only. The value of $\langle T_w \rangle$ for the different beam conditions are summarized in the table 4.2.

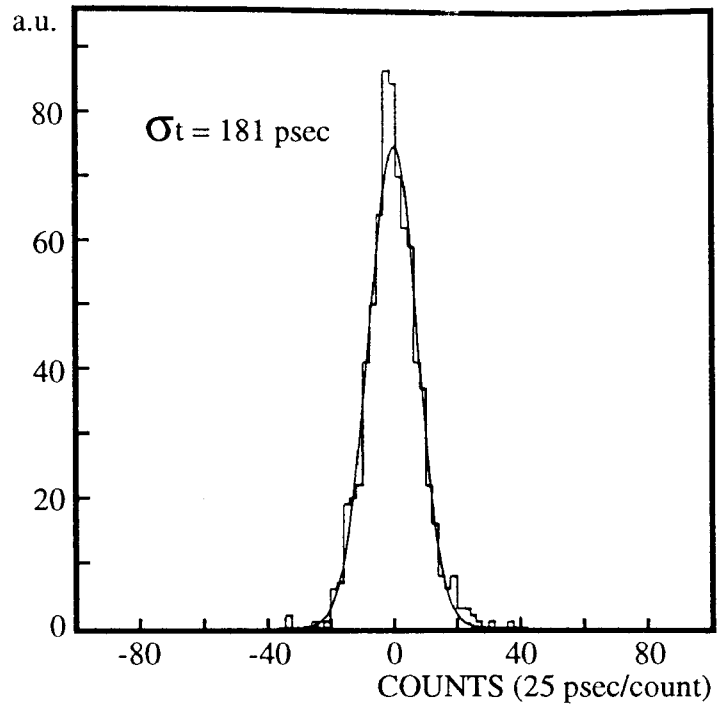

Fig. 4.30. Muon time distributions averaged over all the elements (side B).

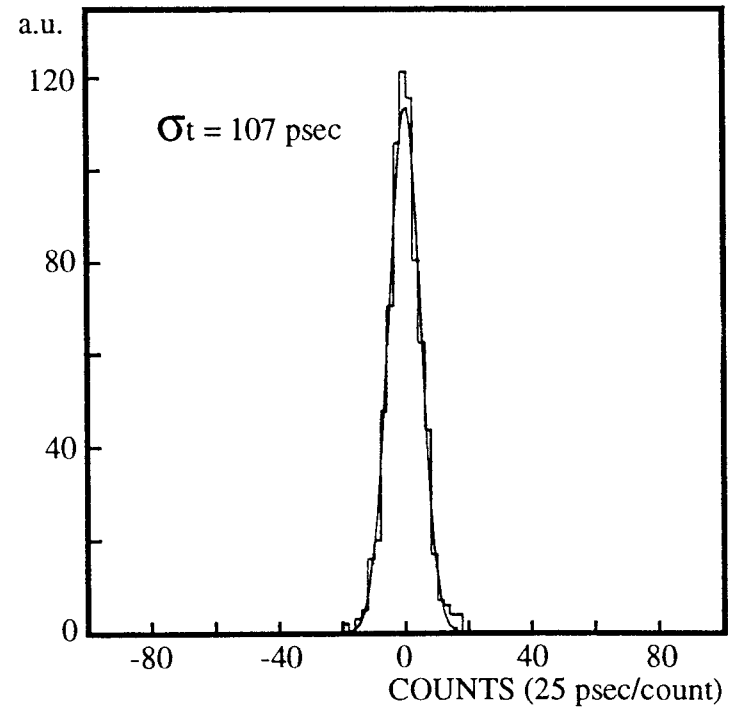

Fig. 4.31. Muons time distributions averaged over all the elements (both sides).

The same values are then plotted as σ_t vs E_{eq}^{em} in fig. 4.32. The final time resolution obtained is $\sigma \sim 50$ ps$/\sqrt{E_{eq}^{em}\ (\mathrm{GeV})}$, which meets the design requirements. Fig. 4.33 shows the distribution of T_w, for 200 MeV e's with an incidence angle of 45°. The resolution is 143 ps. This

is ~15% worse than the result found for 200 MeV e's at normal incidence. We have verified that this worsening is due to the slewing corrections, which are not well described by the $1/\sqrt{\text{signal}}$ law we used, for small signals. With appropriate corrections, the resolution is the same as for normal incidence.

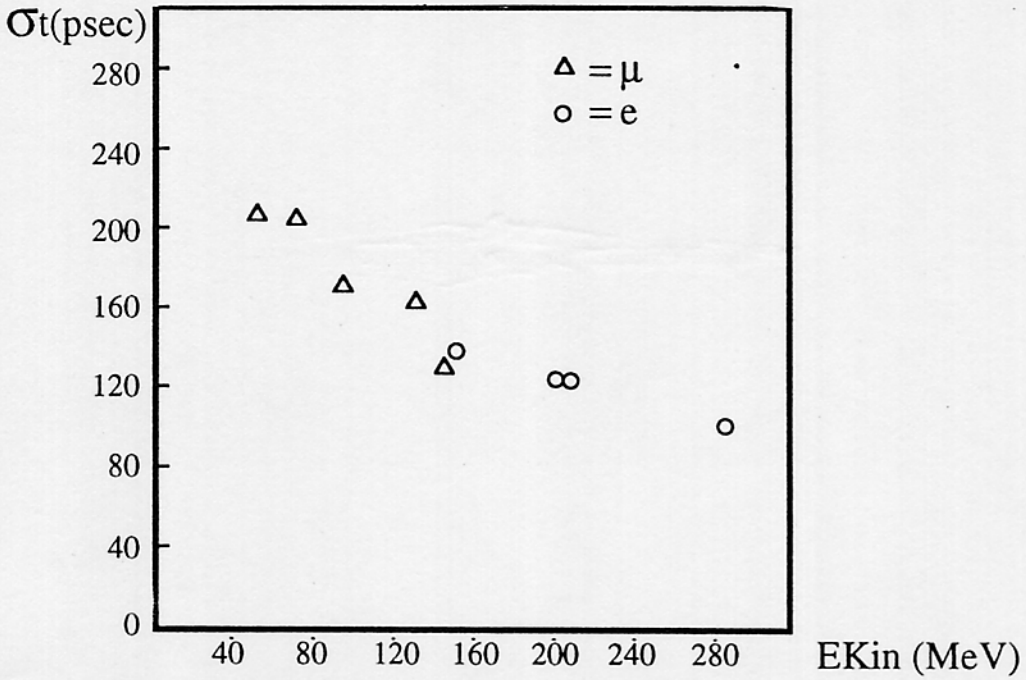

Fig. 4.32. $1/\sqrt{2}$ ×time resolution as a function of E_{eq}^{em}, side A, μ and e.

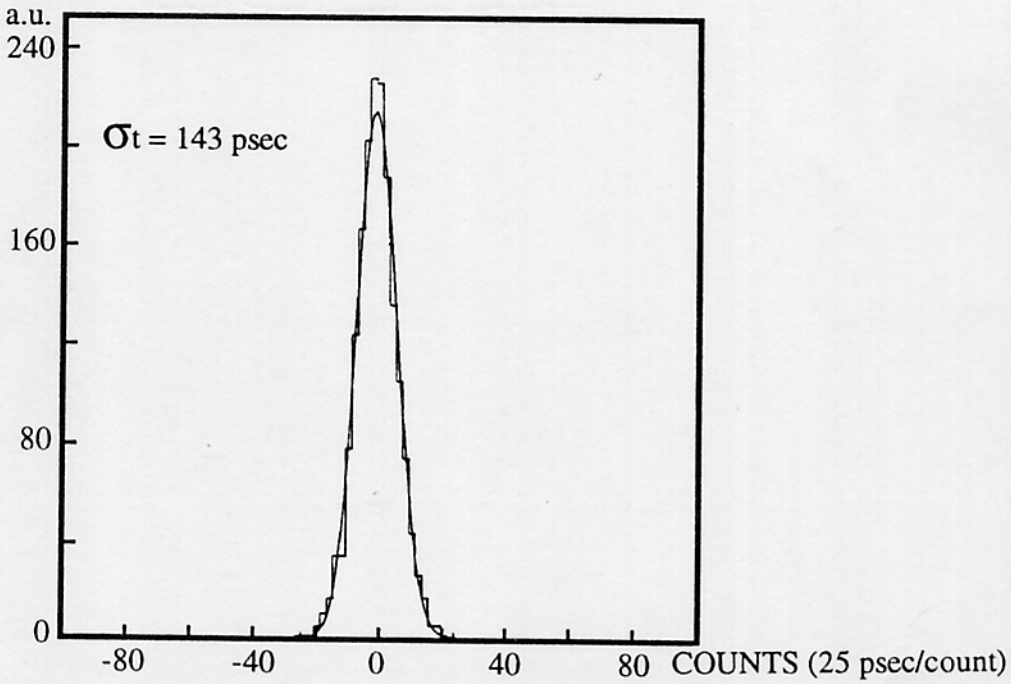

Fig. 4.33. Time resolution for electrons at 45°.

4.7.6 Test beam results with low energy γ's

Tests at PSI were limited by the electron energy being above 250 MeV. Two small, 10×10×22 cm^3, prototypes have been tested at the Ladon tagged photon[31] beam at Frascati in the region between 20 MeV and 80 MeV.[32]

Data were taken with fibers perpendicular to the beam, normal incidence, and with fibers parallel to the beam, parallel incidence. Typical distributions of the measured signals are shown in fig. 4.34 and fig. 4.35. with fits.

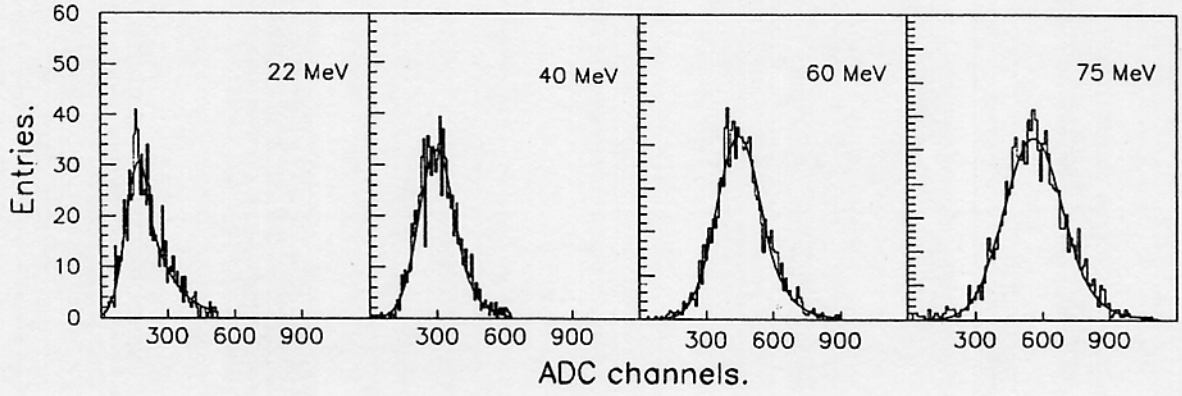

Fig. 4.34. Experimental distributions for parallel incidence.

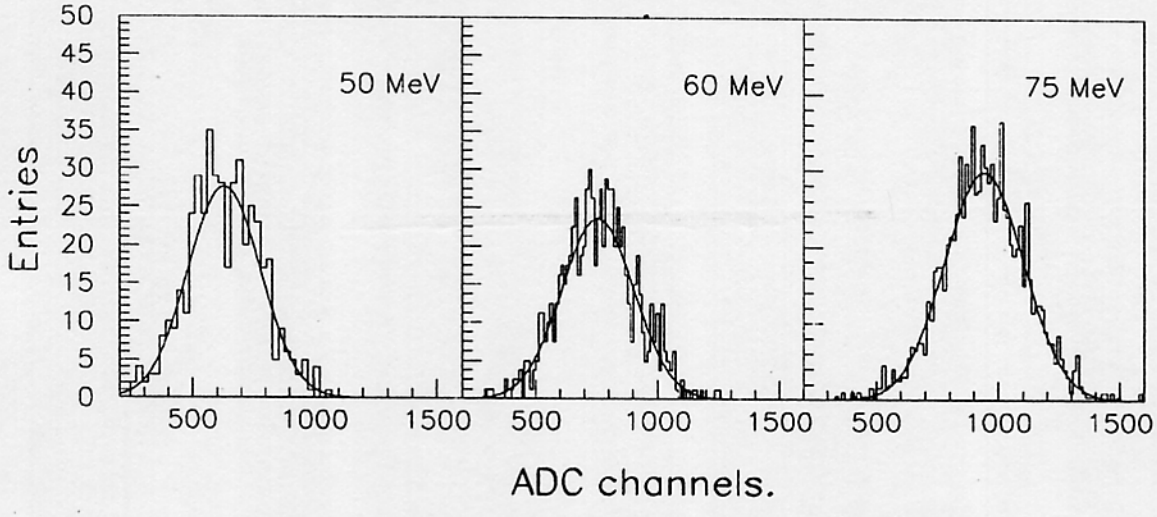

Fig. 4.35. Experimental distributions for normal incidence.

Normal incidence data are well fitted by a gaussian while the parallel incidence data exhibits a tail at high signal. Experimental resolutions obtained from the tests for both incidences are given in fig. 4.36. The normal incidence data scale with $1/\sqrt{E}$ while the parallel incidence data clearly exhibit a non scaling term. From fits to the data we obtain $\sigma/\sqrt{E\,(\mathrm{GeV})} = (4.80\pm0.06)\%$ for normal incidence and $\sigma/\sqrt{E\,(\mathrm{GeV})} = (4.7\pm0.1)\%+(3.4\pm0.6)\times\sqrt{E\,(\mathrm{GeV})}\%$ for parallel incidence, in excellent agreement with Monte Carlo simulations.[33]

The resolution at normal incidence of $4.7\%/\sqrt{(E\,(\mathrm{GeV})}$ was obtained with a light collection efficiency about 1/4 of that of the KLOE calorimeter. The results above scales to $4.4\%/\sqrt{E\,(\mathrm{GeV})}$ for the KLOE design, in excellent agreement with the results from the PSI test.

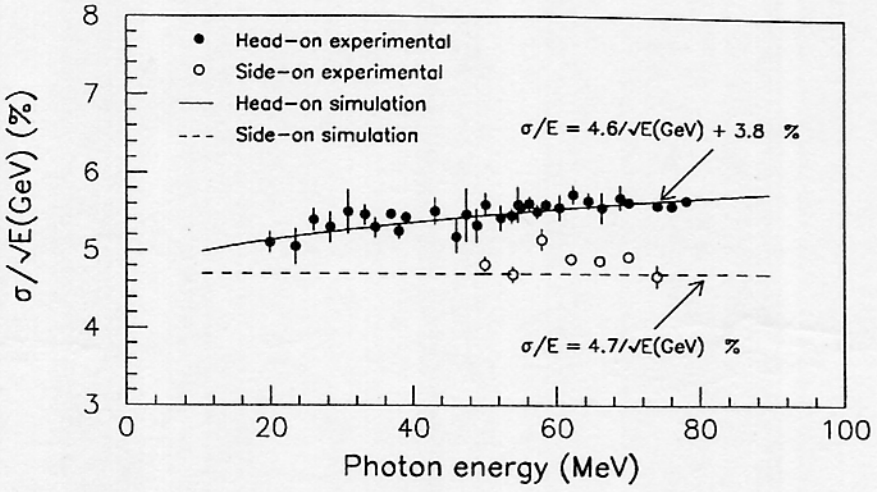

Fig. 4.36. Measured and computed resolutions.

4.7.7 Particle Identification

$\pi - \mu$ separation at 250 MeV/c is of interest in improving $K_{\mu 3}$ rejection.[34,35] We have studied methods of particle identification in the KLOE EmC using data from the test beam. The number of events collected versus the beam energy is given in Table 3.

TABLE 4.3. Number of particles used in this analysis vs beam energy.

Energy(MeV)	e	μ	π	Total
150	1780	3049	1585	6414
200	637	681	2701	4019
250	1035	1687	259	2981

In order to measure the energy released layer by layer inside the calorimeter and to find the particle range, an algorithm for path reconstruction has been developed. Starting from the second cell in the first layer, a vectorial sum of the energies released in adjacent cells has been performed to find the particle direction. The energy released in this layer is measured and the next cell with higher energy is found. The same procedure is repeated in the successive layers (see fig. 4.37). This method performs a particle path reconstruction independently from the incident angle. At the end of this procedure the entire path inside the calorimeter has been reconstructed, measuring the range, the energy released layer by layer and the differences between each other, essentially a specific ionization measurement.

Performing cuts on path length and energy difference between fifth and fourth layer, the muon rejection of different momenta can be tuned while retaining good pion efficiency. At 250 MeV using a cut on path length of 19 cm and a cut on the energy deposit difference gives a muon rejection factor of 7 with an efficiency for pions of 95%.

A more powerful method, using discriminant analysis[36] has also been tried. This method makes optimal use of all variables carrying information about whether objects belong to different

classes.[37]

Each event inside the calorimeter is described by a certain number of variables like the cluster length, the total energy, the plane energies and so on. The discriminant analysis, starting from a sample of these events, is able to increase the separation between clusters, building new discriminant variables as a linear combination of the original ones. Fig. 4.38 shows the distribution of a discriminant for pion and muons of 250 MeV/c. Results of a first analysis are shown in table 4.

TABLE 4.4. Particle id. with Discriminant Analysis.

Truth	e id.(%)	μ id.(%)	π id.(%)
e (250 MeV/c)	95.2	2.0	2.8
μ "	2.0	92.0	5.9
π "	3.9	12.4	83.6
Rej. Fact.	21	7	-
e (200 Mev/c)	93.0	2.8	4.2
μ "	0.4	85.6	14.0
π	0.6	2.8	96.6
Rej. Fact.	161	34	-

In conclusion, results obtained with a primitive path reconstruction give a μ rejection factor of $\sim$7, with a pion efficiency greater than 95%. While discriminant analysis is potentially more powerful, the present work still requires refinement. Both analysis show that most informations are provided by the fourth and fifth layer, justifying the present choice of the EmC granularity.

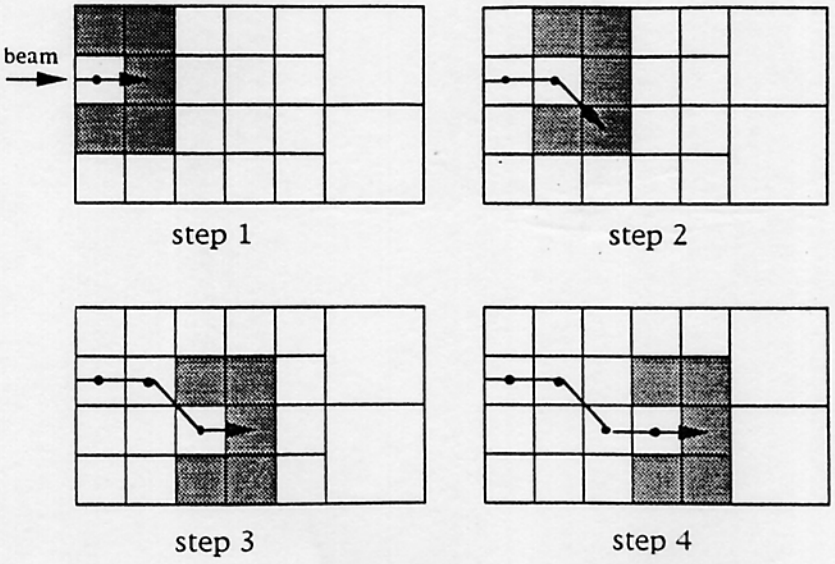

Fig. 4.37. Particle path reconstruction inside the calorimeter.

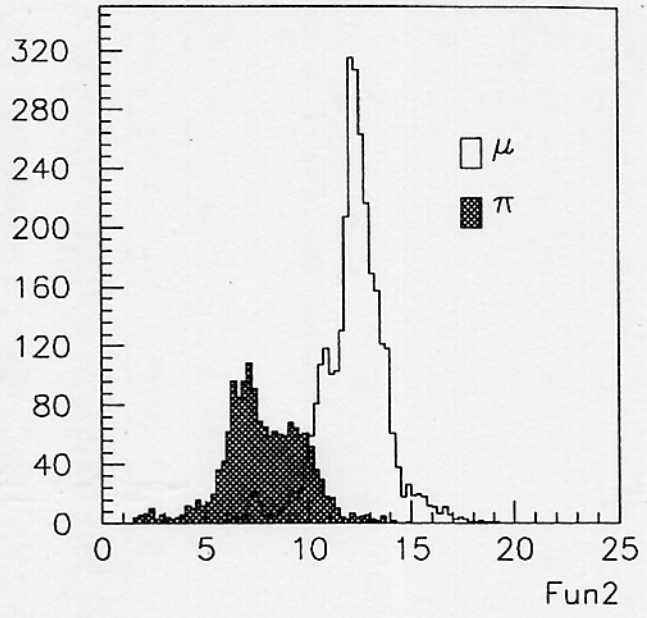

Fig. 4.38. Distribution of a discriminant variable for π's and μ's.

4.7.8 Particle ID with TOF

The excellent calorimeter timing performance provides additional $\pi - \mu$ rejection, in conjunction with the tracking information. A simple algorithm has been applied to simulated $K_{\mu 3}$ decays, which survive the kinematical cuts described in section 10.3.1. A χ^2 function

$$\chi^2 = \frac{(\Delta T_s - \Delta T_p)^2}{\sigma^2}$$

is built, where ΔT_s is the observed difference in particle arrival times and ΔT_p is the expected time difference in the hypothesis that both particles are pions. Fig. 4.39 shows the rejection factor obtained as a function of the calorimeter timing resolution, for two different signal efficiencies. In the relevant momentum range, where one expects a resolution of ~120 ps, a rejection factor of 8 is obtained, while keeping 95% of the signal.

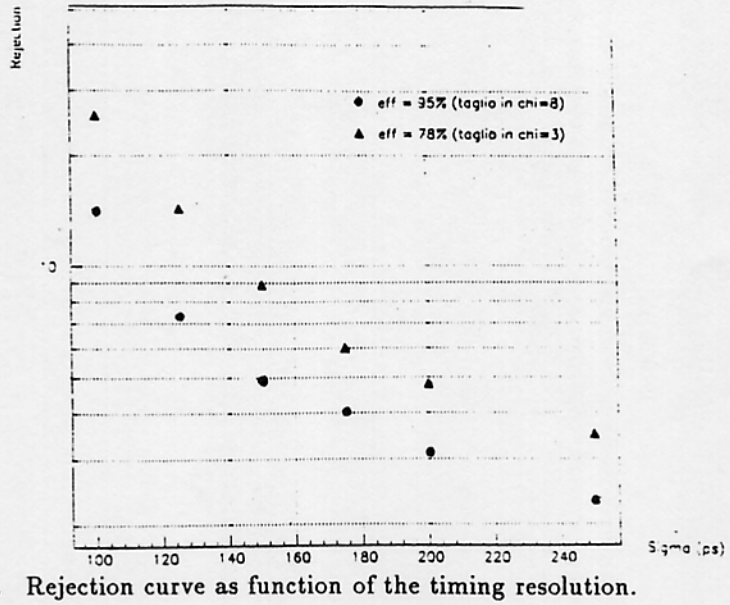

Fig. 4.39. Rejection curve as function of the timing resolution.

4.7.9 Test beam performance of ARCO.

The ARCO prototype was tested, along with the barrel prototype, at PSI test beam, with

the main aim of demonstrating that with the curved structure of ARCO calorimeter performance and fiber light transmission characteristics are not altered with respect to a straight geometry of barrel prototype. The test beam setup at PSI has been described in section 4.7.2. The four rows of ARCO were lined up with barrel rows. However due to mounting supports there was an ~10 cm air gap between the two calorimeters. 16 rear barrel readout channels were used to read the ARCO cells, so that the readout electronics remained exactly the same as described in section 4.7.2 for the barrel. All data were taken at normal incidence.

4.7.10 ARCO Calibration

Inter-cell calibration was performed using 300 MeV/c pions, positioning the beam at the geometrical center of the four row and collecting ~10000 events for each row. In order to isolate response for normally incident pions which act like minimum ionizing particles the following set of analysis cuts was used:

1. A cut was applied on the scatter plot of the pulse height of the trigger counters A and B, to clean up the beam from stray or non minimum ionizing particles.
2. Pions were identified based on their time of flight information as mentioned in 4.7.2.
3. To ensure normal incidence of the beam, inter-row isolation cuts were used, i.e, while studying i^{th} row, it was required that the surrounding elements of that plane had no energy deposit.
4. 300 MeV/c pions deposit the same amount of energy in each of the two longitudinal row. We therefore selected events in the window as shown in fig. 4.40, a plot of the correlation between the signals of the two rows.

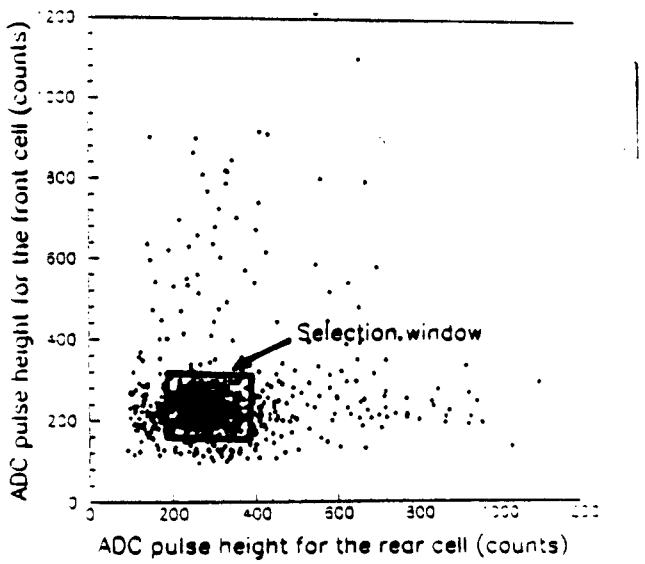

Fig. 4.40. Correlation of the pulse heights on front and back rows.

The pulse height distributions obtained are symmetric and their averages were used as calibration constants. An immediate check of the calibration procedure is performed by comparing the sum of normalized pulse heights of all eight cell on one side with that of the other side as shown in fig. 4.41. The line is the expected correlation.

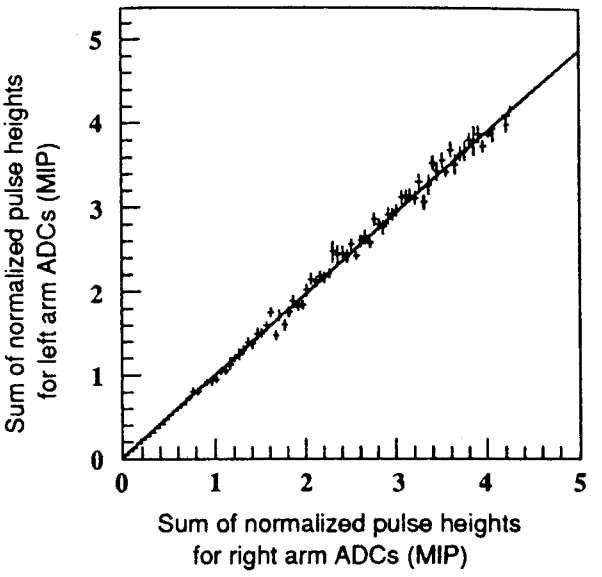

Fig. 4.41. Correlation of the normalized pulse heights on side A and B.

4.7.11 Attenuation length

Each row of ARCO was scanned all along its length, in order to obtain the response vs distance. The normalized pulse height for a readout cell is plotted as function of beam distance from the PM in fig. 4.42a for SCSF-38 fibers and in fig. 4.42b for SCSF-81 fibers. Typical multi-exponential behavior is shown by both types of fibers, and fitting the curves with an exponential function for x $\geq$ 50 cm yields an attenuation length of 1.98 m for SCSF-38 and 2.00 m for SCSF-81.

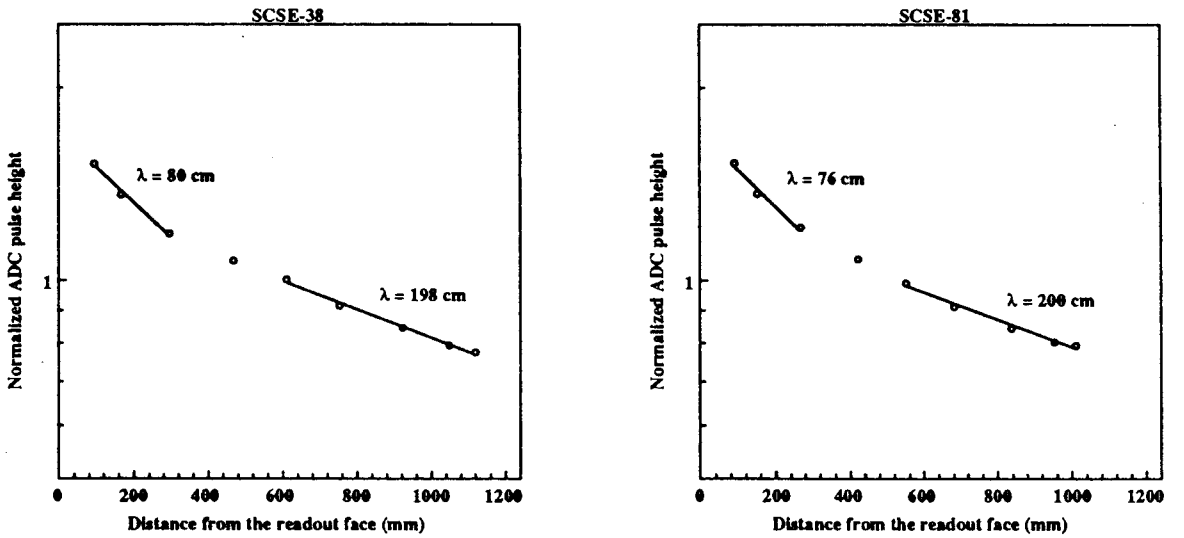

Fig. 4.42. Attenuation curves for fibers SCSF38 a) and SCSF81 b).

The main purpose of this measurement was to check whether curving fiber deteriorates light transmission. Fig. 4.43, where ARCO and Barrel attenuation curves are plotted, shows no significant difference.

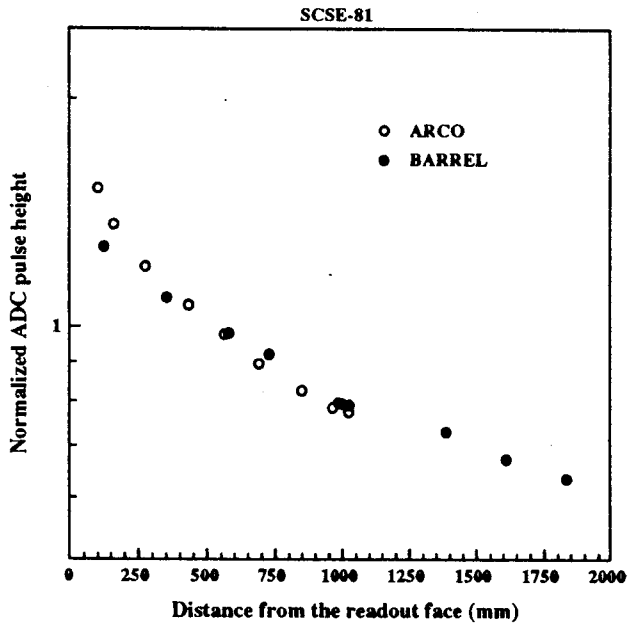

Fig. 4.43. Attenuation curves for ARCO and straight prototype.

4.7.12 Energy resolution for ARCO

Data obtained for electrons with beam momentum of 150 and 200 MeV/c were selected as above. Since the total depth of ARCO is not sufficient to contain the showers, the signals the straight prototype behind were added. The relative weighing of ARCO and straight prototype signals is done by a constant which minimizes the spread of energy distribution. The pulse height distributions for 150 MeV/c and 200 MeV/c electrons are shown in figure fig. 4.44. An energy resolution of $4.7\%/\sqrt{E\ (\mathrm{GeV})}$ is obtained, in agreement with the straight prototype results.

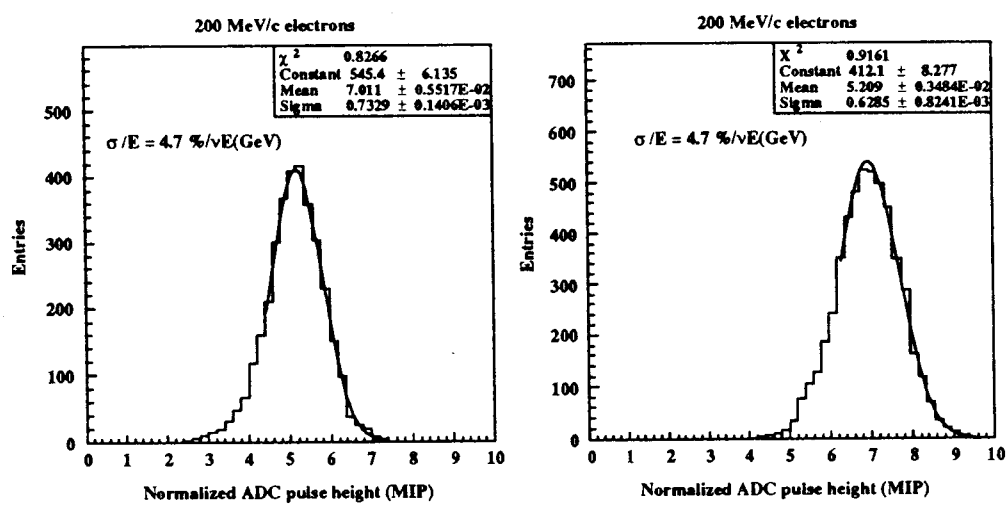

Fig. 4.44. Energy response to 150 and 200 MeV/c electrons.

4.7.13 Time resolution for ARCO

For timing analysis we have used 150 MeV/c electrons incident at the center of second innermost row. Time walk corrections are made for all channels of ARCO and T_0s, obtained from the corrected TDC distributions, are removed. Fig. 4.45 shows the energy weighed time distribution, which has an rms of 150 ps. After subtracting quadratically the time base contribution of 85 ps, one obtains a time resolution of 120 ps, which also agrees with the straight prototype

results.

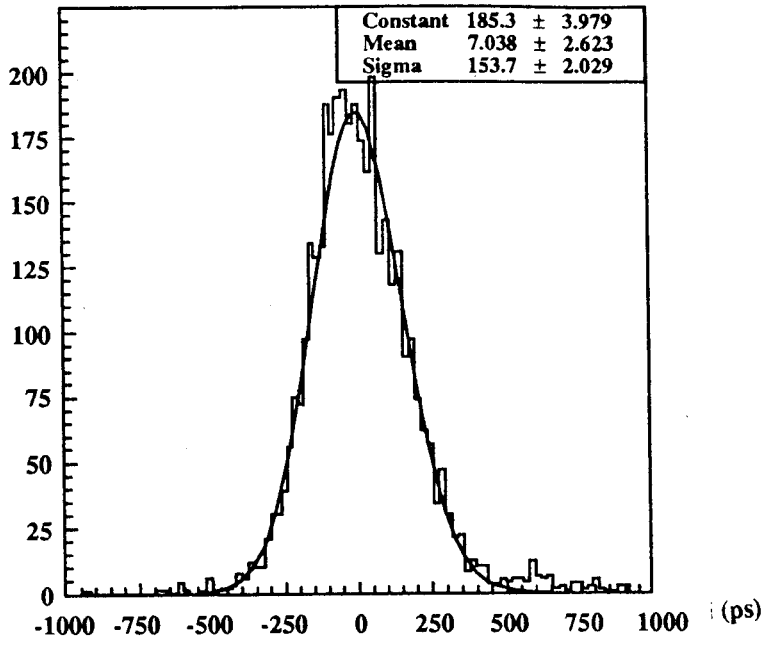

Fig. 4.45. Time resolution for 150 MeV/c electrons.

4.7.14 Cosmic Ray Results with Claw

The claw prototype[38] has been exposed to cosmic rays during a two-week period. Four Hamamatsu R1398 photomultipliers (HV=-1600V) were glued to 3.5×3.5 cm^2 lightguides, 20cm long. Two lightguides were glued to each claw end. A two-counter telescope defined a 7×1 cm^2 cosmic ray spot located at 50 cm from the straight readout end and at 50 cm from the 5 cm-radius curved readout end. A 10 cm lead brick was placed between the two counters. The gate to the ADC was formed by coincidence of the telescope counters. The ADC scale was calibrated in photoelectrons by illuminating the photocathodes with green LED's.

Fig. 4.46 shows the correlation between the photomultiplier signal connected to the straight end P_S and the signal of the 5 cm radius, curved end P_C, in photoelectron units. The cosmic ray impact point is at 50 cm from both readouts. Isolation cuts are applied, requiring an energy deposition in the adjacent counter not exceeding 20 p.e. The most probable value of the charge distribution as seen by P_C is approximately 90 p.e. Fig. 4.47 shows the two signals P_S and P_C averaged together.

These preliminary results show that curved modules can be constructed with no appreciable loss of light transport efficiency even with such a small curvature radius, which is significantly smaller than the smallest radius in the KLOE end-cap design.

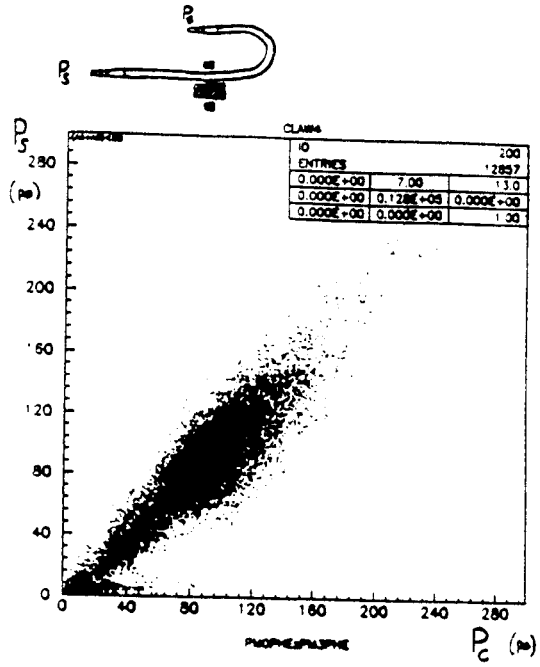

Fig. 4.46. Correlation between P_S and P_C signals.

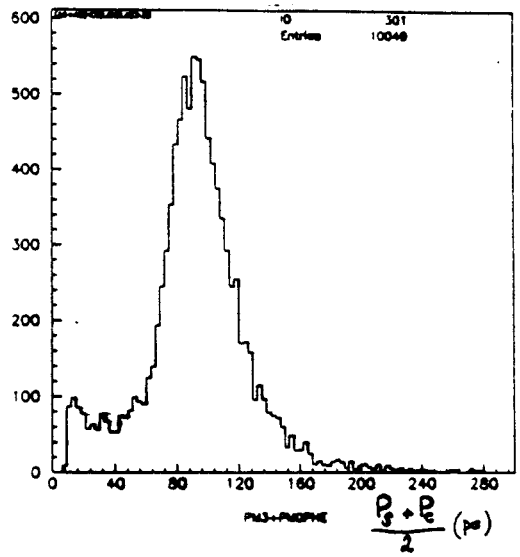

Fig. 4.47. Straight-end and curved-end signals averaged together.

4.8 Calibration and Monitoring

4.8.1 Physics Requirements

The overall error in the determination of efficiency, trigger and reconstruction acceptance of π^0's in the final state, must be kept at a level of few parts in 10^4. The large number of events available at DAΦNE will be used to calibrate and monitor the calorimeter. "Calibration events" will be collected *simultaneously* with physics events, ensuring freedom from biases introduced by different running conditions. In the following, the main variables to be calibrated and monitored are summarized, together with a brief discussion of the systematic errors arising from uncontrolled variations in the determination of these quantities.

1. Energy: the measurement of the energy of γ's from π^0 decays enters in the constrained fit for the determination of the $K_L \to \pi^0\pi^0$ decay vertex.
2. Time: it is used mainly for the reconstruction of the neutral decay vertex of K_L and K_S

decays and is helpful for $\pi - \mu$ separation. The times from the two photomultipliers also provide the coordinate along the readout element which is used in the constrained fit. The time resolution represents the largest contribution to the accuracy in the determination of the fiducial volume for the reconstruction of the $K_L \to \pi^0\pi^0$decay vertex.

3. Efficiency; a precise and direct (*i.e.* from data) evaluation of the photon detection efficiency is crucial for the measurement of the π^0 reconstruction efficiency and of the background (*e.g.* from the $K_L \to \pi^0\pi^0\pi^0$ decay channel).
4. Trigger: a set of triggers with a large overlap has to be envisaged, in order to provide low threshold trigger configurations whose redundancy can be used for monitoring purposes.

4.8.2 Monitoring the Energy Scale

From test beam data it has been shown that the calorimeter has an energy resolution of $0.045/\sqrt{E\ (\mathrm{GeV})}$, which means that, on average, a resolution of $\sim$13% is expected for a γ coming from $K^0 \to \pi^0\pi^0$. It can be shown that the constrained fit used to determine the $K_{L,S}$ decay vertex is weakly dependent on the energy resolution and scale (in fact the fit improves the energy determination of the γ's). This fact allows a relatively loose requirement on the calibration and monitoring. The determination of the calibration constants and the periodic monitoring of the photomultiplier's gain and of the analog readout electronics, can be easily performed with Bhabha events and cross checked with muon pairs and cosmic rays. An accuracy of a fraction of a per cent can be easily achieved with few minutes of data taking. In the barrel region, at $\mathcal{L}$=2.5×10^{32} a rate as high as 3 Hz per readout element is expected. In the end-caps the monitoring time window could be even shorter due to the large increase in rate. In addition we will monitor the calorimeter electronics with a test pulse, see section 6.1.

A proof that the calibration obtained with electrons directly applies to photons is obtained by computing the invariant mass of 2 and 4 photons and comparing with the π^0 and K^0 masses.

4.8.3 Monitoring the Time Scale

The time scale must be kept under the tightest control. As already explained, a crucial role played by the calorimeter lies in the determination of the K_L neutral decay vertex. Moreover, the coordinate along the fiber direction is deduced from the difference in arrival times at the ends of the corresponding readout element of the calorimeter. The knowledge of the time scale is crucial for the determination of the fiducial volume, see section 1.3.2, requiring control at the level of few parts in 10^4. The required accuracy of 0.5 mm in the fiducial volume definition, translates into an averaged time accuracy of about 10 ps.

Such a precision in the calibration of times can be achieved accumulating a suitable number of events (Bhabha) in each readout element. We will show that the period of the variations of the calibration constants are long with respect to the time interval over which they are determined.

Considering a readout element of length L, the two arrival times of a particle incident at a point x can be written:

$$\begin{aligned} t_1 &= T_p + t_1^0 + T_{L-x} \\ t_2 &= T_p + t_2^0 + T_x \end{aligned} \tag{4.1}$$

where T_p is the time of flight of the particles impinging on the calorimeter, t_1^0, t_2^0 the delays, for each channel, from the PM to the TDC and $T_x = x/v$, $T_{L-x} = (L-x)/v$ the transit times

along the scintillation fiber, v the speed of the light in the fiber. We can therefore construct the two variables:

$$\begin{aligned} t_1 - t_2 &= t_1^0 - t_2^0 + (L - 2x)/v \\ t_1 + t_2 &= 2T_p + t_1^0 + t_2^0 + L/v \end{aligned} \tag{4.2}$$

The first variable allows us to determine the coordinate along each readout element. In Bhabha events we can consider the term $t_1^0 + t_2^0 + L/v$ as a constant which has to be kept under control as already explained, at the level of 10 ps. The term $2T_p$ will be given, in Bhabha events, by the evaluation of the trajectory provided by the Central Chamber with a spatial resolution which gives an extremely precise expected time of flight.

In order to determine the longitudinal coordinate, z, the values of t_1^0, t_2^0, L and v must be known. The accuracy required is much lower with respect to the preceding case.

4.8.4 Monitoring the Detection Efficiency

The problem of monitoring the photon detection efficiency, and, in general, the response of the calorimeter to the various particles hitting it, can be divided into two separate tasks.

1. A detailed survey of the status of each readout element and a mapping of cracks, inefficiencies, noisy channels, etc, which can be performed nearly on-line. Bhabha events, cosmic rays, muon pairs etc., will help monitoring the calorimeter efficiency for photon detection, which are expected to be high.

2. A precise determination of the photon detection efficiency, see section 10.2, for which we can use K_L and $K^{\pm}$ decays with both neutral and charged pions.

4.8.5 Results on Monitoring from Tests

An evaluation of the procedure for the monitoring of the time scale is given by the prototype data collected at PSI. A relatively long (~20,000 triggers, ~2 hours elapsed) run was subdivided in groups of ~1,000 selected 250 MeV electrons. A cut on the energy seen by the first readout element hit by the beam was applied in order to reduce tail effects in the determination of the arrival times.

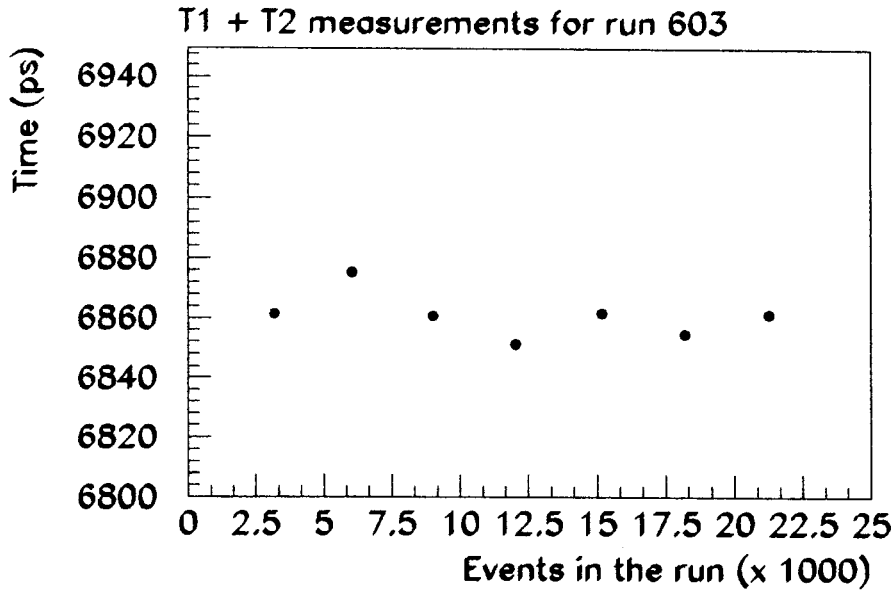

Fig. 4.48. Measurements of $t_1 + t_2$.

The quantity $t_1 + t_2$ was determined in the 7 parts in which the run was divided (fig. 4.48). The r.m.s. of the seven measurements turns out to be 7 ps. An analogous procedure was applied to a set of contiguous runs, obtaining a similar spread in the determinations of $t_1 + t_2$. The results are in agreement with the expected small differences in the time scale at short term periods. They also shows that, provided significant statistics are collected, using only on-line data we are capable of detecting drifts in the timing system.

5. TRACKING CHAMBERS

5.1 Introduction

The drift chamber design is driven by two points: a) maximizing the homogeneity and isotropy of the tracking volume because of the long decay path of the K_L and the large opening angle of the charged decay products and b) achieving a high density of track point sampling in order to obtain high efficiency for the reconstruction of $K \to \pi^+\pi^-$ decays. Single sense wire cells, of constant size across the chamber volume are the only acceptable solution. They imply however a more complicated space-time relation and require a larger numbers of electronics channels. The disadvantage of having several field wires per sense wire is compensated by the fact that smaller diameter wires can be used, reducing the amount of material and lessening the mechanical tension on the end walls of the chamber. Electrically, single wire cells require a single high voltage for the sense wires. Grounding of all field wires simplifies the feedthrough's, improves signal transmission and gives better control of noise. An overall view of the chamber with dimensions is shown in fig. 5.1.

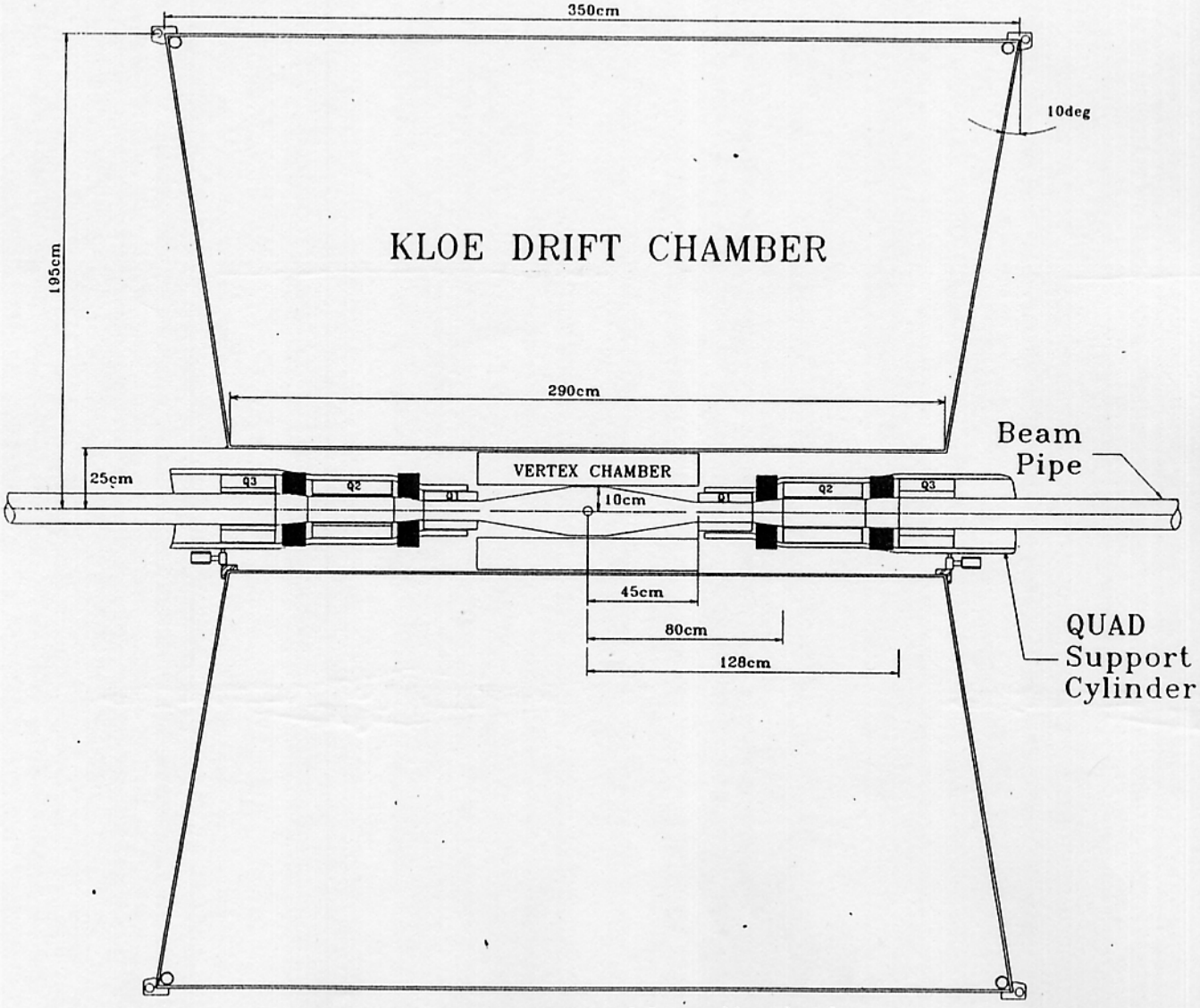

Fig. 5.1. An overall view of the tracking chamber.

5.2 Cell

The choice of cell dimensions is governed mostly by two factors. Frequent sampling of the tracks improves tracking and vertexing efficiency but makes the construction of the chamber harder, more expensive and affect the overall reliability of the device. One cannot forget the possibility of accidents at construction time and catastrophic failures, such as many wires breaking during attempts to remove a broken one, which increase combinatorially with the number of wires. Finally the cost and complexity of the wire read–out electronics cannot be ignored. The present choice is based on the results of extensive Monte Carlo calculations[39] whose results are given in chapter 10. A cell with a cross section of about 4 cm^2 appears acceptable and we choose therefore a cell width of $2\pi/3$ cm and a height of 2 cm. This corresponds to ~27000 sense wires, a rather large number.

Square cells are chosen because they allow uniform and isotropic filling of the r, ϕ plane and non axial stringing of all wires, with minimal deformations of the cell geometry along the axis.

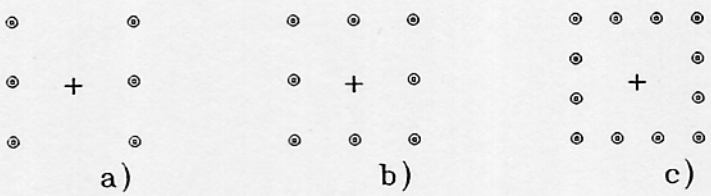

Fig. 5.2. Square cells: a) MARKII, b) CLEO-II, c) ARGUS.

As illustrated in the examples of fig. 5.2, several square cells have been successfully used, differing in the ratio of field wires to sense wires, $\mathcal{R}_{fs}$. In principle, the number of field wires affects the opacity of the chamber (*i.e.* the multiple scattering contribution to the momentum resolution) and the stiffness of the end-plates. Both these effects are proportional to the square of the field wire radius r_{fw}. The fields at the surfaces of the wires which determine gain and long term stability are, instead, inversely proportional to the wire radii. Cells with higher $\mathcal{R}_{fs}$ are best as far as multiple scattering and mechanical tension on the end-plates are concerned. Because of the very large total number of wires we prefer to chose $\mathcal{R}_{fs}$=2 (3 at the worst). This configuration requires extensive testing.

5.3 Wires

Reasonable signals, for both time and charge measurements, are obtained in argon based gas mixtures with gains of the order of 5×10^4, corresponding to linear charge densities of approximately 13 nC/m on the sense wires. In what follows, we shall assume that similar values, with a large margin of uncertainty[40] due to the final choice of the gas mixture, hold also, in a helium based gas.[41] Within a cell, the total charge on the anode wire is equal to that on the corresponding cathode wires. Therefore, by fixing the gain or equivalently the charge density on the sense wire and imposing a maximum field on the field wires, because of ageing effects,[41] one gets a lower limit on the radii of the field wires, for any given cell configuration, *i.e.* for any given $\mathcal{R}_{fs}$. A safe limit, in a helium mixture and in the low radiation environment at DAΦNE,

is around 30 KV/cm, to be confirmed by measurements. The SLD group found 50 kV/cm to be satisfactory. Use of He might lower this value.

For the chosen cell configuration, one obtains the desired gain with 25 μm diameter sense wires (for an electric field on the wire surface of about 180 kV/cm) and fields below the limit of 30 KV/cm for 75 μm field wires.

5.4 Layer Structure

The choice of cell described allows the possibility of stringing consecutive layers at alternating opposite angles to the chamber axis, thus maximizing the homogeneity of the chamber throughout the entire gas volume. A cell layer is defined as the set of sense wires at a given radius and the field wires immediately below. The relative position of the upper row of field wires, with respect to the corresponding sense wires, will change along the axis of the chamber, the z axis, and this will affect, to some extent both the time to space relation and the uniformity of the gain along the z axis. These effects, however, are smaller than those, analogous and unavoidable, due to the fixed cell width and to the fixed pitch of the field wires in consecutive layers, expected along the azimuthal direction.

Having all layers at angles with respect to the axis of the chamber which is parallel to the B field, will complicate pattern recognition but this is compensated by the higher accuracy in the measurement of z. Track multiplicity in KLOE is low, $\sim$3 in average. Pattern recognition will not be our worst problem. The stereo angles are chosen to give a constant inward displacement, at the chamber center, in all the layers, thus maintaining the shape of the cell. Table 5.1 gives the stereo angles for a radial drop of 1 cm. The stereo angle ranges from $\sim$51 mrad to $\sim$112 mrad. The choice is a compromise between accuracy in the z coordinate and filling of the sensitive volume. Two layers of guard wires correct field distortion due to inner and outer walls of the drift chamber at 25 cm and 194 cm radius respectively.

TABLE 5.1. Chamber Structure.

layer type	radius (cm)	st. angle (mrad)	w. dia. (μm)	number of wires	voltage (Volts)
inner wall	25				0
guard	27	−50.1	50	162	900
1^{st} field	28	+50.9	75	168	0
1^{st} sense	29	+51.8	25	87	1800
2^{nd} field	30	−52.6	75	180	0
2^{nd} sense	31	−53.4	25	93	1800
..	..	..	..	..	..
82^{nd} sense	191	−112.1	25	573	1800
83^{rd} field	192	+112.2	75	1152	0
guard	193	−112.3	50	1158	900
inner wall	194				0

The stereo angle, ϵ_i, is given by:

$$\epsilon_i = \arctan(\sqrt{2r_i - 1}/L_i) \tag{5.1}$$

with r_i and L_i in cm. It increases approximately with the square root of the radius of the layer

up to a value of 112 mrad on the outermost radius. L_i indicates the length of the i-th layer.

In general, the i^{th} sub-layer of sense wires will be at a radius r_i given by: $r_i = 27 + 2i$ (cm) with s_i sense wires

$$s_i = \frac{2\pi \times r_i}{2/3\pi} = 3 \times r_i \tag{5.2}$$

The total number of sense wires is

$$\mathcal{N}_{\rm sw} = \sum_{i=1}^{82} s_i = 27060. \tag{5.3}$$

and that of field wires is 55278. The number of guard wires is 1320. Table 1 summarizes the structure of the chamber. The total number of wires is 83,658. A cell with $\mathcal{R}_{\rm fs}$=3 requires 111,215 wires.

5.5 Multiple Scattering

Both gas and wires contribute to multiple scattering which must be maintained small for good accuracy in angle and momenta measurements at the energies of interest. Gas multiple scattering is reduced by use of helium mixtures. Primary ionization and diffusion will both affect the position resolution and also therefore affect the choice of gas. Accurate measurements of drift velocity, longitudinal and transverse diffusion and primary ionization in different gas mixtures are in the process of being performed in a very precise test chamber with an ultraviolet excimer laser. Multiple scattering in the wires is considerable and we chose therefore aluminum for the field wires while for sense wires the 25 μm radius requires tungsten. Guard wires, 50 μm thick, will be made of CuBe alloy.

The relative contributions to the radiation length due to the wires is summarized in Table 5.2 for gas mixtures with different X_0.

Table 5.2 shows that in going from a gas mixture with an X_0 = 2000 m (like 95% He - 5% iso-C_4H_{10} or 80% He - 20% CH_4) to one with an X_0 = 700 m (like 78% He - 15% CO_2 - 7% iso-C_4H_{10} or 70% He - 30% DME) the relative increment in the total multiple scattering contribution is only of the order of 35%, whereas the primary ionization goes from about 8/cm to more than 20/cm. A final choice, then, must be postponed until all measurements of the gas parameters have been completed.

TABLE 5.2. Radiation-length contributions.

Gas X_0 (m)	2,000		700	
$\mathcal{R}_{\rm fs}$	2	3	2	3
Field w dia. (μm)	75	50	75	50
Field w material	Al	CuBe	Al	CuBe
Gas contribution (%)	46	29	70	53
Sense w contribution (%)	28	18	16	12
Field w contribution (%)	25	52	13	35
Total X_0 (m)	915	576	502	380

The decrease in radiation length due to the wires is only a relative figure since the frequency of actually crossing a wire is very small (typically 0.7 per meter of track length). All the above values refer to a radiation length of the tracker volume evaluated by spreading out the wire material in the chamber and are therefore pessimistic.

5.6 Mechanical Construction

5.6.1 Wires

The mechanical tension required to have a gravitational sag roughly at the same level as the expected spatial resolution is ~56 g for a tungsten wire 25 μm in diameter and 3.0 m long. Hard drawn aluminum alloys can reach an elastic limit of 34 kg/mm^2. Aluminum wires require a tension of 64 g. They are therefore used only at 40% of the yield strength. Hard drawn aluminum alloys have been used for wires in large drift chambers, the CLEO chamber and the SLD chamber. The total wire tension for KLOE is ~4.6 tons corresponding to a load of the end-plate of ~1/25 of an atmosphere. Magnesium wires, which could increase the radiation length due to the field wires by ~×2, deserve attention. The so called *creep* of aluminum is not serious: the tension drop is negligible (<7%) at the value we plan to use and the equilibrium tension is reached within minutes. Gold plating of both field and sense wires improves long term stability. The amount of material resulting from gold plating marginally decreases the total radiation length in the chamber: a 0.3 μm. thick gold plating would, at most, add ~5% to the total chamber radiation length.

5.6.2 Chamber Walls

The structure of the walls must satisfy the constraints of very low thickness, measured in radiation lengths, of the end-plates and the outer wall. The inner wall, in addition, must produce very low energy loss for charged particles, especially kaons. The load on the end-plates is moderate and some bending of the end-plates, ≤5 mm is quite acceptable.[42] This does, however, require prestressing the end-plates before the stringing operation. We plan to build the end-plates out of solid aluminum 5 mm thick, in the shape of a truncated cone of 75° half angle, corresponding to a thickness of ~0.1 X_0, including electronics and cabling. The outer rim, where most of the deformation is expected, must be rigidly fixed to the outer wall by means of a high stiffness ring. To avoid radial deformation at the inner rim some, less relevant, reinforcement also must be provided.[43,44]

A hollow 5×5 cm^2 aluminum ring adds ≤ 0.4 X_0 in a small fraction, ~0.5%, of the total solid angle for photons coming from K decays and is stiff enough to have ≤ 0.5 mm displacement at the outer ring, as obtained by scaling from the designs mentioned above.

The expected longitudinal deformations are shown in fig. 5.3, as a function of the radial coordinate.

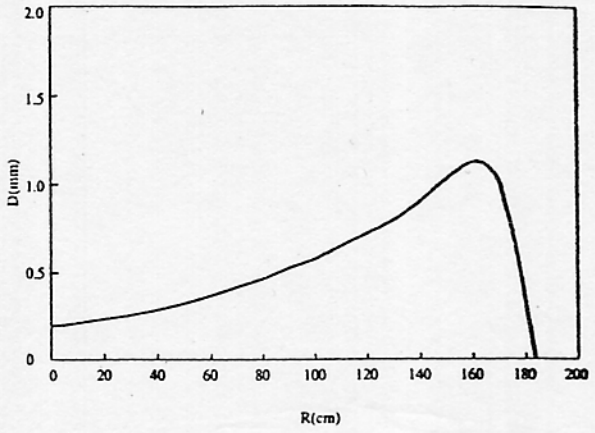

Fig. 5.3. Longitudinal deformation of the end-plates as a function of the radial coordinate.

The end-plate behaves as a membrane, with deformation increasing quadratically with radius and a sharp drop at the outer, fixed edge. A smoother behavior is expected if the thickness increases smoothly near the outer edge or if the end-plates are dome shaped.[45] These mechanical structures are under investigation. Also the use of a composite structure and carbon fiber composite materials[46] for the end-plates is under study.[47] To achieve the same deformations with flat end-plates one would need[42,47] a thickness $t \simeq [3wR^4(1-\nu^2)/(16ED)]^{1/3} \simeq 4$ cm (where E and ν are the Young and Poisson moduli); for conical end-plates[47] the thickness needed behaves as $\sim 1/\sin^2(2\alpha)$, where α, is the cone half opening. The outer and the inner walls are much easier. A composite structure, thick to avoid any buckling, but equivalent to 2 mm of aluminum in terms of radiation lengths, is adequate for the outer wall. A panel structure will simplify inspection of the inside of the chamber. For the inner wall, 1 mm of carbon fiber should fulfill any requirement.[46]

5.7 Chamber Stringing

The very large number of wires in the KLOE drift chamber requires the use of automated techniques to string the chamber. Cleanliness must be guaranteed over a period of at least one year. The use of a clean room to do the stringing is mandatory, even a *moderately (class 1000)* clean room is adequate.

We plan to do the stringing with at least partial opening(s) in the inner/outer skins. In fact we believe that the flexibility of being able to reach almost freely the already strung wires inside the chamber offsets the added precautions that have to be taken to keep the chamber clean; once the stringing is completed the final clean up of the chamber would be easier. The chamber will be strung in a vertical position: this choice, required by the automated procedures, ensures a better overall cleanliness as dust and wire clippings will eventually collect on the lower end-plate. The conical shape of the end-plates will help to also move debris and dust toward the outer rim of the end-plates, with the help of a downward air flow.

The planned stringing operation includes a motorized arm to feed the wire through the upper end-plate holes. The free end of the wire carries a soft iron needle, which serves as a weight and can be caught at the lower end-plate by a magnet. A scheme like the one described has been successfully employed in the construction of the CLEO II chamber.[42] The entire set-up must be computer controlled. Once the wires are set in place, they will be threaded through

the aluminum bushing and crimped, first at the upper end and, after tensioning, at the lower one. During the stringing operation wire tension will be continuously monitored: two Helmholtz coils can provide the (low) magnetic field necessary to measure the resonant frequency of the wires. Creep of the wires can be continuously monitored. Previous experiences with aluminum wires requires one to have a stringing and operating environment with temperature excursions smaller than 2° C. Upon completion, each individual layer will be H.V. tested in air up to 2.5 KV, roughly 50% more than the operating voltage. All wire positions will be optically surveyed after stringing.

5.8 Monitoring and Gas System

The proposed helium mixtures result in a non-saturated drift velocity, dependent on pressure and the composition of the gas mixture, requiring a high quality gas system.

We would like to design a system based on experiences from the Crystal Barrel Detector, the OPAL drift chamber, the L3 Time Expansion Chamber and from the H1 gas system. The gas volume of the KLOE detector, 40 m^3, is comparable to that of the OPAL chamber. The availability of liquid He in large quantities makes a single pass gas system the best choice. The mixture uniformity inside the whole chamber volume will be checked at several gas outlets, each of them connected via a multi-port valve to the gas analyzing system described below.

The gas system is designed to provide a two or three component gas mixture. The system must provide for the possibility of introducing water at the level of 0.01 atm, partial vapor pressure. Water has been proven to be the best method for preventing polymerization and increasing chamber life. It must also reduce the concentration of gases with large electron attachment to a level of a few ppm. The circulation should enable the exchange of the whole gas volume every one or two days, implying a pumping capacity of 1–2 m^3/h. A block diagram of the gas system is shown in fig. 5.4. The principle of operation is as follows: part of the gas entering and/or leaving the chamber at various outlets will be analyzed to check its composition and possible impurities. An infrared spectrometer will detect hydrocarbons and commercial devices will measure O_2 contamination. Gas chromatography measures the purity of the hydrocarbons. A container serves as a gas reservoir for compensating pressure changes. The temperature is monitored continuously at many positions of the chamber. A real time processor switches the valves, triggers the gas chromatograph, reduces and checks the various data.

The site of the gas system will be outside the experimental area. All gas pipes will be made of sealed copper. Connections will be made either by hard soldering or compression fittings. The in- and out- lets will be controlled by in- and out- flow meters to recognize major gas leaks. It is foreseen to flush N_2 around the detector for safety reasons and to flush leaked helium out of the detector environment.

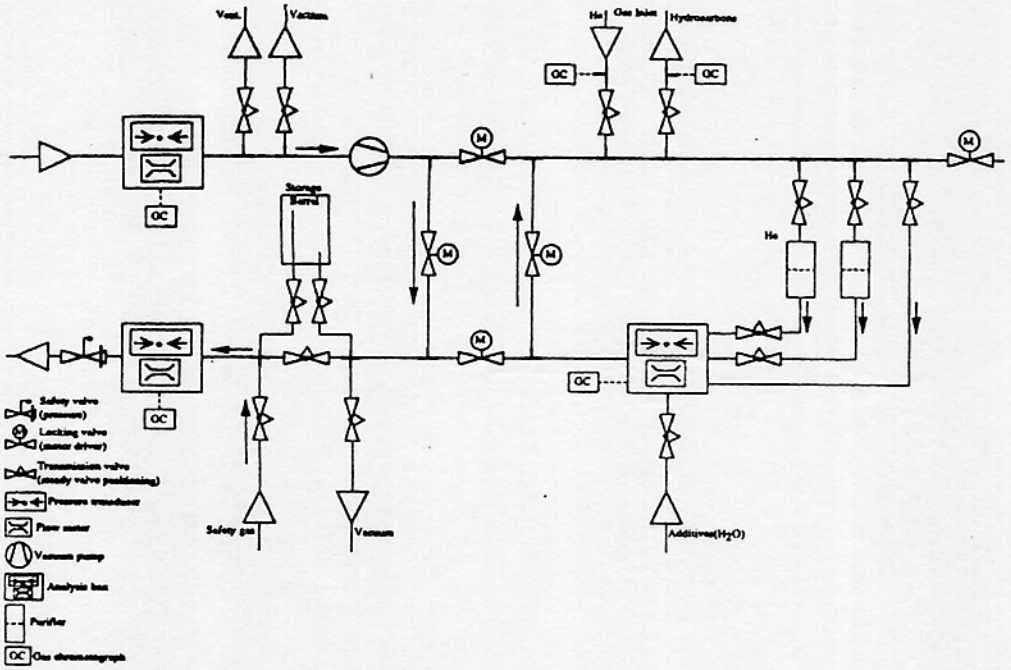

Fig. 5.4. The gas system.

Data from the gas system will be passed on with the events for continuous recording. Alarms will be provided for failures and out-of-limits conditions. Experiences with the gas systems similar to the above one show that off–line calibration and real time control including the measurement of drift velocity and gas amplification can be obtained with cosmic rays or real events. In addition we plan to have a small test chamber in which gas from the KLOE chamber is circulated allowing monitoring of the gas behavior (gas amplification, drift velocities etc.)

In addition to the information obtained from the gas system, other parameters such as temperature and pressure inside the chamber, high voltage, etc. must all be passed to the DAQ system for correlation with the events at analysis time. In order to check for possible gas stratification, we plan to have several gas inlets and outlets, at different positions throughout the end-plates, all connected, via a multiplexer, to a gas chromatograph and to an infrared spectrometer. A small test chamber, in which samples of gas of the Central Chamber flow, can directly measure the physical parameters. Changes in drift velocity, efficiency and mean pulse height would quickly and independently monitor the gas composition. In order to produce ionization in the gas, one can use different methods, like two ^{106}Ru sources[48] or alpha– decay recoils[49] or photo-electrons emitted from a cathode surface by means of a UV laser pulse.[50]

5.9 High Voltage System

Because of the unsaturated drift velocity the high voltage requires precise monitoring and control. The current drawn by the sense wires must also be monitored allowing one to trip the H.V. if excess current is measured. Adequate commercial systems are available. It is, however, unrealistic to use a power supply per wire. An intelligent and low cost distribution of high voltage to the wires is required.

5.10 Laser Calibration

A UV laser system might be used for the initial calibration of the chamber, before installation. With the help of rotating mirrors, tracks could be generated everywhere in the chamber. Seeding agents with low ionization energy could be possibly used, depending on the gas mixture selected. Using a dielectric beam splitter, in front of the scan mirror, parallel double beams of precisely known separation can be generated in order to derive drift velocity from the measured drift time difference.

5.11 Vertex Chamber

The drift chamber of KLOE surrounds the quadrupoles of the low beta insertion of DAΦNE. The needs for mounting and supporting these quadrupoles and the beam pipe imposes an inner diameter of the chamber of 50 cm. Charged tracks can therefore only be detected at distances greater than ~30 cm from the intersection point of the beams. Tracking charged particles beginning at 30 cm rather than 8–10 cm, the radius of the beam pipe, results in: a worsening of the resolution of the vertex coordinates for K decays into charged tracks near the intersection region and loss in efficiency for detecting and reconstructing $K_S \to \pi^+\pi^-$ decays.

The insertion of a small and very light vertex detector between the beam pipe and the inner wall of the drift chamber would improve both points. The anticipated gains have been estimated via MC, see section 10.1.4. Such a detector has to fulfill three requirements. First, it must be as light as possible. This is especially important for $\phi \to K^+K^-$ events. Charged kaons are produced with a velocity β=0.25 (p=127 MeV/c). Second, it has to be stable and maintenance free and, possibly, modular in such a way that a single broken wire, will not seriously degrade the performance of the whole detector. Once installed the detector will be completely inaccessible and any repair would require a very long shut down of the experiment. Moreover, modularity can make the installation of the detector easier in a region with a very limited access. Third, it must have good spatial resolution. The measurement of the direction of charged track, coming from the intersection region, will rely essentially on the vertex detector, improving the vertex reconstruction accuracy.

A detector made of very thin aluminized plastic tubes ("straw" tubes) may fulfill all the above requirements. Several experiments[52–54] have already demonstrated the feasibility and the very good performance of such a detector. It consists of many tubes (diameter from few millimeters to a couple of centimeters), mounted parallel to the beam direction or with a small stereo angle, with an anode wire running along the axis of each "straw". The detector is electrically robust, it has a simple mechanical design, it is easy to construct and finally it has a modest cost. The closed-cell structure eliminates several possible problems, present with other structures, and the modularity allows one, in case of troubles, to disconnect individual channels leaving almost unchanged the performance of the whole detector.

After an optimization study we plan to build a vertex detector made of 1350 plastic tubes, 25 μm thick and with the external diameter of 8 mm, arranged in three superlayers (fig. 5.5). The innermost and outermost superlayers are made of three tube layers and the tubes are axially assembled along concentric cylinders. The central superlayer is made of four stereo layers, two

with positive stereo angle and two with negative angle. The values of the stereo angle range from 93 to 105 mr.

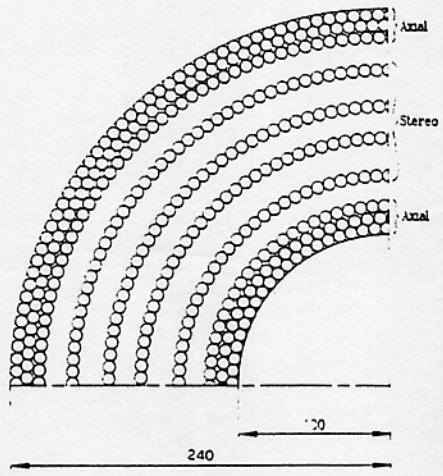

Fig. 5.5. A schematic view of the vertex chamber.

The detector will cover polar angles down to 10° with a useful length of the tubes of 1.0 m, an inner radius of 10 cm and an outer radius of 24 cm. The vertex chamber will be fixed either to the supporting structure of the low beta insertion quadrupoles or to the vacuum tube flanges just in front of the innermost quadrupoles. The mechanical structure of the detector is still under study. We are considering a few options and the final decision will be strongly related to the final design of the intersection region of DAΦNE. One possibility we are studying is to glue together the tubes of each of the two axial superlayers and to fill the interstices with a low mass mixture of glue and microballoons (similar to the AMY design) in order to have a very light self supporting rigid structure, able to support the wire tension and also the tension of the stereo tubes, which will be stretched between the two ends of the detector. Another possibility is to use light external walls made of a foam sandwich. In any case the average total amount of material, in the radial direction, of the whole detector will be kept within 0.25 g/cm^2 and the total thickness will be about 0.8% of a radiation length. The mean momentum lost by charged kaons traversing the vertex detector will be about 40 MeV/c. The tubes will be operated in proportional mode. An accuracy for the coordinate measurement in each tube better than 100 μm can easily be obtained also using a medium diffusion gas mixture (*i.e.* argon-ethane) at atmospheric pressure.

5.12 Research and Development

5.12.1 Small prototype

In order to study the true performance of a helium based drift chamber, a 4 m long cylindrical wire chamber prototype has been built at LNF.[55]

The prototype end-plates are shown in fig. 5.6. The sense wires are 50 μm Cu-Be and the field wires are 100 μm, also Cu-Be.

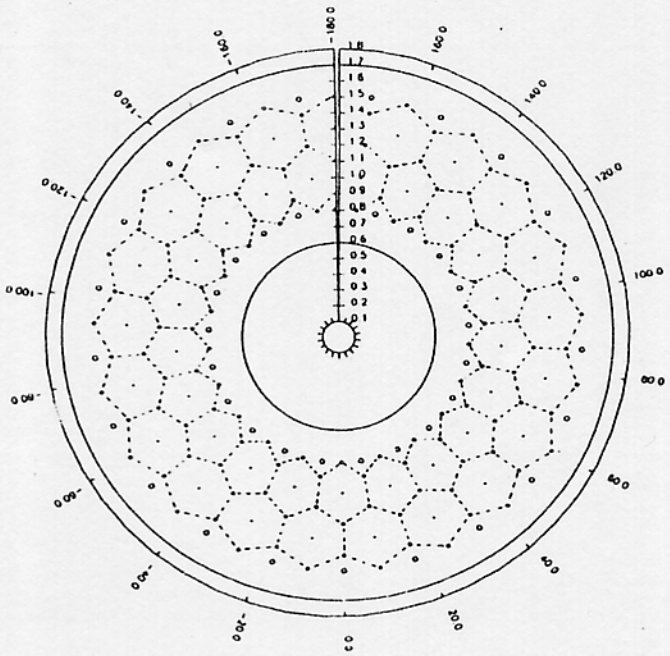

Fig. 5.6. The small prototype end-plate.

The diameter of a single cell is about 4 cm. The total number of sense (field) wires is 42 (210). The wires are fixed to the end-plates by means of special copper crimp pins (feed-through), fig. 5.7. Pin bores are 100 and 200 μm in order to fit sense and field wires respectively. Pins and wires were crimped with a special crimping tool designed at CERN. The overall rms positioning error of the wires is estimated to be less than 50 μm. The chamber is flushed at atmospheric pressure with a 95:5 helium, isobutane gas mixture.

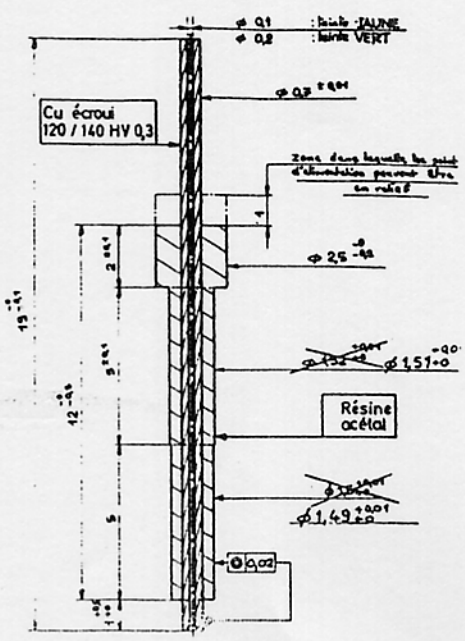

Fig. 5.7. Copper feed-through.

The wire signal amplifiers were built at LNF.[56] A typical signal obtained with 1850 V on the sense wires and field wires at ground, as seen at the output of the preamplifier, is shown in fig. 5.8.

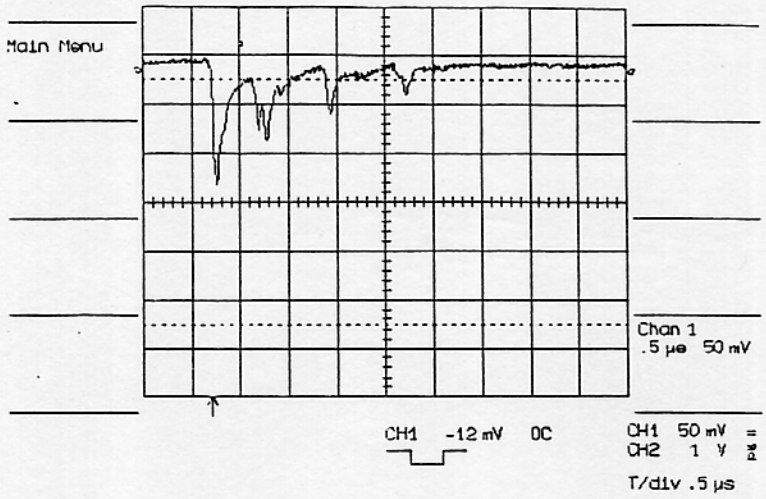

Fig. 5.8. Wire signal from the small prototype.

A telescope of streamer tubes and a glass spark chamber system provide external tracking and timing signals for the study with the prototype of gas and cell performance. The telescope provides a rms resolution on the reconstructed point inside the prototype chamber of 100 μm.

5.12.2 Prototype 1 design

We intend to build a full length prototype of approximately one sixteenth in azimuth for the purpose of checking cell structures of different dimensions, for testing the efficiency and time-to-distance relation of different ratios of field wires to sense, and for testing small scale production of preamplifier prototypes and front-end digitizing electronics. The prototype will also allow studies of the mechanical tension on the wires and of the gravitational sag, of the electrostatic stability of the cell structures for different mechanical tensions, of the systematics introduced by the tolerances on the wire positions, of the design of the feedthrough's, both for sense and field wires. The large volume of the prototype will help in understanding the monitoring of the physical parameters and the problems associated with the gas supply, also the impermeability of the walls to helium and the possible stratification of the gas mixture.

Finally, given the large number of wires (about two thousand cells will be strung), this prototype will allow testing the wiring strategy to be adopted in the actual construction of the drift chamber and for training personnel to do this difficult and skill requiring task.

5.12.3 Electronics R&D

R&D work has been in progress and is continuing toward the development of low cost, high performance flash encoders operating at 200–1000 mega–samples per second. The encoders would be followed by fast, special purpose processors to generate pulse times and area. These devices could be of use for wave–form analysis of sense wire signals.

6. FRONT END ELECTRONICS

6.1 Calorimeter Signal Processing

Given the stringent requirements in time and energy resolution of the EmC, the front end electronics, FEE, must have excellent performance, in particular with respect to noise and bandwidth. All calorimeter electronics is on the high performance side of good contemporary electronics and does not rely on next generation devices, nor on *just out* ones. Special attention needs to be devoted to the overall system. In order to control external noise, properly match signal cables and control signal grounds, the preamps are mounted directly on the PM bases, together with the voltage dividers, both requiring low power design to minimize the cooling required in enclosed places. The large number of preamps, ~7 000, located in inaccessible places requires special design to ensure high *mean time to failure*, MTTF. The proposed FEE design is shown in fig. 6.1.

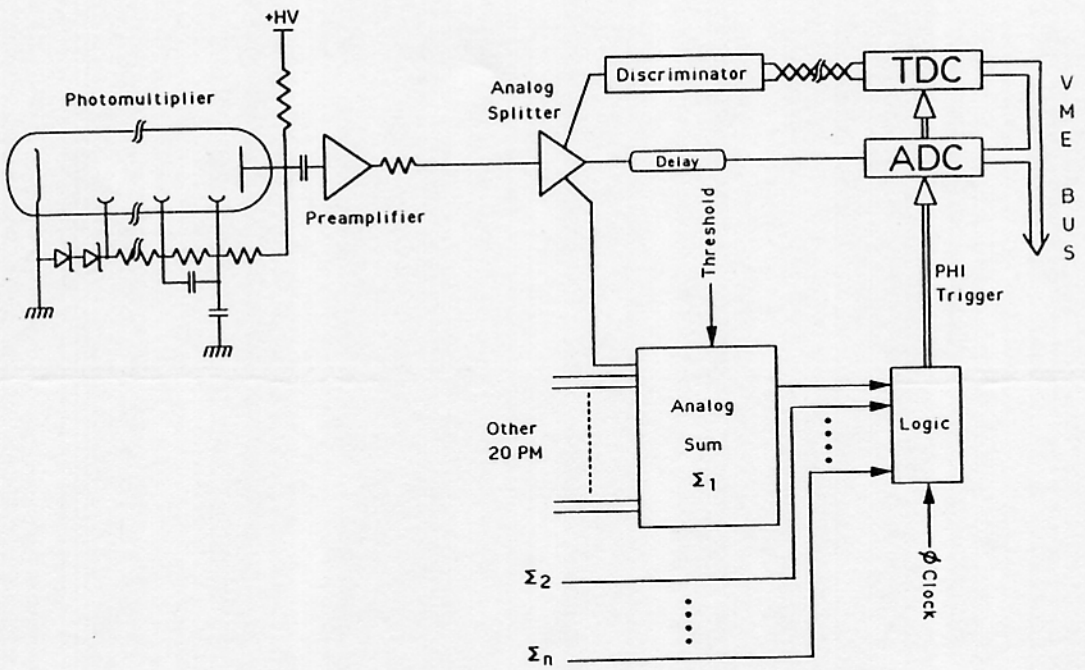

Fig. 6.1. Calorimeter front end electronics.

The PM choice is dictated by the ability to operate in a magnetic field and by low electron transit time spread, <0.3 ns, necessary to obtain a superior calorimeter time resolution. The total gain (PM plus preamp) required to obtain reasonable signals (50 mV for 20 MeV photons) is around 10^5. We will use a grounded cathode connection for the PM (positive high voltage) in order to remove possible sources of additional noise. The consequent capacitive coupling of the PM to the preamp is possible because of the low rate and the very short signals.

The PM anode signal current, averaged over ~10 ns, is 2.5 mA for a 500 MeV energy deposit or a charge of 25 pC. No tube will in fact see signals this large, since 500 MeV showers spread over several calorimeter blocks. We analyze, however, the effects of the values above. The average anode current is .15 nA reducing the HV across the voltage divider, made with 1 MΩ resistors, by 0.14 mV, corresponding to a gain change $\delta g/g = 1.1 \times 10^{-6}$ and a change in total tube transit time of 0.7 ps going from full to zero luminosity. These values are completely negligible

for our purpose. The instantaneous voltage drop, for 10 nF blocking and filter capacitors is 2.5 mV in the worse place, quite negligible. The average value above is approached in a fraction of a second.

A test signal, phase–locked with the machine clock, allows quick measurements of drifts in time and amplitude response of electronics plus cables. It also gives early warning on unstable or noisy channels.

The divider current is 100 μA to reduce power dissipation, $\sim$200 mW per tube. Nevertheless, given the high number of channels, cooling has to be provided, allowing us to eliminate any PM exposure to helium from possible chamber leaks.

Each PM signal has to be split three ways to provide the following functions:

1. amplitude measurements via ADC, to provide energy deposit information,
2. time measurements through a few channel multi-hit TDC after a constant fraction discriminator,
3. trigger generation from the analog sum of signals from adjacent channels (*i.e.* local calorimeter neighborhoods).

We have chosen a full scale of 500 MeV per channel and a 12 bit ADC, the least count corresponding to 0.12 MeV, assuring adequate precision for the detection of minimum ionizing particles which give a signal equivalent to 20 MeV γ's, and for the proper clustering of em showers.

The classical solution of delaying all signals until the formation of the trigger signal becomes unpleasant at the level of thousands of channels. Miniature delay lines, usually wound on high permeability thin foils of very large permeability are poor, expensive and sensitive to magnetic fields. A possible solution is continuous encoding of the signals, after appropriate shaping, at frequencies of 20-50 MHz and only 10 bits, with hardware signal processing to find time and amplitude of the signals at the relevant time.[57] . Recall that we must measure the energies deposited by particles arriving with a spread in time of 100–200 ns.

An alternative solution[58] which we are investigating is the continuous sampling of the output of integrators with a restoring time of about 50μs. Using three switches (and holding capacitors) which constantly toggle between follow and hold, each at a frequency of 1/(required integration time) and a phase delay of 1/2 the period, one can always obtain a valid baseline reading. Receipt of a trigger freezes two switches and extends the follow time of the appropriate one, to integrate all late arriving particles. The appropriate difference between signal and base line is obtained in analog and digitized by a conventional ADC. This method, extensively used in modern electronics practice, allows dynamical ranges well in excess of 1:32,000. Digitization time is the only dead time, which, however, can, to a large extent, be removed by a shadow set of switches which can process the next event while the first is being digitized. A channel is shown in fig. 6.2.

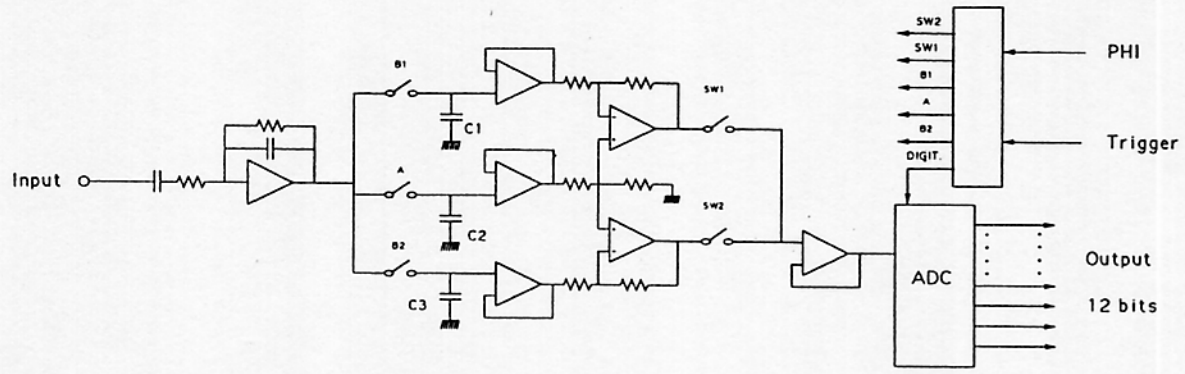

Fig. 6.2. Sampled data system principle.

A similar scheme[58] can be adopted for the TDC design, with the difference that switching is phase locked to the machine master clock, or better a local pick–up electrode detecting the beam bunch. Fig. 6.3 shows the principle. A multihit extension of the system is straightforward in this scheme with minimal cost increase.

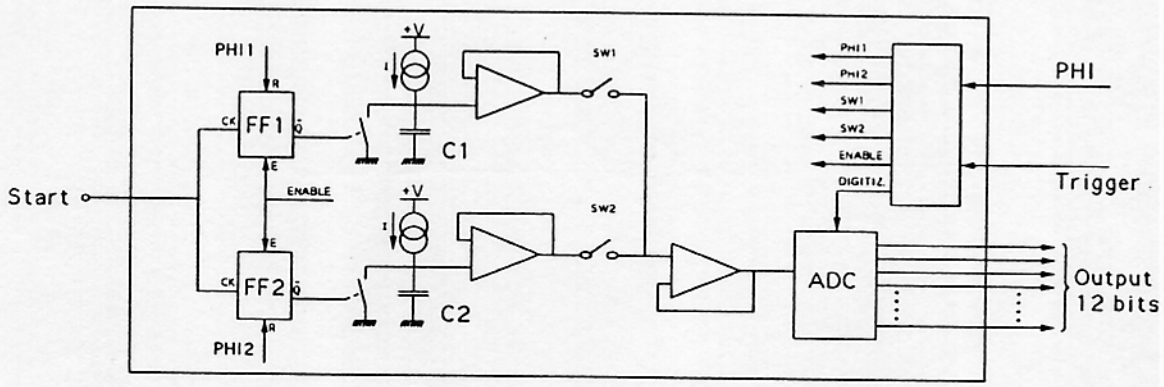

Fig. 6.3. Deadtimeless time-to-voltage converter.

Although the approaches presented above for both the TDC and ADC have a number of desirable features, such as base line control, lack of long delay cables, etc., intensive R&D is needed before final decisions can be taken.

This part of the electronics will reside in a VME environment. The use of vertical interconnects, for example VIC bus, will allow very simple data concentration prior to entering the fast switches of event builders for transmission to a microprocessor farm.

6.2 Chamber Signal Processing

6.2.1 Preamplifier

Preamplifiers must be mounted on the chamber face, for the same reasons given for the PM's. In addition they must have low mass, since they are in front of the EmC. Power considerations are more critical, because of the large number, ~27000, of wires. Many devices, in miniature

integrated packages, are available, providing excellent performance and extremely low mass. We have also developed some circuits at LNF.[59]

6.2.2 Data Acquisition

The block diagram for conventional data acquisition from a single wire is shown in fig. 6.4.

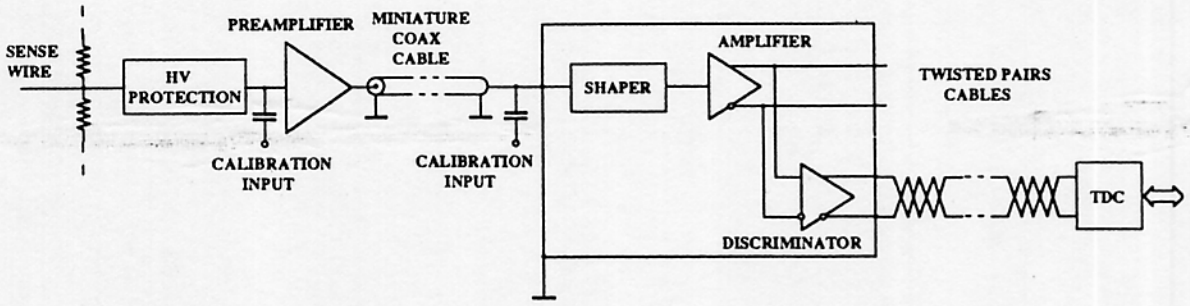

Fig. 6.4. Schematic of the front end chamber electronics.

The preamplifier output signals are transmitted by miniature 50 Ω cables to amplifiers and shaper circuits whose output drives a discriminator and is made available for amplitude measurements. We assume that the discriminators are mounted on the outer iron shell of KLOE, while the TDC's that follow are in the counting room, with the signals carried on twisted pair cables. We also plan to use a pulser for rapid system test.

It is not possible to give the exact cost per channel, because work is still in progress. However the cost of the electronics should be kept below 0.1 MLit per channel.

7. TRIGGER

7.1 INTRODUCTION

The physical processes yielding observable events in KLOE are: ϕ decays, ~5 kHz at full DAΦNE luminosity; Bhabha scattering, ~50 kHz for $8° < \theta < 172°$; muon pairs, ~100 Hz; non resonant hadronic channels, ~200 Hz.

In addition, there are backgrounds: cosmic ray muons, ~3-5 kHz, and machine background, for which an estimate is 1-10 Hz, for a total energy deposit in the calorimeter > 100 MeV, scaling from CESR, operating at 10 GeV.

Bhabha scattering represents an intolerable load for the DAQ system, yet it is a most valuable source of calibration events for time and energy scales. Cosmic ray muons can also help in this respect, although it might be desirable to reject them at some level. Machine background can be ignored, even at 10 times the expected rate, and filtered at event analysis time. The most important requirement of a trigger for KLOE, for the purpose of studying CP violation, is that it must be fully efficient, irrespective of the $K_{L,S}$ decay channels. An additional requirement is that it must identify Bhabha's in the region $\theta < 20°$, so that by prescaling, no more than a 5 kHz rate will be retained. Cosmic rays should be recognized and rejected at the trigger level.

A pure energy trigger, using calorimeter information should be quite adequate for the above requirements. Monte Carlo studies[60] show that if the signals from all calorimeter elements are added together, an energy threshold of 300 MeV gives 100% efficiency, see fig. 7.1 a), with extremely low sensitivity to machine background, <1 Hz rate, and appreciable cosmic ray rejection.

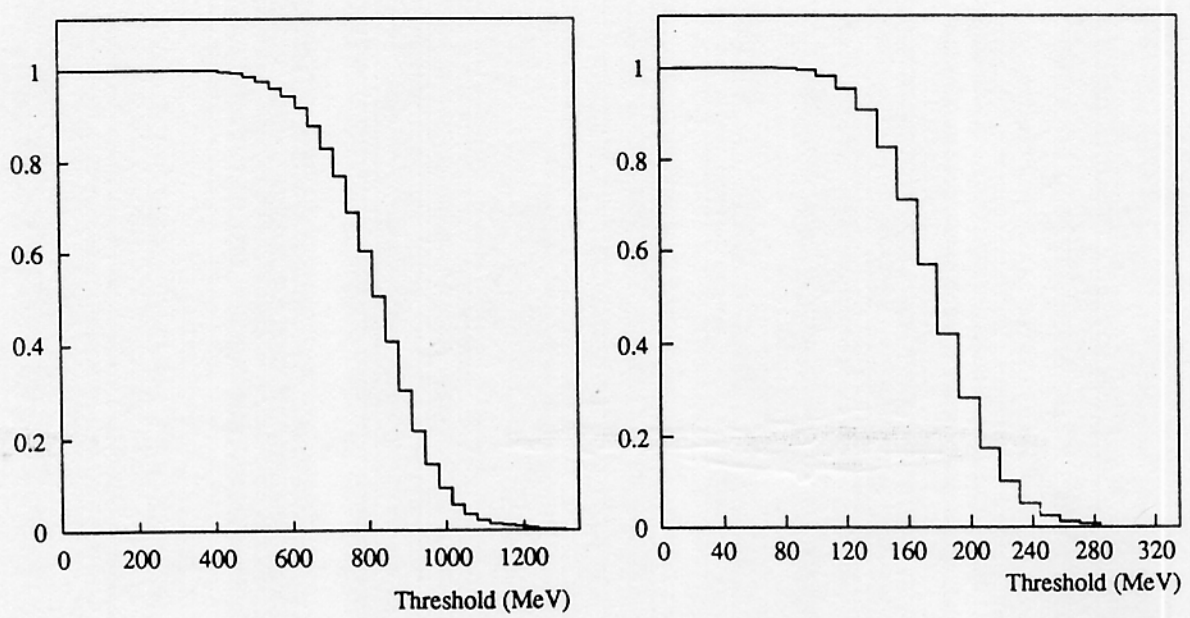

Fig. 7.1. Trigger efficiency vs threshold: a) total energy, b) single particle.

Such a trigger would not recognize Bhabha's. Another trigger can be based on the detection of small isolated energy deposits, such as those due to single γ's and charged particles, in the calorimeter. Again Monte Carlo studies show that an energy threshold of 100 MeV ensures 100%

efficiency, see fig. 7.1 b). This kind of trigger is also extremely effective in rejecting machine background, but has no discrimination against cosmic rays and Bhabha's.

Bhabha's can of course be easily identified by asking for two local large energy deposits, *i.e.* ≀00–500 MeV, and a loose collinearity requirement. The only processes capable of depositing $\mathcal{O}(1020)$ MeV in the calorimeter are due to decays $\phi \rightarrow$neutrals$\rightarrow\gamma$'s, with a vanishingly small probability for two single collinear clusters of $\mathcal{O}(510$ MeV) each.

A complication in the generation of the trigger is due to the fact that, owing to the low β of the kaons from ϕ decays, the energy signals can appear over a time interval of few tens of ns. Fig. 7.2 shows the time distribution of the arrival time of the first particle which gives a signal of 100 MeV or larger in the calorimeter. There is a large peak at t=0, due to photons and fast particles from the interaction point and a visible tail up to 30-40 ns later. Light propagation in the fibers adds an additional small time spread. For large delays, the correct crossing time must recovered using the reconstruction of the whole event.

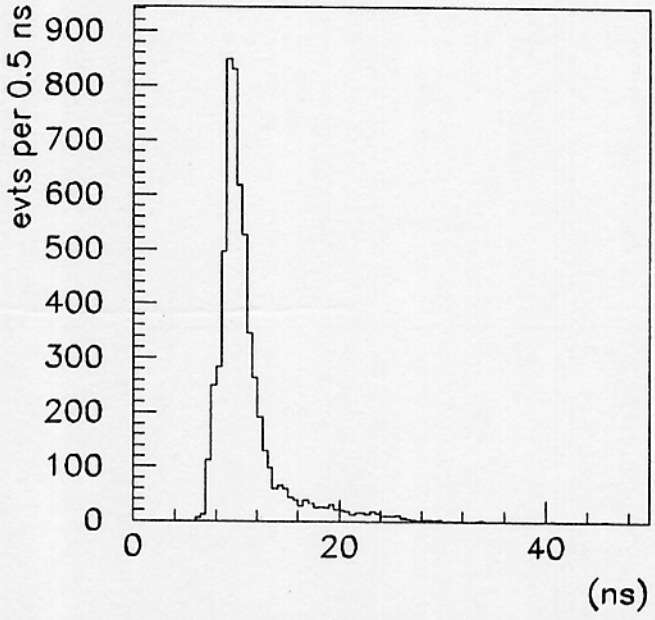

Fig. 7.2. Single particle arrival time for $E > 100$ MeV.

This is, of course, not true of Bhabha's, for which the arrival time of the two electrons is identical and has very little time spread. Because of the collinearity of the e^+e^- pair, light propagation times do not destroy the temporal coincidence.

7.2 Trigger Hardware

We intend to generate trigger signals based on both local energy deposits and total energy, with special provision for small angle Bhabha detection and prescaling. Signals from adjacent calorimeter read–out elements, called calorimeter segments in the following, are summed in fast, precision analog adders, the PM preamp is ideally suited for this, and compared with settable thresholds to obtain an efficient single particle trigger, together with the first time of arrival. The elementary scheme above must be duplicated for the two readouts on the ends of each KLOE calorimeter element. Clustering must also be duplicated, with a half segment shift, in order to ensure correct detection of energy deposits on segment boundaries. A subdivision of the

detector, for trigger purposes, into 50 segments, requires 200 channels of summing, comparison and very simple random logic. Times for each of the listed steps is around 1-5 ns, for a total of perhaps 10 ns, although likely be larger in practice, due to the interconnecting cables.

A second level sum can produce a total energy trigger. In this case *slow* adders are necessary, to sum over all energy deposits within the spread of arrival times. Comparison of the two trigger responses can provide a measure of trigger efficiencies, since the global trigger can be made much more efficient, without acquiring sensitivity to machine background. Fig. 7.3 shows an example.

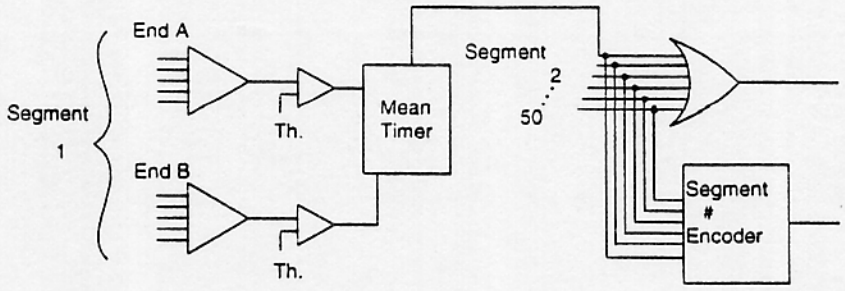

Fig. 7.3. Local energy deposit trigger.

For those calorimeter elements exposed to small angle Bhabha's, a duplication of the isolated trigger is necessary. For each end-cap it is necessary to cover a circle of r <64 cm. Assuming full shower containment in 14 cm of transverse dimension, 4×4=16 sums of 22 signals each must be produced and compared with energy thresholds on the order of 510 MeV, 440 MeV is an adequate value. The sums above must be doubled, with a shift of 7 cm, to maintain full efficiency for electrons entering the edge of a local calorimeter environment. A total of 44 discriminator outputs per end-cap are therefore produced. Some simple combinatorial logic can then check for approximate collinearity and time coincidence at the few ns level. The complete Bhabha trigger can be contained in 2–4 VME cards, 9U high. It should be remarked that the overall Bhabha detection efficiency needs to be only on the order of 90%, since only a factor 10 rejection is required; insensitivity to ϕ decays must be kept very low. No true space collinearity is used, but only collinearity, after projection in the $\{x, z\}$ plane, is required. Timing, with respect to the beam crossing time and the difference at the two ends of each module, provides information on the y point of impact of the e^+e^- on the end-cap planes. We do not believe this to be necessary.

Bhabha and ϕ decay events which overlap in time are recognized by the trigger described and can be passed to the DAQ system.

8. DATA ACQUISITION

At full DAΦNE luminosity, ϕ decays and calibration events represent a very large load for the data acquisition system, corresponding to a data production rate of ~50 MBytes/sec, after filtering cosmic rays and reducing the Bhabha contribution. We assume that at the maximum DAΦNE luminosity of 10^{33} the data acquisition event rate is about 15 kHz, divided among:

1. ~5 kHz for the ϕ decays
2. ~5 kHz for the Bhabha scatters after filtering at the trigger level from a total of 50 kHz produced
3. ~5 kHz for unfiltered cosmic rays
4. we also assume that all other background contributions are well below 1 kHz.

Assuming that the subsystem event lengths from the electromagnetic calorimeter and from the tracking chamber are 1–2 kBytes each, as estimated from Monte Carlo calculations, the average bandwidth required is 25–50 MBytes/sec. The data acquisition system will be configured in a expandable way, initially supporting a throughput of about 100 MBytes/sec. The system scalability, both in hardware and software, will assure the ability to support a larger throughput if required.

A general scheme of the data acquisition system is jointly proposed by the KLOE and ALSAT collaborations[61–63] that are evaluating with the use of a FDDI switch (the Gigaswitch), FDDI protocol and Alpha-chip based processors, to configure data acquisition systems for new accelerators, and in particular to configure the event builder and the farm system for the KLOE data acquisition system. This scheme is presented in the fig. 8.1. Data coming from the trigger system, the electromagnetic calorimeter and the tracking chamber, that were accepted by the 1st level trigger, are collected in several readout systems that interface through VME crates with the rest of the data acquisition system. These readout systems are configured so as collect data from different parts of the apparatus, with the criteria of balancing the throughput distribution. Eleven of these sub-detector readout systems are proposed: one for the trigger, five for the calorimeter and five for the chamber.

All the data accepted by the 1st level trigger system are sent to a parallel event building system, FDDI based, that reconstructs and analyzes the full event using a farm of RISC processors. The event flow controller, implementing the run control functions, is the central acquisition computer that is also connected to "VME" and the farm system through separate channels. Data are finally stored on tape for further reprocessing. We anticipate the development of methods to reduce the amount of stored data, both at the first level trigger and at a second level trigger to be implemented in the farm system.

Sub-detector readout, event building, farming, and monitoring and control will be discussed briefly in the following sections.

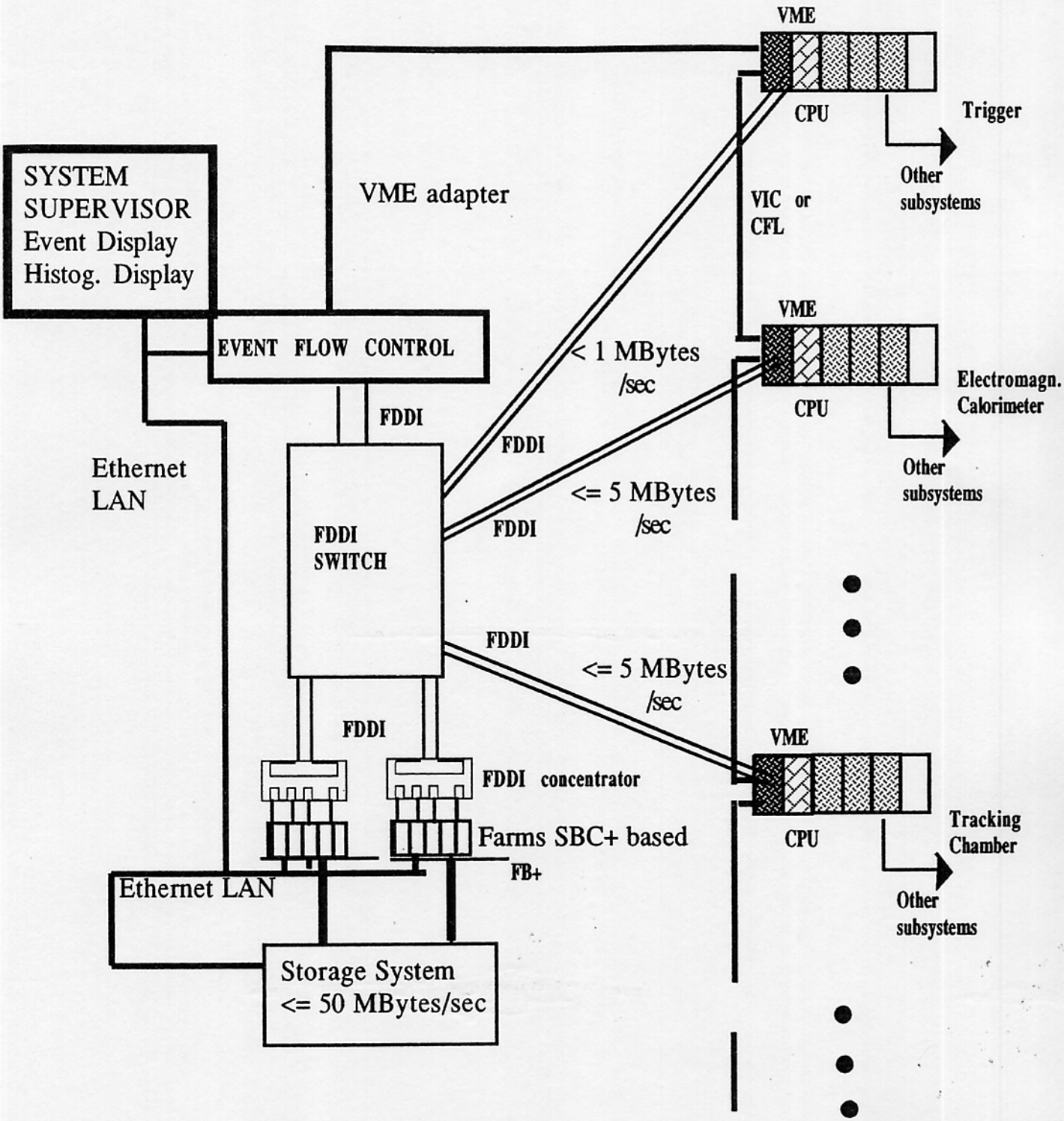

Fig. 8.1. Data acquisition architecture.

8.1 Readout

Data accepted by the 1st level trigger are collected into a DAQ network of VME crates. This choice meets the requirements of a large bandwidth back-plane (15 Mbytes/sec sustained, 35 Mbytes/sec peak) and the availability of high performance CPU boards, running very efficient real time operating systems. Each VME crate branch manages data from a given sub-detector.

Multi-event buffers in the VME crates will accommodate data consisting of parts of events coming from sub-detectors, to be sent to the event-builder system through the FDDI channels in an asynchronous way with respect to the read-out system. Many pieces of events can be buffered together before being sent to the event builder system; this strategy will optimize the FDDI channel performance.

Through the inter-crate network, information related to event building and processing will be sent between the event flow controller, the trigger crate and the sub-detector readout crates. On each crate specialized tasks will run, in order to monitor sub-detector activity and data transmission.

8.2 Event builder

The event builder in a data acquisition system receives data from various detector elements, organizes these data into complete events and distributes these events to the processors in a farm. The event builder functions presented in the fig. 8.1 are distributed in three main components. The sub-event building in the VME readout controller, the transmission of the different sub-events to a farm using a parallel switch matrix, that is presented in this section, and finally the complete event building in the farm.

Parallel event builders realized using switch matrices are intrinsically scalable because the aggregate bandwidth grows linearly with the number of channels. Commercial switched networks can be used to implement these kinds of event builders. Industrially supported communication links and network protocols can strongly facilitate the management and maintenance of such a system.

The Gigaswitch proposed for KLOE allows parallel interconnections at the maximum FDDI throughput of 100 Mbps, using 22 different ports. Each port has an internal buffer of 4 MBytes and two optical fiber channels allowing a full-duplex connection. Stations are connected to the switch using the two fibers. A full-duplex connection is obtained when this connection is configured as a point-to-point link, allowing the elimination of the FDDI token. In this case, the two lines can separately use the maximum FDDI throughput.

The Gigaswitch implements a bridge protocol between input and output ports that does not require store and forward procedures. The total time needed to recognize the path and to configure the switch is about 10-20 μs. The maximum transfer packet rate is about 6.25 Mega packets/sec.

The Gigaswitch ports are connected to:

1. the event flow controller
2. every readout controller
3. every farm sub-system

The event flow controller implements the following functions related to the event building:

1. Receives trigger-number information from the trigger system
2. Assigns a farm address to a trigger-number
3. Communicates these assignments to the readout controllers.

In this way, data coming to the Gigaswitch from the readout controllers and related to a given event-number contain a unique destination address: the address of the farm element where the complete event will be elaborated. The bridge protocol inside the Gigaswitch concentrates these data into the farm queue.

Simulations of this model has been studied using Verilog-C language tools .[64] In this model the farm is assigned depending on the actual farm queue length, which is communicated to the event flow controller by the farm every time a new event is received. The results of the simulation show that the Gigaswitch does not introduce significant delays in the traffic, while its internal buffers allow the implementation of a completely asynchronous event building system.

8.3 Farm

The on-line farm has to perform the following tasks :

1. Dynamically inform the event flow controller about the ability to receive data from individual farm elements. The data inputs are buffered, and form queues of events to be processed in a continuous way by the local CPU. As soon as these input buffers are emptied the CPU lares its availability to receive other data.
2. The end part of the event building. To optimize the transfer rate, groups of pieces of events, corresponding to the same sub-detector, are sent together via the FDDI channels to the single elements of the on-line farm. In addition these data from different sub-detectors arrive in a random way, and have to be re-ordered. The integration of these pieces of events in a data structure should be done before the final processing. The event building algorithm should also analyze and discard incomplete events or events with transmission errors and keep track of this information.
3. Event reconstruction. Full on-line event reconstruction and analysis should possibly be performed by the farm processors, once the detectors and the trigger logic are fully tested. The aggregate CPU power needed for this task was evaluated at 20000 MIPS. At the beginning of the data taking the farm will be mostly used to check the quality of the events and to perform partial event reconstruction.
4. Output of the (reconstructed) events. The raw data of the accepted events should be made contiguous by copying them, together with the reconstruction information, to large output buffers. From time to time the accumulated events will be sent in streaming mode to the storage sub-system. The system should support an aggregate output rate of 50-100 Mbyte/sec.
5. Communicate with the DAQ supervisor sub-system, sending statistics and bookkeeping information, allowing event stripping for analysis and display, etc.

To reach the required processing power the on-line farm is thought to be a modular cluster of more than 10 computing sub-systems. The single sub-system is composed of a group of

single board computers in a Futurebus+ crate (150 Mbyte/sec throughput). A Joint Project INFN-DEC, initiated by the ALSAT collaboration, has been set up for the development of the prototype of such a Single Board Computer. The project foresees the use of the new ALPHA 21064 chip from (150 MHz cycle time, full 64 bit architecture, dual-pipelined), embedded in a board (called SBC+) with at least 16 Mbyte of memory and interfaced to Futurebus+, to FDDI (via a FDDI single attachment port) and possibly to Ethernet. The SBC+'s will run one of the real-time operating systems (VAXELN or DECELX), after adapting to the board architecture.

Each SBC+ receives data individually from an FDDI ring, built from a FDDI concentrator (with FDDI dual attachment ports), which in turn is connected by a single port to the FDDI switch. This configuration allows one to replace a SBC+ without stopping the whole computing sub-system. To take advantage of the Futurebus+ bandwidth, more crates will be bridged together, conveying the output data from their SBC+'s to the identical interfaces in the storage system. Higher level protocols which will assure some flow control facilities over the FDDI logical layer are under study.[65] The full modularity of both the farm and the switching system should assure the expandability of computing and data flow capabilities of the DAQ system.

Several architectures and tape systems are under study to find a better storage system. Technical solutions which are already in the marketplace could fulfil the KLOE needs, for instance, they could be connected to FB+ in two or three separated streams. Commercial distributed database systems, based on the new IEEE storage models under development, will be investigated.

8.4 System control and monitoring

The run control functions are performed by a central acquisition computer, which distributes the commands (e.g., begin run) to all the processors in the acquisition network via Ethernet links. The switch matrix, used as the event builder, allows a "natural" partitioning of the acquisition system into independent sub-detector groups, such as monitoring and debugging; the matrix can be configured in preprogrammed paths in order to assign a subset of the processor farms to a particular sub-detector, allowing a software environment in which multiple parallel data acquisition systems run concurrently. For general monitoring purposes, such as histogramming and event display, the processor farm, if enough resources are left (memory, CPU) can send complete events to the central computer, via the Ethernet links. The central computer inserts these events in a data stream and makes them available, upon request, to local/remote multiple processes.

9. PHYSICS PERFORMANCE

9.1 Detector Simulations

9.1.1 Task specific

A number of different detector simulations were used during the design of KLOE. Many use special, simple geometric modelling and very simple event generation, often more physically correct than the clumsy GEANT means of dealing with phase space, which have the virtue of being extremely fast but task specific. In this way event samples $>10^7$ can be produced.[66] In addition, more specialized and realistic subdetector simulation such as GEMS[67] and EMCAL[68] are used for subcomponent design.

9.1.2 GEANFI

GEANFI, A general Monte Carlo program based on the Geant code,[69,70] has been developed, and optimized in execution time and disk space usage.[71] GEANFI includes the generation of the relevant ϕ and kaon decay channels, the description of the machine interaction diamond together with a realistic geometry of the KLOE experimental set-up. The machine interaction zone is described by introducing the proper beam pipe shape (8 cm radius at the interaction point), three pairs of low β quadrupoles, and the ϕ decay kinematics are simulated assuming that e^+ e^- beams cross at a half angle of 15 mr. A beam energy spread of 700 keV is assumed and radiative corrections are taken into account. GEANFI handles ϕ decays into K^+K^-, K_SK_L, $\pi^+\pi^-\pi^0$ and the decays of neutral and charged kaons. The neutral kaon decay modes include the CP-violating channels, and for the 2 pion decays the effect of the interference in the decay rates of the 2-kaon system is included. The $K_{\mu 3}$, K_{e3} decays include the $V-A$ matrix elements. Generators of other processes including ϕ radiative decays, Bhabha scattering, $\gamma\gamma$ interactions are available. K_L, K^- hadronic interactions are handled correctly.[72]

The experimental set-up consists of a central chamber with conical end-plates, and of a sampling calorimeter with Pb-scintillator planes, 0.07 X_0 each, for a total radiation length of 16 X_0. The EmC consists of a central barrel section, divided into 24 modules in the transverse plane, and two end-cap sections. The geometrical parameters and the materials used in each subsystem of the detector, as well as its segmentation, can be redefined from default values via *data cards*. For each detector unit (*e.g.*, wire layers in the central chamber, and planes in the EmC) position, momentum, deposited energy, time of flight and particle type are saved. The output consists of the standard Geant banks, read by a package developed inside the collaboration that allows easy access to data for subsequent analysis.[73] It is also possible to make some choices concerning the particle tracking that considerably reduce the execution times. The user can turn off, for example, the full shower development in the calorimeter, saving only the impact points.

The time needed to simulate one $\phi \to K_SK_L \to \pi^+\pi^-\pi^0\pi^0$ event is 7.2 s on a VAXstation 4000-60; including full em shower development in the calorimeter. The event size is 28.4 blocks, in average. When particles are not followed inside the calorimeter the time is 0.5 s and the event size 8 blocks.

9.1.3 Event Display

We have also written event display programs which show the reconstructed tracks in the

chamber and clustered energies in the EmC.[7.4] An event display of $\phi \to K_S K_L$ with $K_S \to \pi^0\pi^0$, $K_L \to \pi^+\pi^-$ is shown in fig. 9.1. An event display of $\phi \to K_S K_L$ with $K_L \to \pi^0\pi^0$, $K_S \to \pi^+\pi^-$ is shown in fig. 9.2. In both events three out of four photons are in the barrel EmC.

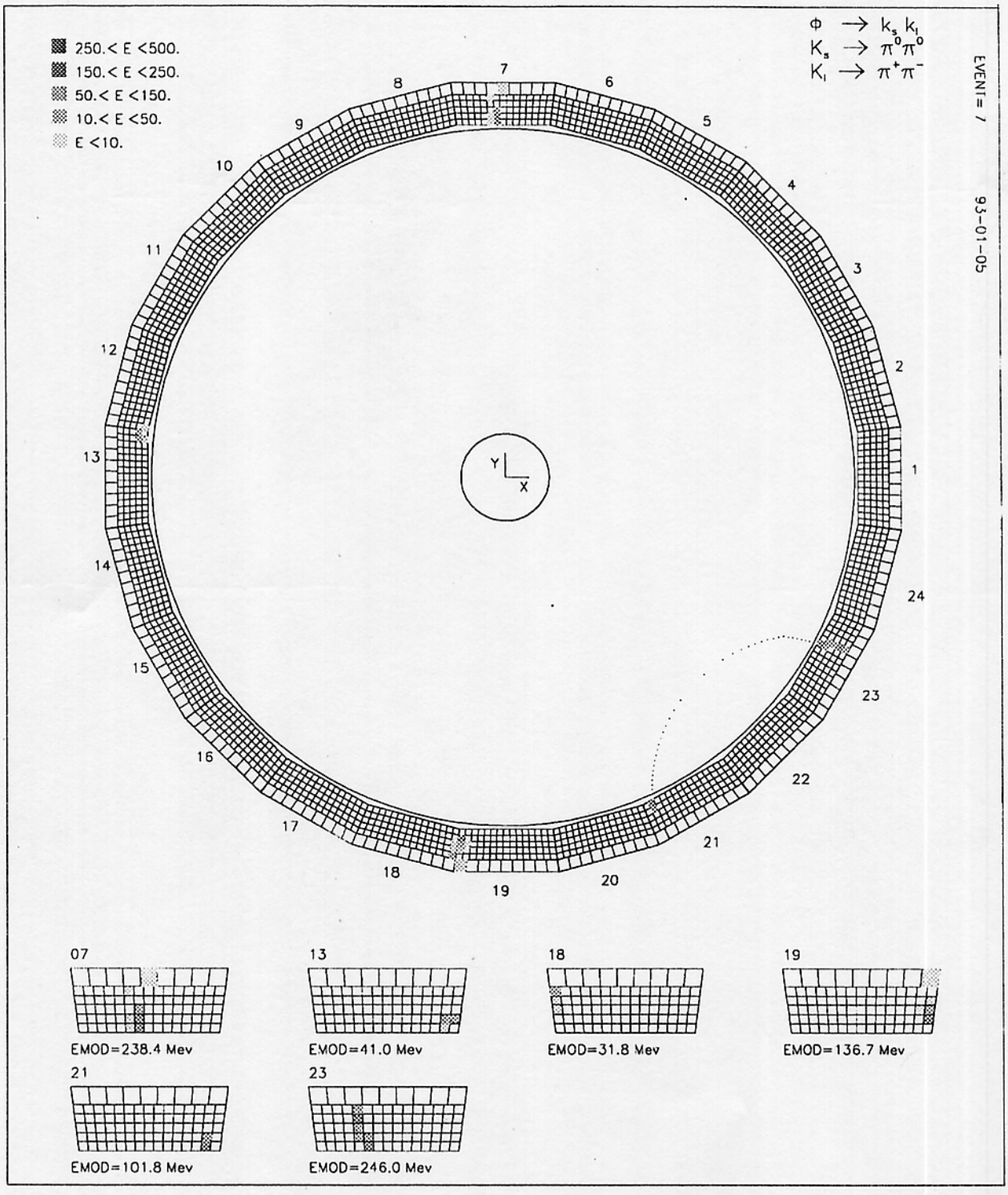

Fig. 9.1. Display of a $\phi \to K_S$, $K_L \to \pi^0\pi^0$, $\pi^+\pi^-$ event.

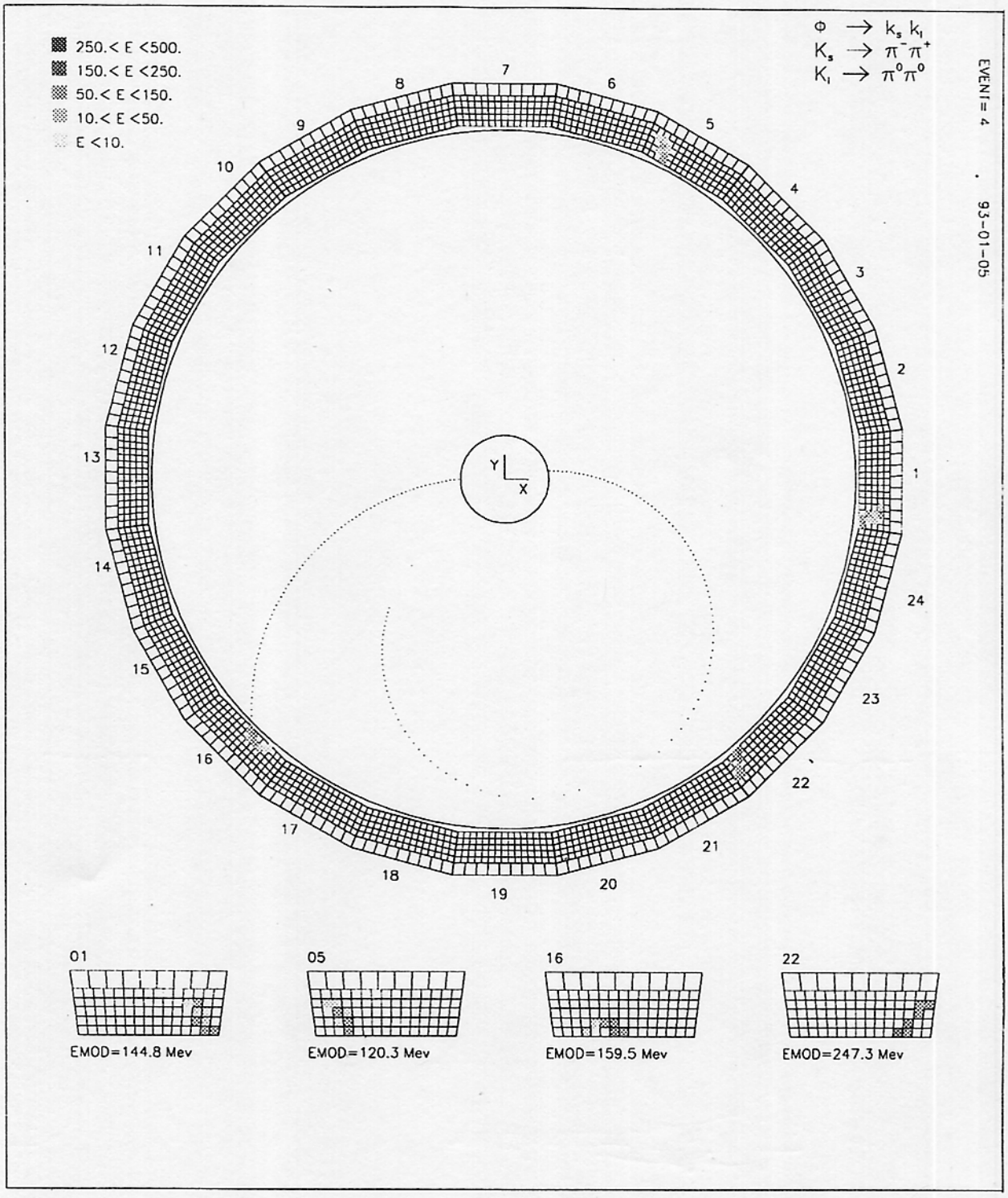

Fig. 9.2. Display of a $\phi \to K_S$, $K_L \to \pi^+\pi^-$, $\pi^0\pi^0$ event.

9.2 Detector resolutions

9.2.1 Charged Tracks

Tracking in KLOE is non-trivial because tracks can begin at any point in the chamber volume, tracks may spiral through 2π, $\sim$20% for K_L at 6 kG, and low energy pions undergo $\pi \to \mu$ decays. Our present tracking program is adapted from the ARGUS[75] program, to

the KLOE geometry.[39] This tracking routine has the virtue of being able to handle spiralling tracks with the same accuracy as non-spiralling ones.

15381 $K_L \to \pi^+\pi^-$ decays inside the fiducial volume have been analyzed using a chamber accuracy in r, ϕ of 200 μm, assuming 107 layers, a radial wire drop of 1 cm, and varying the magnetic field B, from 4 to 8 kG. A geometrical cut of at least 6 hits in the chamber has been used for track fitting. While the resolutions improve with increasing B, reconstruction losses are barely seen to increase with B. A 6 kG field is taken to be an optimal choice after background studies, see the following chapter.[76] Using 13400 $K_L \to \pi^+\pi^-$ decays at each field value, we found this behavior to be also true for a chamber with 84 layers.

The corresponding experimental resolutions are given in table 9.1 and the tracking and fitting efficiencies in table 9.2.

TABLE 9.1. Experimental resolutions for $K_L \to \pi^+\pi^-$ as a function of B.

Performance		Magnetic field, (kG)		
Variable	Resolution	5	6	7
$(P_T^{fit} - P_T)/P_T$ (%)	R.M.S.	1.53	1.49	1.47
	σ	0.35	0.33	0.29
$(P_z^{fit} - P_z)/P_z$ (%)	R.M.S.	3.32	3.23	3.23
	σ	0.65	0.64	0.63
$\phi^{fit} - \phi$ (mrad)	R.M.S.	13.9	14.5	14.6
	σ	1.60	1.66	1.71
$(\cot\theta)^{fit} - \cot\theta$	R.M.S.	2.98×10^{-2}	3.00×10^{-2}	2.99×10^{-2}
	σ	0.29×10^{-2}	0.30×10^{-2}	0.30×10^{-2}
$M_{\pi\pi}^{fit} - M_{\pi\pi}$ (MeV)	R.M.S.	5.40	5.12	4.87
	σ	1.01	0.90	0.87
$\sum E_\pi^{fit} - \sum E_\pi$ (MeV)	R.M.S.	8.16	7.88	7.91
	σ	1.21	1.10	1.03
$X_{vertex}^{fit} - X_{vertex}$ (mm)	R.M.S.	2.04	2.09	2.07
	σ	0.44	0.44	0.45
$Y_{vertex}^{fit} - Y_{vertex}$ (mm)	R.M.S.	1.97	2.03	2.12
	σ	0.45	0.45	0.45
$Z_{vertex}^{fit} - Z_{vertex}$ (mm)	R.M.S.	3.63	3.75	3.74
	σ	1.17	1.17	1.19

The R.M.S. values in the above table are partly an artifact of the present analysis, since $\pi \to \mu$ decays have not been removed from the sample. They result in long tails in the distributions.

TABLE 9.2. Track and "V" efficiencies as function of B.

Magnetic field, (kGauss)	5	6	7
Single track efficiency(geom+recons)	98.8%	98.7%	98.6%
Event efficiency(geom+recons)	97.7%	97.4%	97.2%
Total track losses:	1.2%	1.3%	1.4%
Geometry, no. of hits > 5	0.2%	0.2%	0.2%
Reconstruction	1.0%	1.1%	1.2%
Total event losses	2.3%	2.6%	2.8%
Geometry, no. of hits > 5	0.4%	0.4%	0.4%
Reconstruction	1.9%	2.2%	2.4%

9.2.2 Photons

In the following we assume as fiducial volume for K_L decays a sphere of 150 cm radius. ~35 % of the K_L's decay in this volume. We exclude decays within a cylinder of 30 cm radius around the beams, along the z axis, to remove $K_L \to K_S$ regeneration. In evaluating the performance of the EmC we assume 100% detection efficiency down to photon energy of 20 MeV, an energy resolution of $\sigma_E/E = 4.8\%/\sqrt{E/1\ \mathrm{GeV}}$, a temporal resolution, including attenuation, of $\sigma_t = 35\sqrt{\cosh z/\ 2.7\mathrm{m}}/\sqrt{E/1\ \mathrm{GeV}}$ ps. The spatial resolution for the photon apex is $\sigma_{r\phi;\, barrel} = \sigma_x, z;\, end-cap = 3.5/\sqrt{12} = 1$ cm from the read out granularity and $\sigma_{z;\, barrel} = \sigma_y;\, end-cap = 2.2$ cm (averaged over the photon spectrum) from time differences. The time information is crucial to the reconstruction of the $\pi^0\pi^0$ decay vertex. In fact, if the K_L line of flight is known from the reconstruction of the $K_S \to \pi^+\pi^-$ on the other hemisphere, the $\pi^0\pi^0$ vertex can be obtained for each photon from the time measurement.

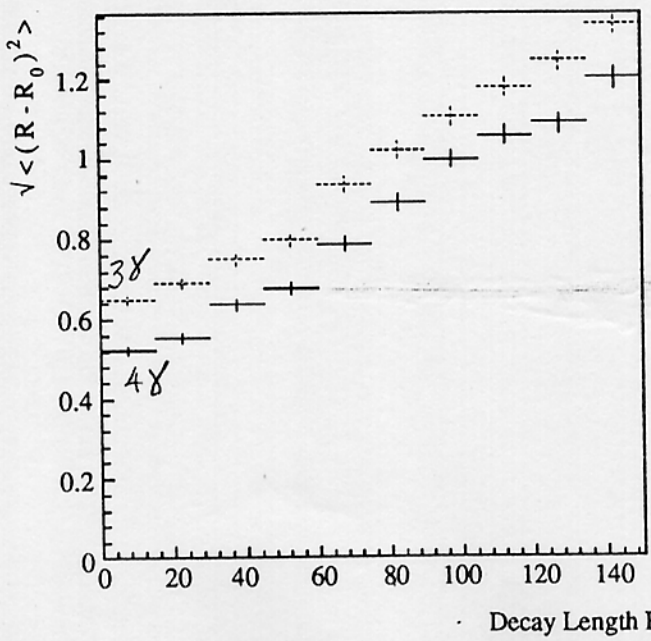

Fig. 9.3. RMS spread of the reconstructed radial distance of the $K_L \to \pi^0\pi^0$ vertex vs r.

The resolution for the $K_L \to \pi^0\pi^0$ vertex has been studied, assuming a resolution on the transverse momentum p_T of charged pions of 0.003 p_T, of 0.002 radians on the azimuthal angle, and $\sigma_{tan\delta}$=0.005 for the dip angle . The vertex position is obtained by a constrained fit which requires the invariant mass of the 4 γ system to be equal to the K_L mass, and the invariant mass of each 2 γ pair to be equal to the π^0 mass. The radial resolution σ_r (along K_L line of flight **r**) worsens with the distance r; σ_r=5.1–12.0 mm for r=10–150 cm, see solid line in fig. 9.3. The K_L vertex can be reconstructed also for events with only 3 photons detected. The spatial resolution is about 20% worse,[77] see dashed line in fig. 9.3. The vertex resolution for $K_S \to \pi^0\pi^0$ decays is σ_x=3.6 mm, σ_y=3.2 mm, σ_z=1.83 cm.

The resolution for the invariant four photon mass M from $K^0 \to \pi^0\pi^0 \to 4\gamma$ using the pion mass and beam energy constraints, is shown in fig. 9.4, σ_M=3.1 MeV. The resolution for M is approximately linear in the EmC energy resolution but rather insensitive to the spatial and temporal resolutions of the calorimeter.[77]

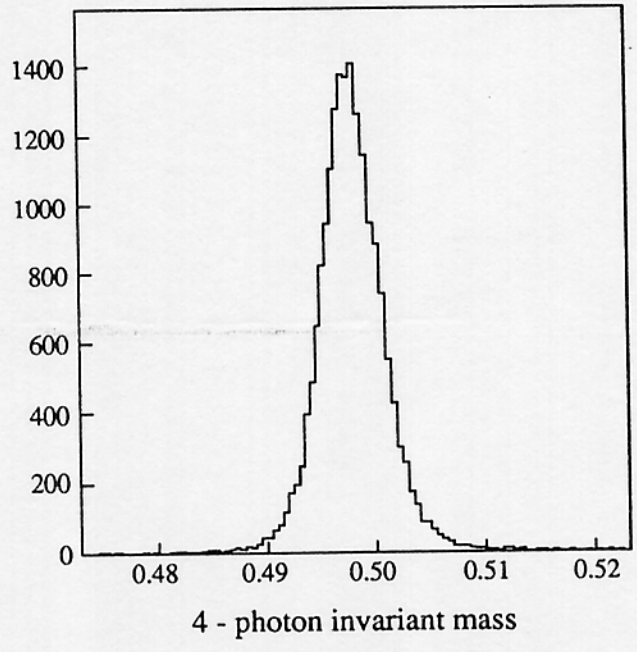

Fig. 9.4. $M(4\gamma)$ distribution for $K^0 \to \pi^0\pi^0 \to 4\gamma$.

10. DETECTOR EFFICIENCIES AND BACKGROUNDS

10.1 Main Tracking Chamber Efficiency

10.1.1 Geometric losses

The fraction of short tracks from $K_L \to \pi^+\pi^-$ with <6 hits in our chamber is 1.6% ± .1%, in the range of magnetic field from 4 to 8 kG. These losses are purely geometrical, about one quarter of the loss is due to pion decay. Their contribution, $\Delta\epsilon_{recon}$, to the systematic error on the reconstruction efficiency of $K_L \to \pi^+\pi^-$ can be estimated from the wire efficiency, ϵ_{wire}, and the result is shown in fig. 10.1, for a range of ϵ_{wire} from 90% to 100%, assuming an accuracy of $\Delta\epsilon_{wire}$ from 0.1% to 0.5% . We note that as long as $\Delta\epsilon_{wire}$ is <0.3%, the contribution to $\Delta\epsilon_{recon}$ is negligible when added in quadrature.

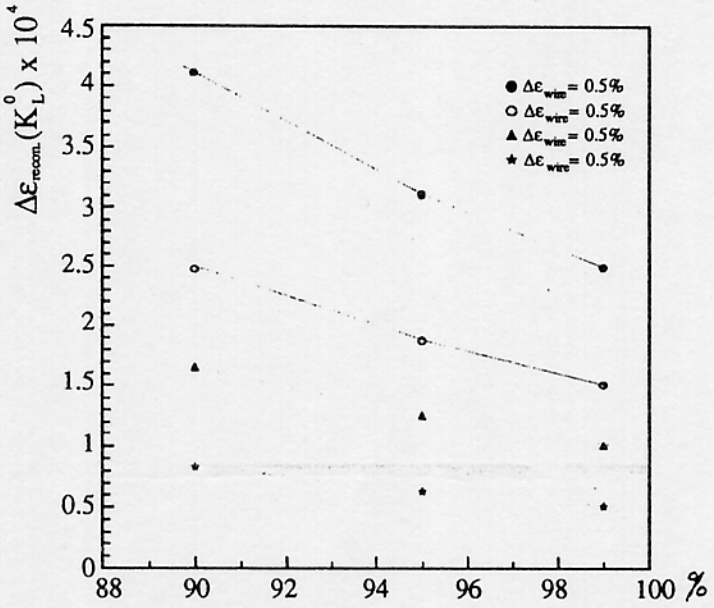

Fig. 10.1. $\Delta\epsilon_{recon}$ vs ϵ_{wire}.

It is quite easy to monitor $\Delta\epsilon_{wire}$ to 0.3%, assuming for example ϵ_{wire}=95%, one needs 5.5×10^3 tracks to measure the average layer efficiency to that accuracy, and since each track crosses 84 wires, one needs 1.6×10^6 tracks to measure the efficiency for all the wires in the chamber to 0.3% accuracy. Since we have 5000 two track events/sec in the detector, it takes half a second to achieve such accuracy per layer, and 2.1 minutes to measure the efficiency of each of the 27,000 wire (on average) to that accuracy. If we use only $e^+e^- \to \mu^+\mu^-$ events ~50Hz for $45° < \theta < 135°$, it takes 50 sec to reach a 0.3% accuracy per layer, and approximately 3.4 hours to measure the efficiency for all 27,000 wires.

10.1.2 Reconstruction losses

These losses are due to bad χ^2 or fit nonconvergence because of pion decays, non gaussian measurement errors due to multiple scattering or drift times, and fitting routine limitations. We can monitor the geometrical and reconstruction track losses by using $K^+ \to \pi^+\pi^+\pi^-$ events. At full luminosity, we will have 8.0×10^8 events/year. Fitting the K^+ and the three pion tracks we reconstruct the $K^+\pi^+\pi^+\pi^-$ vertex. About 40% of these events have all 3 pion tracks reconstructible (that is with at least 6 hits in the chamber). From the ratio of cases with 2 or 3 pion tracks fitted one may derive the track fit efficiency. Assuming then a track fitting efficiency of

99%, we estimate that it can be measured to an accuracy of 10^{-4} in ~10 hours at full luminosity, integrated over momentum and decay point. We therefore can also obtain the decay point and momentum dependence of the track fit efficiency using a larger data sample.

10.1.3 Vertex reconstruction losses

Causes for poor vertexing are short tracks or tracks which are almost 180 degrees apart (very rare). This may result in a bad χ^2 or a large uncertainty on the vertex position for a few percent of the K_L decays into charged tracks. In particular those decays happening close to the fiducial volume boundaries may contribute to the systematic error. These losses may be corrected for by using the results of the single charged track fit and the K_L direction as inferred from the reconstruction of the $K_S \to \pi^0\pi^0$ on the opposite hemisphere.

10.1.4 Vertex Chamber Monte Carlo Study

A special MC study has been performed to study the impact of inserting a vertex chamber, as described in section 5.11, within the tracking chamber.[78] Unfortunately, at present, both the central drift chamber assumed and the tracking routine utilized are not the optimized ones, thus the study's results can only be used as an indication of the usefulness of adding such a chamber, but give an underestimate in the absolute efficiency of the system. The following assumptions are used: 70 μm and 200 μm single hit resolution for the vertex detector and the drift chamber respectively, $5\%/\sqrt{E\ (\mathrm{GeV})}$ and 45 ps$/\sqrt{E\ (\mathrm{GeV})}$ for the energy and time resolutions of the electromagnetic calorimeter. $\phi \to K_S K_L$ events, with $K_S \to \pi^+\pi^-$ and $K_L \to \pi^0\pi^0$, were generated and, then, fully reconstructed obtaining the results shown in table 10.1, without and with the vertex chamber.

TABLE 10.1. Monte Carlo results for $\phi \to K_S$, K_L events.

Fit	Resolution	DC only	DC + VC
Single track	$\sigma(p_t)$, MeV	0.73	0.74
	$\sigma(\phi)$, mr	5.3	4.4
	$\sigma(\tan\lambda)$	8.3×10^{-3}	7.9×10^{-3}
	$\sigma(D_o)$, mm	1.2	0.4
	$\sigma(Z_o)$, mm	2.4	1.1
K_S vertex	$\sigma(x)$, mm	1.9	1.0
	$\sigma(y)$, mm	1.5	0.8
	$\sigma(z)$, mm	2.1	1.1
event vertex	$\sigma(x_v)$, mm	2.6	1.7
	$\sigma(y_v)$, μm	30	30
	$\sigma(z_v)$, mm	2.7	1.7

For the single charged track reconstruction the use of the vertex detector improves, as expected, the resolution on the initial direction of the track, while leaving the p_T resolution almost unchanged. After a kinematical fit, the resolution of the reconstructed $K_S \to \pi^+\pi^-$ vertex is improved by about a factor of two using the vertex detector. The event vertex resolution also improves, although to a lesser extent than the K_S vertex, being more affected by the reconstruction of $K_L \to \pi^0\pi^0$. Furthermore the efficiency for reconstructing $K_S \to \pi^+\pi^-$ increases by ~10%.

10.2 PHOTONS

The energy scale and time of flight scale of the electromagnetic calorimeter will be continuously measured as described in the chapter 4.

10.2.1 Energy Calibration

Bhabha events (5000/sec) are a copious source of calibration events for the calorimeter. However they originate from the interaction region, and have fixed energy (510 MeV/c). Radiative Bhabhas do provide a continuum. We can also use $K^+ \to \pi^+\pi^0$ events which yield photons of lower energy. The yield is 1.5×10^9/year at full DAΦNE luminosity. Each photon energy can be kinematically reconstructed by using $\mathbf{p}_{\pi^0} = \mathbf{p}_{K^+} - \mathbf{p}_{\pi^+}$ (from the track fit) and the photon impact point. The corresponding energy resolution is $1.5\%/\sqrt{E}$, (see fig. 10.2); precise enough to check the calorimeter energy response.[79]

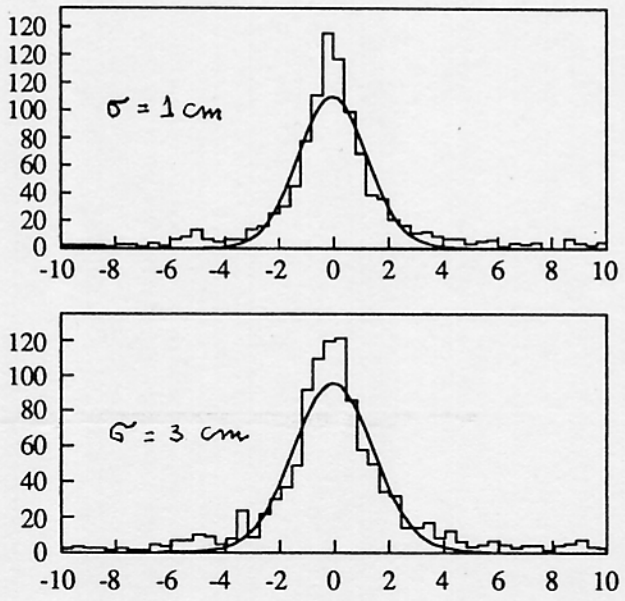

Fig. 10.2. Photon energy resolution, in %, for fitted $K^+ \to \pi^+\pi^0$ events.

10.2.2 Time of Flight Calibration

Bhabha's and $K^+ \to \pi^+\pi^0$ decays can also be used to check the time of flight, T_f, calibration. A fitted T_f is obtained from the fit of the K^+ momentum and the distance traveled by one of the photons between the K^+ decay point and its impact point at the EmC. The distribution of the difference, $\Delta T_f = T_{f,obs.} - T_{f,fit}$ has a rms of about 400 ps, about half of which comes from the K^+'s T_f spread. This last effect can be eliminated by taking the difference of the T_f's of the two photons, which has a dispersion of 300 ps. During data taking we can check that this distribution is centered around zero, confirming that the neutral vertex coincides spatially with the charged vertex. Note that we do not need to know the absolute spatial scale for vertex reconstruction since, in the ratio of $K_L \to \pi^+\pi^-$ to $K_L \to \pi^0\pi^0$, it drops out.[79]

10.3 BACKGROUNDS

10.3.1 $K_L \to \pi^+\pi^-$, $K_{\mu 3}$

A realistic study of the methods for removing $K_{\mu 3}$ contamination has been developed, based

on past work and the study described above of the chamber resolutions. In particular the error distributions of the measured quantities now include[80] non gaussian tails, as obtained in the track simulation work. Also a large event sample, 1.35×10^7 $K_{\mu3}$ and 10^5 $K_L\to\pi^+\pi^-$, was generated, using the standard size of the luminous region, σ_x=0.2 cm, σ_y=20 μm, σ_z=3 cm. $K_{\mu3}$ and $K_L\to\pi^+\pi^-$ events are distinguished by the use of a χ^2 function constructed using the measured variables corresponding to the all kinematical constraints available. A double Gausssian parametrization has been applied to the resolution functions (in p_T, ϕ, cot(θ), vertex position) obtained from reconstructed GEANFI generated tracks, using the ARGUS–KLOE program for an 84 layer stereo chamber, to take the tails into account.

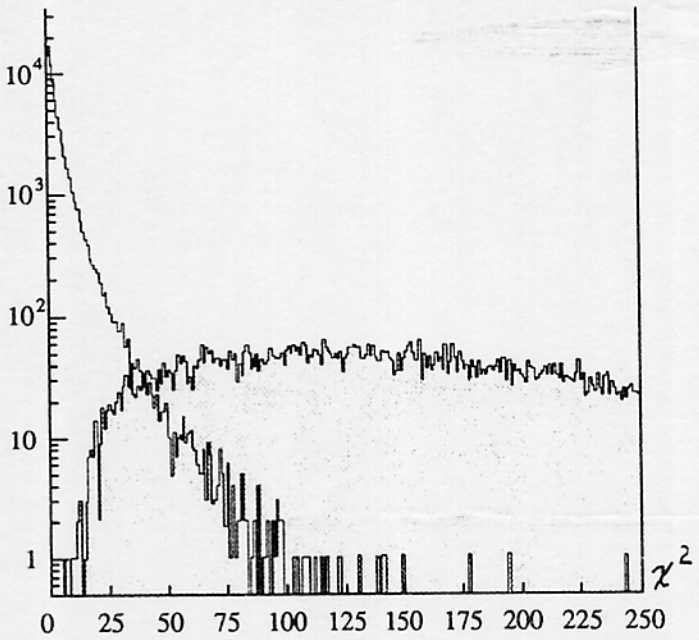

Fig. 10.3. Number of events vs χ^2 for $K_L\to\pi^+\pi^-$ events and $K_{\mu3}$ events, cross hatched.

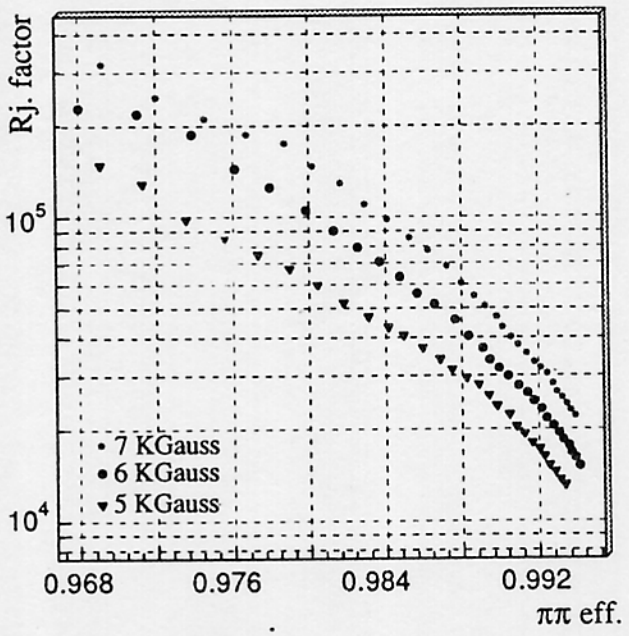

Fig. 10.4. $K_{\mu3}$ rejection factor vs $K_L\to\pi^+\pi^-$ efficiency for different B values.

The χ^2 function is peaked at very low values for $K_L\to\pi^+\pi^-$ decays, while for $K_{\mu3}$ events it

vanishes at 0 and extends to very high values, see fig. 10.3. This calculation has been repeated for several values of the magnetic field from 4 to 8 kG. Fig. 10.4 shows the rejection factor for $K_{\mu 3}$ vs efficiency for two pions from $K_L \to \pi^+\pi^-$ for B=5 to 7 kG. The rejection factor at 6 kG is approximately 4.5×10^{-4} with a $\pi^+\pi^-$ signal efficiency of 98.8%.[81]

10.3.2 $K_L \to 2\pi^0/3\pi^0$

Photon losses must be minimized to reject $K_L \to \pi^0\pi^0\pi^0$ decays which can simulate $K_L \to \pi^0\pi^0$ if two photons are lost. For $K_S \to \pi^0\pi^0$ events, photon are lost in forward/backward regions, $\theta < 9°$ and in the calorimeter cracks. Photons from K_L decays are also absorbed in the quadrupoles. The fraction of $K_L \to \pi^0\pi^0$ decays with 3 or 4 photons detected is ~99.6%.

We have generated 10^8 $K_L \to 3\pi^0$ events and 4.65×10^5 $K_L \to \pi^0\pi^0$ events in the standard KLOE fiducial volume. Because of the large solid angle covered by the EmC, requiring exactly 4 detected photons already brings the $3\pi^0$ efficiency down to 9.2×10^{-3} , while preserving 89.5% of the $2\pi^0$ events. With the assumption that the quadrupoles are covered with devices which can detect photons above some minimum energy, but with no other information, the $3\pi^0$ efficiency is further reduced to 1.2×10^{-3}. A fit of the best combination of 4γ events to the $2\pi^0$ hypothesis is then used, to improve the determination of photon energies (without applying any χ^2 cut).

Scatter plots of $(\Delta M - \Delta E)/\sigma$ vs $(\Delta M + \Delta E)/\sigma$ for the $2\pi^0$ and $3\pi^0$ cases are shown in fig. 10.5 and fig. 10.6 respectively. A combination of cuts on 4γ energy (E), invariant mass (M) and acollinearity between the K_L direction and that of the sum of the four photon momenta, further lowers the $3\pi^0$ efficiency to or below the 10^{-6} level, at the cost of a 3% reduction of the signal, fig. 10.7.[82]

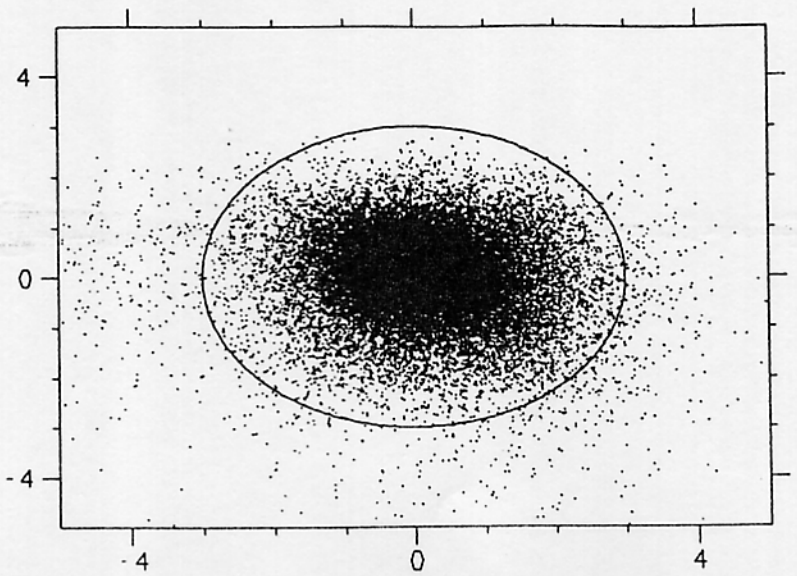

Fig. 10.5. Scatter plot of $(\Delta M - \Delta E)/\sigma$ vs $(\Delta M + \Delta E)/\sigma$ for $2\pi^0$.

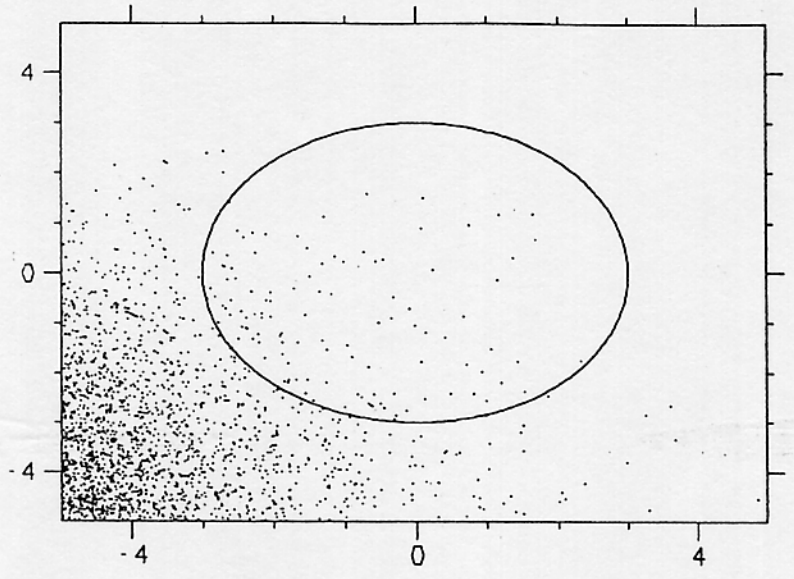

Fig. 10.6. Scatter plot of $(\Delta M - \Delta E)/\sigma$ vs $(\Delta M + \Delta E)/\sigma$ for $3\pi^0$.

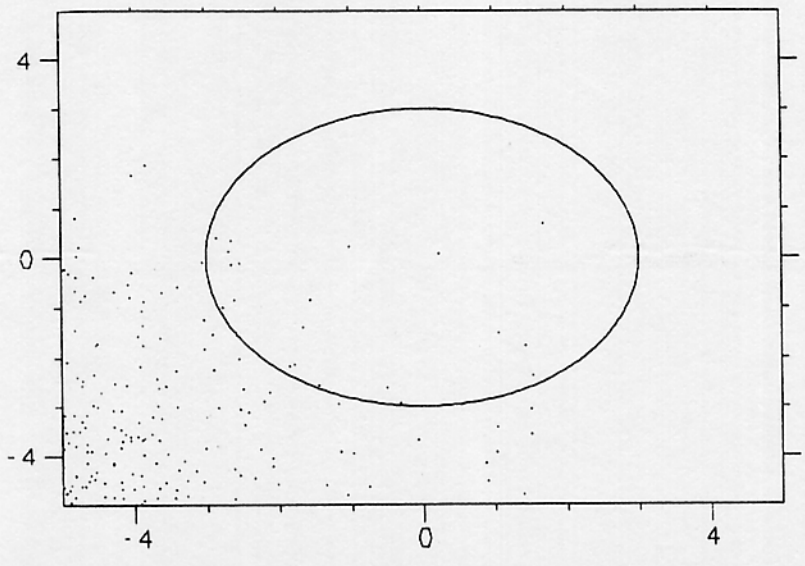

Fig. 10.7. Scatter plot of $(\Delta M - \Delta E)/\sigma$ vs $(\Delta M + \Delta E)/\sigma$ for $3\pi^0$, with cuts.

We also intend to use $K_L \to \pi^0\pi^0$ events where three photons are detected for the $\Re(\epsilon'/\epsilon)$ measurement. Further studies are in progress with regard to the background from $3\pi^0$ yielding only 3 photons in the detector. The rejection factor there is expected to be equally effective.

11. EARLY PHYSICS ANALYSES

11.1 Spectroscopy

Beginning late 1995, DAΦNE will deliver a luminosity $\mathcal{L} \approx 10^{32} cm^{-2} s^{-1}$, yielding some five billion ϕ's in four months of machine-on time. While the main goal of DAΦNE is the study of CP violation, an important complementary goal is spectroscopy. A particularly interesting state, the $f_0(975)$,[83] the lightest scalar ($I^G J^{PC} = 0^+0^{++}$) meson, has been a puzzle since the 1970's. If it is assumed to be a $q\bar{q}$ bound state, many predictions fail, such as the total width (500 MeV rather than the measured 30 MeV), two photon couplings and so on. Other structures, such as four-quark bound states or $K\bar{K}$ "molecules," have been proposed for the f_0. The current predictions[83] for the branching ratio of $\phi \rightarrow f_0\gamma$ (BR) vary from $\mathcal{O}(10^{-4})$ for various four quark states, to $\mathcal{O}(10^{-5})$ for $s\bar{s}$ states, to $< \mathcal{O}(10^{-5})$ for diffuse $K\bar{K}$ systems. The experimental upper bound is currently 2×10^{-3} at 90% c.l. With several thousand to a million produced f_0's per year, DAΦNE is an ideal place to study the f_0. A complete study, including derivations of energy and angular distributions of the signals and backgrounds, has shown that BR's ranging from 1×10^{-6} to 2.5×10^{-4} can be measured with 5×10^9 ϕ's.[84]

11.2 Analysis Programs

Thus, spectroscopy is an ideal physics project which can be done well even during the early stages of the machine's start up period. We have therefore developed a set of programs which include tracking,[39] energy clustering and event reconstruction,[84] event display,[74] which could accomplish the spectroscopy goals, were DAΦNE to deliver beams today and KLOE installed. The added bonus is that they can also be used to commission the KLOE detector for CP studies, as they have been used to study the magnetic field value choice and chamber design, see chapter 5, and background rejection studies.[76]

One observes f_0's through their decay to pions, a 78% branching ratio. First consider the decay of f_0 to neutral pions. The signal for $\phi \rightarrow f_0\gamma$ is five photons, with one low energy photon of about 50 MeV, and the other photons reconstructing to two nearly back-to-back pions. We adapted the CUSB photon cluster algorithm to the KLOE geometry. Fig. 11.1 shows an event display where all five photons are detected in the barrel EmC. Fig. 11.2 shows the mass spectrum of the f_0 reconstructed from 2500 $\phi \rightarrow f_0\gamma \rightarrow \pi^0\pi^0\gamma$ events.

When the f_0 decays to a pair of charged pions, the pions are almost 180 degrees apart.

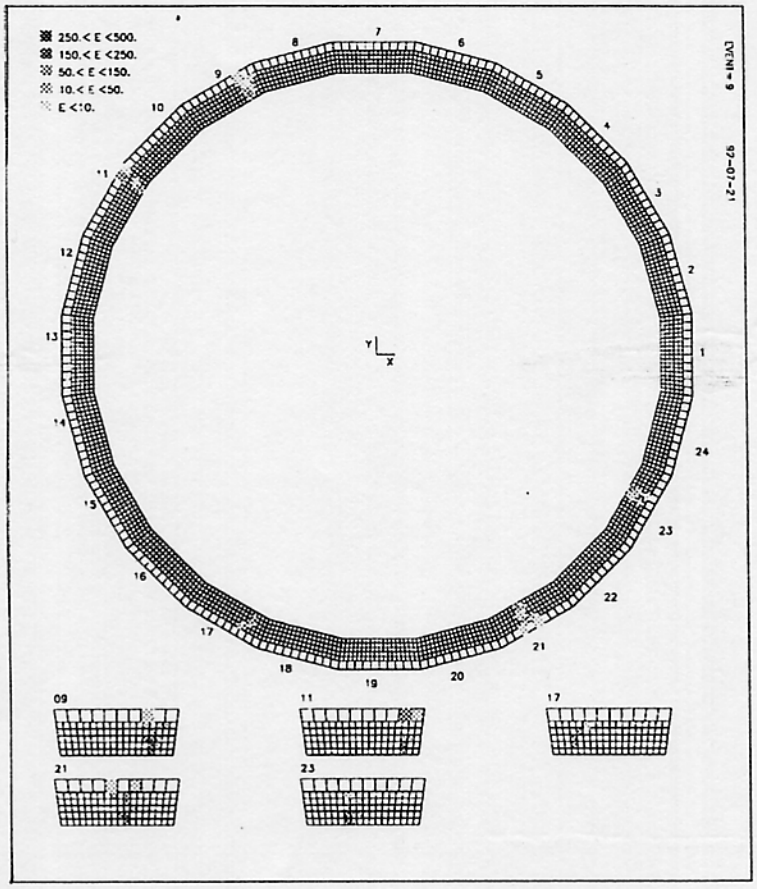

Fig. 11.1. $\phi \rightarrow f_0\gamma \rightarrow \pi^0\pi^0\gamma$ event display.

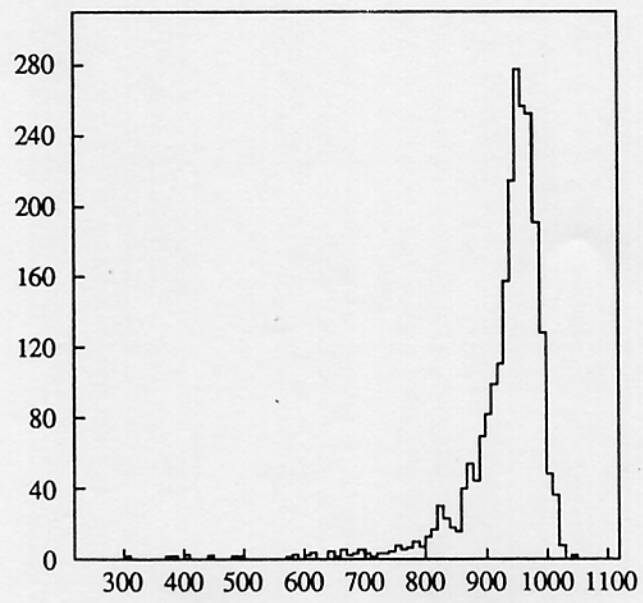

Fig. 11.2. Reconstructed f_0 mass spectrum, $f_0 \rightarrow \pi^0\pi^0$.

Fig. 11.3 shows an event display of $f_0 \rightarrow \pi^+\pi^-$ where the tracks have been reconstructed.

Fig. 11.4 shows the reconstructed ϕ mass spectrum from 1396 $\phi \rightarrow f_0\gamma \rightarrow \pi^+\pi^-\gamma$ events obtained by combining the f_0 reconstructed in the chamber with the photon cluster in the EmC.

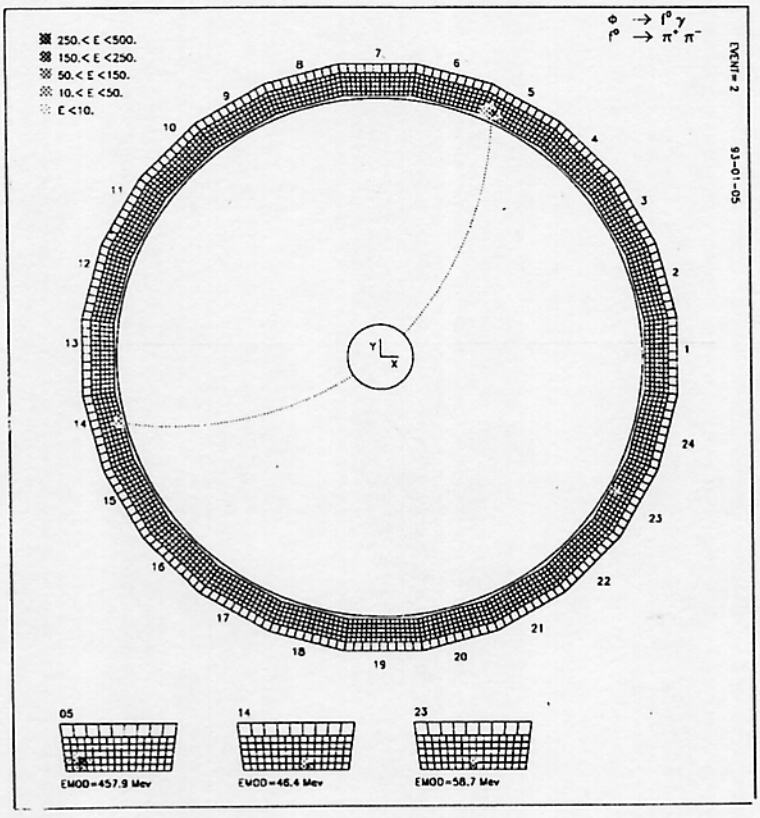

Fig. 11.3. $f_0 \rightarrow \pi^+\pi^-$ event display.

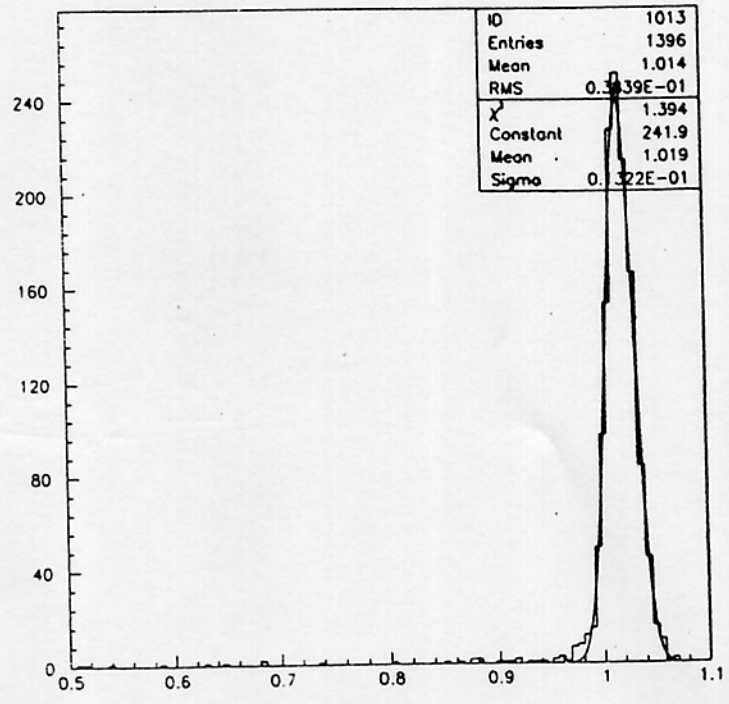

Fig. 11.4. Reconstructed ϕ Mass Spectrum, $\phi \rightarrow f_0\gamma \rightarrow \pi^+\pi^-\gamma$.

12. CONSTRUCTION SCHEDULE

12.1 Construction Schedule

Fig. 12.1 shows the "time" chart for the construction of KLOE. At present the critical path is the magnet construction, the chamber being a very close second.

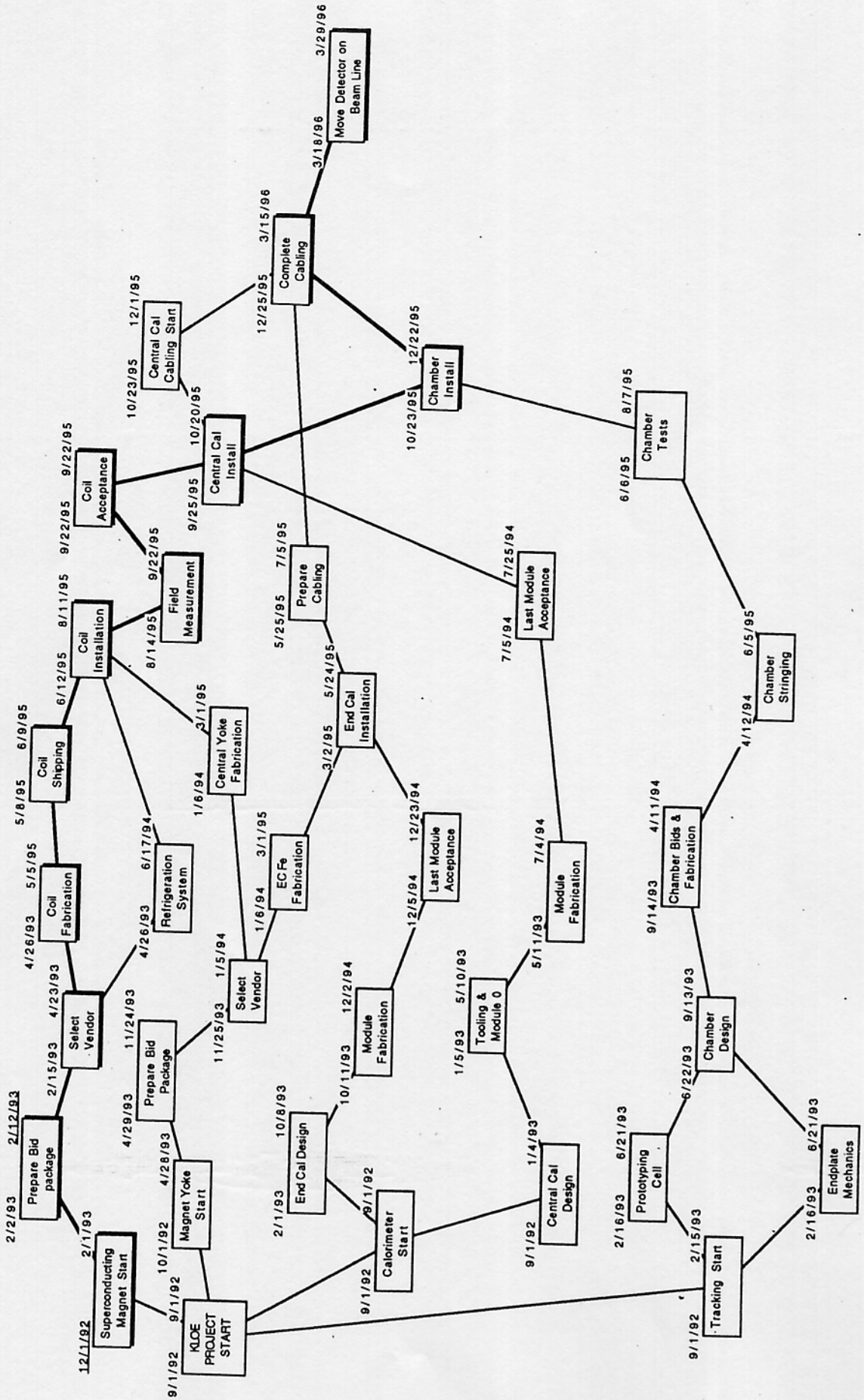

Fig. 12.1. KLOE Construction Schedule.

REFERENCES

1. "KLOE, A General Purpose Detector for DAΦNE", the KLOE Collaboration, Report LNF-92/019, April 1, 1992.
2. J. H. Christenson *et al.*, Phys. Rev. Lett. **13**, 138 (1964).
3. NA31, presented by G. Barr at *ISLEP (1991)*, Geneva, ed. Hegarty *et al.*, (World Scientific, 1992) p. 179; E731, presented by B. Winstein, *ibid* p. 186.
4. Both CDF and DØ have intentionally leaked information on events possibly due to top production at TEV–I.
5. I. Dunietz *et al.*, Phys. Rev. **D35**, 2166 (1987).
6. P. Franzini, in *Workshop on Physics and Detectors for DAΦNE*, ed. G Pancheri, (INFN-LNF, 1991) p. 733.
7. V. Patera and A. Puglisi, in *The DAΦNE Physics Handbook*, ed. L. Maiani *et al.*, (INFN-LNF, 1992) 87-104.
8. C. Buchanan *et al.*, Phys. Rev. **D45**, 4088 (1992).
9. J. Lee-Franzini, in *Les Rencontres de Physique de la Vallée D'Aoste*, Ed. M. Greco, (Edition Frontières, 1992) 349- 368; LNF Preprint LNF-92/046; in *'92 Electroweak Interactions and Unified Theories*, Ed. J. Tran Than Van, (Edition Frontières, 1992) 381-398.
10. The CLEO detector, C. Bebek *et al.*, Nucl. Instru. Methods Phys. Res., Sect A**265**, 258 (1988).
11. The Committee consists of: F. Bonaudi, chair, P. Layzeras and G. Petrucci.
12. D. W. Hertzog *et al.*, Nucl. Inst. Meth. **A294**, 446 (1990) used similar techniques.
13. M. Kuhlen *et al.*, CALT-68-1648, Aug. (1990).
14. S. Bertolucci *et al.*, Proc. *Workshop on Frontier Detectors for Frontier Physics*, La Biodola, Italy (1991); KLOE Note (1990).
15. D. Babusci *et al.*, Proc. *Workshop for Detectors and Physics at DAFNE*, (INFN-LNF, 1991) p. 581.
16. A. Antonelli *et al.*, Proc. *Workshop for Detectors and Physics at DAFNE*, (INFN-LNF, 1991) p. 557.
17. C. Bloise *et al.*, Proc. *Workshop for Detectors and Physics at DAΦNE*, (INFN-LNF, 1991) p. 495.
18. S. Bianco *et al.*, *Proc. 5th Pisa Meeting on Advanced Detectors*, Nucl. Instr. and Meth., **A315**, (1992) 322-326.
19. Nuclear Enterprise NE581 optical epoxy.
20. BICRON BC600 optical epoxy.
21. A. Ceccarelli and B. Dulach, LNF Tech. Note **92/051** (1992) (in Italian).
22. T. Welfor and R. Winston *The Optics of Nonimaging Concentrators*, Academic Press, (1978) p. 76.
23. C. Bini *et al.*, KLOE Note #43 (1992).
24. C. Bini *et al.*, KLOE Note #42 (1992).
25. G. Barbiellini *et al.*, KLOE Note in preparation.
26. S. Miscetti *et al.*, KLOE Note #11 (1991).
27. S. Bianco *et al.*, KLOE Note #10 (1991).
28. S. Sarwar *et al.*, KLOE Note in preparation.
29. S. Sarwar *et al.*, KLOE Note #46 (1992).
30. S. Bertolucci *et al.*, KLOE Note #45 (1992).
31. D. Babusci *et al.*, *Progr. in Part. and Nucl. Phys.*, **24**, (1989).
32. S. Bianco *et al.*, Lead-scintillating fibers calorimetry for low-energy photons, presented by S. Sarwar at the *3rd Int. Conf. on Calorimetry in High-Energy Physics*, Sept. 29–Oct. 2, (1992), Corpus Christi TX (USA).
33. S. Bianco *et al.*, KLOE Note #24 (1992).
34. F. Bossi and G. Capon, KLOE Note #5 (1991).

35. G. Lanfranchi, Thesis: *Misura dei Parametri etc. (in Italian)* (1992).
36. W. W. Cooley and P. R. Lohnes *Multivariate Data Analysis* Wiley, New York 1971; SPSS Inc. *SPSS: Statistical Package for the Social Sciences* 2nd ed. by Norman H. Nie *et al.*, (New York, Mc Grow-Hill).
37. F. Murtas *Thesis: Acquisizione ed Analisi dati del prototipo del Calorimetro Adronico di ALEPH* (1988).
38. S. Bianco *et al.*, KLOE Note 47 (1993).
39. A. Andryakov, KLOE Note in preparation.
40. P. Burchat *et al.*, pre-print SLAC-PUB 5745, Feb. (1992).
41. P. Giubellino *et al.*, Nucl. Instr. and Meth. **A252**, 528 (1986); J. Va'vra, Nucl. Instr. and Meth. **A252**, 547 (1986).
42. See the CLEO II Drift chamber description in D.G. Cassel *et al.*, Nucl. Instr. and Meth. **A252**, 325 (1986).
43. Opal Drift Chamber: R.D. Heuer *et al.*, Nucl. Instr. and Meth. **A265**, 11 (1988).
44. Elettra Drift Chamber: J.L. Benichou *et al.*, Nucl. Instr. and Meth. **A 217**, 163 (1983).
45. Venus Drift Chamber: R. Arai *et al.*, Nucl. Instr. and Meth. **A217**, 181 (1983).
46. Helena Drift Chamber:H. Albrecht *et al.*, Desy int. rep. Desy 92-41.
47. R. J. Roark and W. G. Young: Formulas for stress and strain, Mc Graw Hill (1985).
48. D. S. Koetke, SLAC–Report 396, June (1992).
49. A. A. Vorobyov *et al.*, Nucl. Instr. and Meth. **A310**, 167 (1991).
50. L. Baksay *et al.*, Nucl. Instr. and Meth. **A310**, 607 (1991).
51. W. W. Ash *et al.*, Nucl. Instr. and Meth. **A261**, 399 (1987).
52. P. Baringer *et al.*, Nucl. Instr. and Meth. **A254**, 591 (1987).
53. J. Adler *et al.*, Nucl. Instr. and Meth. **A276**, 42 (1989).
54. M. Frautschi *et al.*, Nucl. Instr. and Meth. **A307**, 52 (1991).
55. R. De Sangro, KLOE Note in preparation.
56. G. Bencivenni and G. Felici, KLOE Note in preparation.
57. P. Franzini, KLOE Note in preparation.
58. M. Cordelli, KLOE Note in preparation.
59. G. Felici, KLOE Note in preparation.
60. M. Baroni *et al.*, KLOE Note in preparation.
61. A. Farilla *et al.*, Alta Luminosita' e Sistemi di Acquisizione e Trattamento dati, INFN-project, 1992-1994.
62. A. Farilla *et al.*, Projects of data acquisition systems for experiments at high luminosity facilities, CHEP92, Annecy 21-25 Sept, 1992.
63. A. Guglielmi, *et al.*, A Futurebus+ Single Board Computer using Digital's new 21064 RISC CPU, OBS92, Zurich, October 1992.
64. M. L. Ferrer, E. Pace, and E. Pasqualucci, KLOE Note #37 (1992).
65. M. L. Ferrer, E. Pace, and C. Stanescu, KLOE Note #30 (1992).
66. F. Bossi and G. Capon, KLOE Note #05 (1991), A. Calcaterra, KLOE Note #12 (1991), C. Gatto, KLOE Note #14 (1991), J. Lee-Franzini, W. Kim and P.J. Franzini, KLOE Notes #17 (1991) and #28 (1992), F. Anulli *et al.*, KLOE note #32 (1992).
67. S. Bianco *et al.*, KLOE Note #24 and #36 (1992).
68. M. Barone and A. Parri, KLOE Note in preparation.
69. R. Brun *et al.*, CERN DD/EE/84-1 /(1991).
70. A. Antonelli *et al.*, KLOE Note #3 (1991) and #23 (1992).
71. M. Barone and A. Parri, KLOE Note #35 (1992).
72. R. Baldini and A. Michetti, KLOE Note in preparation.
73. M. Barone *et al.*, KLOE Note #26 (1992).
74. M. C. Petrucci, KLOE Note in preparation.
75. We thank Dr. Herbert Kapitza for so generously sharing his knowledge with us.

76. F. Bossi and G. Capon, KLOE Note #5 (1991); A. Farilla, G. Lanfranchi and V. Patera, KLOE Note #13 (1991); A. Calcaterra, KLOE Note #12 (1991); A. Andryakov, G. Capon and V. Patera, KLOE Note in preparation.
77. C. Bloise, KLOE Note in preparation.
78. C. Gatto et al., KLOE Note in preparation.
79. G. Capon, KLOE Note in preparation.
80. Non gaussian tail were not considered in ref. 1.
81. A. Andryakov, G. Capon, V. Patera, KLOE Note in preparation.
82. A. Calcaterra, KLOE Note in preparation.
83. N. Brown and F. E. Close, in the *DAΦNE Physics Handbook.*, ed. L. Maiani *et al.*, (INFN-LNF, 1992) 447-466, and references therein.
84. For details and references see P. J. Franzini, W. Kim, and J. Lee-Franzini, Phys. Lett. **B287**, 259 (1992) and in the *DAΦNE Physics Handbook.*, ed. L. Maiani *et al.*, (INFN-LNF, 1992) 513-544.